

Mode Tomography using Signals from the Long Range Ocean Acoustic Propagation  
EXperiment (LOAPEX)

A dissertation submitted in partial fulfillment of the requirements for the degree of  
Doctor of Philosophy at George Mason University

By

Tarun K. Chandrayadula  
Master of Science  
George Mason University, 2003  
Bachelor of Science  
University of Madras, 2001

Director: Dr. Kathleen E. Wage, Associate Professor  
Department of Electrical and Computer Engineering

Fall Semester 2009  
George Mason University  
Fairfax, VA

Copyright © 2009 by Tarun K. Chandrayadula  
All Rights Reserved

## Dedication

*To Ma, Daddy and Appu*

## Acknowledgments

First, I would like to thank my parents and my brother Appu for their love. My education has taken a long time and they have been supportive of me during its whole course.

I thank my thesis advisor Dr. Kathleen E. Wage for her guidance and support during this thesis. She has been very patient in reading the many versions of this thesis. The training that I have received from her will make me a better scientist in the future. One could not ask for better colleagues than Aravinda, Khalid, Richard and Xu. I appreciate Richard's excellent system administration help and commend his phenomenal drinking abilities. I look forward to many years of friendship and professional collaboration with all my colleagues. Rex K. Andrew of APL-UW answered my many emails about the LOAPEX data processing with utmost patience. A lot of results in this thesis would have been impossible without his help.

My long time friends, Karthik, Dinesh and Sundar provided me with company and were encouraging and supportive during my Ph.D.. Their friendship will always be invaluable to me. During my studies, I have been friends with Shyam (Bollina), Harsha, Bo Zhao (Steve), Anish, Avinash, Saravanan, Shyam (Pandula), Jaime, Linda, Christi, Swathi, Abi and Smitha. All these people are scattered across USA, India and other parts of the world. I want them to know that they all made my life more fun and interesting. I will cherish their friendship forever.

This research was made possible by the experimental work carried out by the NPAL group. I gratefully acknowledge the support from the Office of Naval Research Grant N00014-06-1-0223.

# Table of Contents

	Page
Dedication . . . . .	iii
List of Tables . . . . .	vii
List of Figures . . . . .	viii
Abstract . . . . .	xvii
1 Introduction . . . . .	1
1.1 Underwater Sound Propagation: SOFAR channel . . . . .	2
1.2 Recent experiments: LOAPEX . . . . .	2
1.3 Objectives of this thesis . . . . .	6
2 Mode propagation in the underwater sound channel . . . . .	11
2.1 Underwater acoustic propagation: Modes . . . . .	11
2.1.1 Depth dependent equations for underwater acoustic modes . . . . .	11
2.1.2 A deep water broadband simulation example . . . . .	14
2.2 Mode propagation through range-dependent environments . . . . .	18
2.2.1 The Garrett Munk model . . . . .	19
2.2.2 A simulation example for mode propagation through internal waves . . . . .	21
2.3 Mode tomography and the problems of internal waves . . . . .	21
2.3.1 Challenges to mode tomography due to internal waves . . . . .	25
2.4 Conclusions . . . . .	26
3 A statistical model for the modes at short range . . . . .	27
3.1 Background on mode coupling . . . . .	27
3.2 Statistics for modes affected by internal waves . . . . .	30
3.2.1 Setting up the PE and the coupled mode simulations . . . . .	30
3.2.2 Narrowband amplitude and phase statistics of the mode signals . . . . .	33
3.2.3 Broadband statistics for modes affected by internal waves . . . . .	40
3.3 Summary . . . . .	51
4 LOAPEX mode signals . . . . .	52
4.1 The Long Range Ocean Acoustic Propagation Experiment (LOAPEX) . . . . .	52
4.2 Mode processing . . . . .	53

4.2.1	Timing corrections for LOAPEX . . . . .	54
4.2.2	Mode filtering . . . . .	59
4.2.3	Array motion correction . . . . .	62
4.2.4	Source motion compensation . . . . .	68
4.3	Range variability in LOAPEX . . . . .	70
4.4	LOAPEX mode signals . . . . .	72
4.4.1	Time domain plots for LOAPEX . . . . .	72
4.4.2	Spectrum plots for LOAPEX . . . . .	74
4.4.3	Time coherence for modes 1 and 10 . . . . .	83
4.5	Conclusions . . . . .	85
5	Detection methods for mode signals . . . . .	88
5.1	Optimum detection methods in the absence of internal waves : quiescent matched filter . . . . .	88
5.2	Detection methods for internal wave perturbed modes: Matched Subspace Detectors . . . . .	94
5.2.1	Linear subspace model for mode signals perturbed by internal waves	97
5.2.2	Matched subspace detectors based on the linear subspace model . .	98
5.3	Error statistics of the MSD travel time estimates . . . . .	102
5.4	Discussion and conclusions . . . . .	105
6	Mode tomography using LOAPEX . . . . .	107
6.1	Mode tomography . . . . .	107
6.2	Sound speed inverse in the LOAPEX environment . . . . .	110
6.3	Mode tomography for LOAPEX . . . . .	114
6.4	Conclusions . . . . .	128
7	Conclusions . . . . .	129
7.1	Conclusions . . . . .	129
7.2	Future directions . . . . .	131
	Bibliography . . . . .	133

## List of Tables

Table	Page
3.1 Internal wave simulation parameters . . . . .	31

## List of Figures

Figure	Page
1.1 Deep water sound speed and SOFAR propagation. The left panel shows a typical North Pacific sound speed profile and the right panel shows refracted ray paths from a 800 m source to a receiver located at the same depth at a range of 45 km. . . . .	3
1.2 Location of LOAPEX. The propagation paths for the ATOC 1996 and NPAL 1998 experiments are also indicated. . . . .	4
1.3 LOAPEX reception at T50 (Yearday 259, hour 6). The top subplot shows the pressure time series across depth and the bottom subplot shows the mode time series for modes 1, 5 and 10. Modes 1, 5 and 10 (bottom subplot) are concentrated towards the finale of the pressure field. Mode 10 contains a null and has a lower amplitude than modes 1 and 5. . . . .	7
1.4 LOAPEX reception at T250 (Yearday 260, hour 21). Compared to T50, the pressure field and the modes 1, 5 and 10 have a wider time spread. Modes 1 and 5 are single peaked arrivals. Mode 10 contains multiple peaks. . . . .	8
1.5 LOAPEX reception at T500 (Yearday 262, hour 22). The pressure field has a greater time spread and resembles an “accordion” [1]. Modes 1, 5 and 10 contain multiple peaks. . . . .	9
1.6 LOAPEX T1000 reception (Yearday 265, hour 14). The later arrivals near the axis are a relatively higher SNR than the earlier arrivals. The axial arrivals however contain deep fades. Compared to shorter ranges, modes 1, 5 and 10 show more multipath. The multipath is mainly due to internal wave scattering, which increases with propagation distance. . . . .	10
2.1 Sound speed profile and modeshapes for the LOAPEX path. The left subplot shows the average sound speed profile for the LOAPEX path derived from the World Ocean Atlas [2,3] database. The right subplot shows the modeshapes for modes 1 to 10 at 75 Hz calculated from the sound speed profile. . . . .	12

2.2	The group velocity for the modes shown in figure 2.1. Note that the group velocity varies as a function of mode number and frequency. . . . .	14
2.3	The arrival times of modes 1 to 10 for frequencies 60 Hz-90 Hz at 45 km and 244.7 km. The two ranges correspond to LOAPEX T50 and T250 distances. Note that the modes spread out in time as they propagate in range. . . . .	15
2.4	Simulated reception at 3200 km. The bottom subplot shows the mode time series for modes 1, 5, and 10. The pressure field and the modes 1, 5 and 10 are dispersed in time. . . . .	17
2.5	Simulated LOAPEX reception at 3200 km. The top subplot shows the pressure time series across depth. The bottom subplot shows the mode time series for modes 1, 5 and 10. The finale of the pressure field (top subplot) shows scattering. Modes 1, 5 and 10 contain significant multipath. . . . .	22
3.1	The amplitude of the unscattered component for modes 1 and 10 for up to 400 km. Modes 1 and 10 were initialized with an initial amplitude of 1 at the source. The unscattered component decays across range. Mode 1 decays slower than mode 10. . . . .	34
3.2	The left plot shows the histogram of the wavenumbers of modes 1, 5 and 10 at 75 Hz. The histograms were generated from wavenumbers calculated for a 1000 km range. The wavenumbers are Gaussian distributed. The right plot shows the correlation of the wavenumber at 75 Hz with wavenumbers at frequencies 60 Hz to 90 Hz. The wavenumbers are highly correlated across frequency. . . . .	35
3.3	Cross coherence between modes 1 to 10 at 75 Hz across range. At 50 km the modes are correlated with each other. The modes however decorrelate with each other as they propagate farther in range. . . . .	38
3.4	SIR of the unscattered component of modes 1 and 10 obtained via narrow-band simulations at 75 Hz. Plot includes the effect of the source excitation amplitudes and the $\frac{1}{\sqrt{r}}$ dependence across range. The modes were excited at amplitudes proportional to the mode amplitudes at the LOAPEX source depth of 800 m. Mode 1 was strongly excited while mode 10 was not. Irrespective of the source excitation level, both the modes have an SIR of below 0 dB at 400 km. . . . .	39
3.5	The cross coherence of the wavenumbers of modes 1 to 10. The wavenumbers show significant cross-correlation. . . . .	39

3.6	Cross coherence of modes 1 to 10 at 75 Hz between the scattered and unscattered parts of the mode signals. The unscattered and scattered parts of the modes are uncorrelated with each other. . . . .	40
3.7	The time coherence of mode 1 at 50 km, 100 km, 250 km and 400 km. For mode 1, the unscattered and the scattered mode have similar coherence times at all ranges. . . . .	41
3.8	The time coherence of mode 10 at 50 km, 100 km, 250 km and 400 km. The unscattered mode is more coherent than the scattered mode. The difference in coherence times between the unscattered mode and the scattered mode increases with range. . . . .	42
3.9	The absolute value of the source excitation spectrum of modes 1 and 10. The source depth was set to 800 m (which is the LOAPEX source depth). The error bars, indicate the variance of the amplitudes. At 800 m source depth, the variance in mode 10 amplitudes are greater than mode 1. . . . .	43
3.10	The source excitation spectrum and the spectrum of the unscattered spectrum of modes 1 and 10. Mode 1 excitation spectra is symmetric with respect to the center frequency (75 Hz). Mode 10 excitation spectra contains nulls. The location of the nulls varies between the two IW realizations. The unscattered component for modes 1 and 10 is similar to the excitation spectrum.	44
3.11	Modes 1 and 10 for two different realizations (blue '-' for the mode signal and red '-' for the unscattered signal). For modes 1 and 10 at 50 km, the unscattered component has a significant influence on the total mode signal. That does not hold true at 250 km. . . . .	46
3.12	The normalized spectra for mode 1 and 10 at ranges of 50 km,100 km,250 km and 400 km. At 50 km and 100 km, modes 1 and 10 have a spectra that is close to the background spectrum. At 400 km, nulls appear in the spectrum for modes 1 and 10. Mode 10 appears to have deeper nulls than mode 1. . .	47
3.13	Mode (log normalized) spectra for modes 1 to 10 at different ranges. At 50 km and 100 km, the mean mode spectrum for each mode is similar to the background spectrum. At 250 km and 400 km, the mode spectra contain more scattering. At T400, mode 1 shows the least fading. . . . .	48

3.14	Standard Deviation (SD) of the TOA of mode 1 from PE simulations, Un-scattered component simulations and numerical calculations. For ranges less than 250 km, the TOA SD of the unscattered mode matches the the SD of the PE simulated mode signal implying that the TOA variations of the unscattered component are responsible for the TOA variations of the total mode signal. At 400 km mode 1 is more scattered than at shorter ranges and thus has a higher TOA SD than the unscattered mode 1. . . . .	50
3.15	Averaging losses for modes 1 and 10 at 50 km and 400 km. Averaging across time, causes loss of up to 1 db for mode 1 and 10 at 400 km. Averaging in time does not provide SNR gain. . . . .	50
4.1	LOAPEX geographical location. The experiment consisted of a ship suspended source that made mid-water transmission from 800 m depth to an array from 7 different ranges of 50 km to 3200 km along the same propagation path. . . . .	53
4.2	The different stages in broadband mode processing for LOAPEX . . . . .	54
4.3	LOAPEX arrivals vs predictions at T50. The left subplot shows the peak arrivals of LOAPEX at each depth. The right subplot shows the difference between the time of arrival of the peak at each depth and predicted times of arrival of the peak at each depth. The right subplot shows the difference between the peak arrival for LOAPEX and the predictions across depth. The travel time offset has a mean of 17.2 ms. . . . .	58
4.4	The T50 LOAPEX signals compensated only for receiver delays, processing delays and a source delay of 17.2 ms. . . . .	58
4.5	The MF beamformer beampattern for modes 1 to 40 for the measured profile. The beampattern is defined as $20 \log_{10}(\mathbf{W}^H \mathbf{\Psi})$ where $\mathbf{W}$ is the MF beamformer defined in equation 4.7 and $\mathbf{\Psi}$ is the matrix of modeshapes sampled at the array. The MF beamformer resolves modes 1 to 10 with minimal crosstalk. . . . .	61
4.6	The eigenvalues ( $\lambda$ ) of the correlation matrix of the navigation data. The top subplot shows that the first 3 eigenvalues are at least 25 dB higher in amplitude than the rest of the eigenvalues. The bottom subplot shows a plot of the percentage of the cumulative energy contained in the eigenvalues. The first 3 eigenvalues make up more than 99.99 % of the energy in the navigation data. . . . .	66

4.7	EOFs 1 to 3 for the navigation data from yeardays 160 to 240. The 3 EOFs roughly describe the shape of the array in the X, Y and Z directions. . . . .	66
4.8	EOF sample reconstruction for yearday 402. The black (o) curve shows the true position of the array and the red (x) curve shows the reconstructed array.	67
4.9	The Root Mean Square Error (RMSE) performance of the EOF based reconstruction for yeardays 400 to 480 as a function of depth. The 3 EOFs shown in figure 4.7 were used in the EOF estimator. The RMSE decreases as a function of depth. The mean RMSE is on the order of 1.5 m. . . . .	68
4.10	Spatial gain for different modes as a function of tilt. The tilt is measured with reference to the lowest hydrophone. The left plot shows that modes 10 and 40 are more sensitive to tilt than mode 1. A tilt of more than 10 m causes a loss of more than 3 dB for modes 10 and 40. The right plot shows the loss in gain for a tilt of 3 m, which is the EOF mooring estimation error. The modes do not suffer more than 0.3 d dB loss. . . . .	69
4.11	Source motion at T50 and T250. The source moves on the order of 10 m to 15 m. . . . .	69
4.12	Sound speed profiles measured along the LOAPEX path. The SSP (Seabird) at the VLA (cyan -+), the T50 CTD (red '-.') profile, the T250 CTD (black '-. '), the T500 CTD (blue '-. ') SSPs vary across range. Although the T50 CTD profile and the SSP at the VLA were measured only 50 km apart, the two profiles are much different from each other. . . . .	71
4.13	Modes 1 (blue) and 10 (red -. ) at T50. There were 10 transmissions on yearday 259 between hours 6 and 15. Modes 1 and 10 are dispersed over time. The arrival structure and the time of arrival for modes 1 and 10 changes across time. The arrival structure for mode 1 consists of a single peaked arrival and mode 10 for some receptions consists of a double peaked arrival. . . . .	75
4.14	Modes 1 (blue) and 10 (red -. ) at T250. There were 8 transmissions that occurred between yeardays 260 to 261 from hour 21 to hour 6. Compared to T50, the amount of inter-modal dispersion and the chromatic dispersion is greater. Mode 1 contains small arrivals that precede the main arrival. Mode 10 for some receptions contains more than two peaks. . . . .	76

4.15	Modes 1 (blue) and 10 (red -.) at T500. There were 14 transmissions that occurred between yeardays 262-263 in an intermittent manner. Both, modes 1 and 10 contain multiple peaks/arrivals. This implies that the amount of scattering is significantly higher than at T250. Also note that the amount of variability of the mode arrivals across time is higher than the previous ranges (Figures 4.13 and 4.14). . . . .	77
4.16	Travel time estimates at T50. The errorbars indicate the standard deviation. The travel time estimates are closer to the Seabird SSP measured at the array than the CTD profile measured at the source. . . . .	78
4.17	Travel time estimates at T250. The errorbars indicate the standard deviation. The travel time estimates for the three different methods all lie close to the travel times predicted by the profiles at T50 and T250. . . . .	79
4.18	Travel time estimates at T500. The errorbars indicate the standard deviation. The mean travel time estimates lie midway between the predictions made using the different profiles. The variance of the travel times is much greater than at T50 and T250. . . . .	80
4.19	Travel time standard deviation for modes 1 and 10 during LOAPEX. . . . .	80
4.20	Seabird (yearday 259) and the T50 CTD spectrum for modes 1 and 10. The background spectrum varies for the two SSPs. However, mode 10 for both the profiles is weakly excited. . . . .	81
4.21	Modes 1 and 10 spectra at T50. Mode 10 shows more variability than mode 1. For some of the receptions, mode 10 contains nulls around 80 Hz. . . . .	82
4.22	Spectrum for modes 1 and 10 during yearday 259. . . . .	82
4.23	Mode 1 and 10 spectrum at T250. Mode 10 is excited at much lower level than mode 1. . . . .	83
4.24	Modes 1 and 10 spectra at T250. Mode 1 shows more amplitude variability than at T50. Mode 10 still shows more variability for the higher frequencies, however the lower frequencies of mode 1 have started showing more variability than at T50. . . . .	84
4.25	Modes 1 and 10 spectra at T500. Both the modes show the same amount of variability. The amount of amplitude variability is almost the same across frequency. . . . .	84
4.26	Mode 1 and 10 spectrum at T500. Mode 10 is excited at much lower level than mode 1. . . . .	85
4.27	Time coherence at T50 . . . . .	86

4.28	Time coherence at T250 . . . . .	86
4.29	Time coherence at T500 . . . . .	87
5.1	Finite bandwidth source response $H(f)$ . The frequency response spans frequencies of 40 Hz to 110 Hz and has a peak at 75 Hz. . . . .	89
5.2	Sound speed profile and the modeshapes for the LOAPEX path. The left subplot shows the average sound speed profile for the LOAPEX path derived from the World Ocean Atlas [2, 3] database. The right subplot shows the modeshapes at 75 Hz of modes 1 to 10 calculated from the sound speed profile. . . . .	90
5.3	quiescent frequency response. The mode amplitudes for frequencies 40 Hz to 110 Hz weighed with the source response in Figure 5.1. Modes 6, 9 and 10 contain nulls close to 75 Hz. . . . .	91
5.4	Quiescent time series for modes 1 and 10 (black) and the time of arrival of the 75 Hz component for each mode (red). The time of arrival of the peak of mode 10 differs from the 75 Hz component. . . . .	92
5.5	The quiescent time series (black), the output of the quiescent detector (blue -.) and the the travel time of the 75 Hz component of the background profile for modes 1 and 10. The peak of the quiescent detector matches the time of arrival of the 75 Hz component. . . . .	95
5.6	Performance of the quiescent matched subspace detector at T50, no internal waves. The travel time estimation error is defined as the difference between the travel time estimate and the predicted travel times at 75 Hz. The quiescent matched filter recovers the background travel times. . . . .	95
5.7	Performance of the quiescent matched subspace detector at T250, no internal waves. The travel time estimation error is defined as the difference between the travel time estimate and the predicted travel times at 75 Hz. The quiescent matched filter recovers the background travel times. . . . .	96
5.8	The source excitation spectrum for 2 different internal wave realizations (black ‘-’ and red ‘.’) and the quiescent spectrum (blue ‘.’). Internal waves cause variations in the source excitations spectrum. Mode 10 shows significant variation in mode spectrum for internal wave variations. . . . .	97
5.9	The percentage of energy of the first 5 EOFs of modes 1 to 10. All the modes are described by not more than 2 EOFs. In modes 6 and 10, the first EOF accounts for less than 90 percent of the total energy implying that modes 6 and 10 are more complicated. . . . .	99

5.10	EOFs 1 and 2 for modes 1 and 10 at T50. . . . .	99
5.11	Comparison of the spectrum of the background profile (blue -), the spectrum of EOF 1 (red -) and the spectrum of EOF 2 (black -). The spectrum of EOF 1 is similar to the spectrum of the first EOF. . . . .	100
5.12	MSD sample output at 50 km for modes 1 and 10. MSD sample output at 50 km for modes 1 and 10. For modes 1 and 10, the 1 D MSD and the quiescent detector are matched to the signal arrival. The MSDs and the quiescent detectors compress the mode signal into a single arrival. . . . .	101
5.13	MSD sample output at 50 km for modes 1 and 10 for an internal wave realization. Mode 1 is similar to the arrival in Figure 5.12. Mode 10 on the other hand completely differs from the corresponding arrival in Figure 5.12. The 2 D MSD for mode 10 gives a more stable arrival with respect to the mode arrival in Figure 5.12. . . . .	102
5.14	Travel time estimation at T50. For modes 3, 6,7,9 and 10 the 2 D MSD has a lower error and a more stable arrival. . . . .	103
5.15	Travel time estimation at T250. Peak picking and the quiescent detector have a lower mean error than the MSDs . . . . .	103
5.16	Travel time estimation at T400. Modes 1 and 2 have a lower travel time error and are more stable. . . . .	104
6.1	The modeshapes (red) and the sensitivity matrix (blue) for the mean Seabird profile. The depth resolution of the different columns is roughly proportional to the span of each mode. The higher modes span greater depths and offer more resolution across depth. . . . .	113
6.2	Sound speed perturbations (m/s) (with respect to the time averaged mean SSP) at the VLA. The perturbations vary between $\pm 3$ m/s. . . . .	115
6.3	Statistics of the high pass filtered sound speed perturbations (with respect to the time averaged mean SSP). The standard deviation (left subplot) is around .1 m/s. The maximum and minimum of the sound speed perturbations (right subplot) vary with depth. Around the axis between 600 m to 1000 m, the maximum perturbations are on the order of $\pm .25$ m/s, whereas at shallower depths around 350 m, the sound speed perturbations can go up to .5 m/s. . . . .	116

6.4	One day averages of the sound speed perturbations in m/s (with respect to the time averaged mean SSP) at the VLA. The one day averages of the sound speed perturbations are larger than the magnitudes of the high pass filtered sound speed perturbations in Figure 6.3. The one day averages of the sound speed perturbations vary between -1 m/s and +2 m/s. . . . .	117
6.5	EOFs 1 to 3 estimated from the sound speed perturbations at the VLA. The plotted EOFs make up for more than 99 % of the energy in the sound speed perturbations. . . . .	118
6.6	Travel time estimates at T50. The errorbars indicate the standard deviation of the estimates. The travel time estimates are closer to the Seabird SSP measured at the array than the CTD profile measured at the source. The 2 D MSD yields a less travel time variance. . . . .	120
6.7	Sound speed perturbations inverse at T50. The inverted SSP is closer to the Seabird SSP. The errorbars of the sound speed inverses show that the inverse obtained by using the 2 D MSD has a lower variance. . . . .	121
6.8	Travel time estimates at T250. The errorbars indicate the standard deviation of the estimates. The travel time estimates for the three different methods all lie close to the travel times predicted by the profiles at T50 and T250. Similar to T50, the MSD travel times have a less variance. . . . .	123
6.9	Tomographic inverse at T250. The inverse sound speed profile is close to the CTD profile at T250. The errorbars of the sound speed inverses show that the inverse obtained by using the 2 D MSD has a lower variance. . . . .	124
6.10	Travel time estimates at T500 (via peak picking). The errorbars indicate the standard deviation of the estimates. The LOAPEX mode travel times are closer to the travel times predicted by the mean SSP than any of the other spot measurements. . . . .	125
6.11	Sound speed inversion results at T500 using modes 1 to 3 (left plot) and using modes 1 to 10 (right plot). The SSP inversion results have a much higher variance than at T50 and T250. Using only modes 1 to 3, decreases the variance of the sound speed inverse, however causing poor inversion results for depth above 500 m. . . . .	126
6.12	Mean sound speed inverse at T500 using modes 1 to 10. The mean of the sound speed inverse is close to the mean SSP obtained by averaging the SSPs measured across the T500 path. . . . .	127

## Abstract

MODE TOMOGRAPHY USING SIGNALS FROM THE LONG RANGE OCEAN ACOUSTIC PROPAGATION EXPERIMENT (LOAPEX)

Tarun K. Chandrayadula, PhD

George Mason University, 2009

Dissertation Director: Dr. Kathleen E. Wage

Ocean acoustic tomography uses acoustic signals to infer the environmental properties of the ocean. The procedure for tomography consists of low frequency acoustic transmissions at mid-water depths to receivers located at hundreds of kilometer ranges. The arrival times of the signal at the receiver are then inverted for the sound speed of the background environment. Using this principle, experiments such as the 2004 Long Range Ocean Acoustic Propagation EXperiment have used acoustic signals recorded across Vertical Line Arrays (VLAs) to infer the Sound Speed Profile (SSP) across depth. The acoustic signals across the VLAs can be represented in terms of orthonormal basis functions called modes. The lower modes of the basis set concentrated around mid-water propagate longer distances and can be inverted for mesoscale effects such as currents and eddies. In spite of these advantages, mode tomography has received less attention. One of the important reasons for this is that internal waves in the ocean cause significant amplitude and travel time fluctuations in the modes. The amplitude and travel time fluctuations cause errors in travel time estimates. The absence of a statistical model and the lack of signal processing techniques for internal wave effects have precluded the modes from being used in tomographic inversions.

This thesis estimates a statistical model for modes affected by internal waves and then uses the estimated model to design appropriate signal processing methods to obtain tomographic observables for the low modes. In order to estimate a statistical model, this thesis uses both the LOAPEX signals and also numerical simulations. The statistical model describes the amplitude and phase coherence across different frequencies for modes at different ranges. The model suggests that Matched Subspace Detectors (MSDs) based on the amplitude statistics of the modes are the optimum detectors to make travel time estimates for modes up to 250 km. The mean of the travel time estimates is close to the mode travel times for the background SSP. The travel time estimates produced by the MSDs have a smaller variance than other signal processing methods that do not take into account the statistics of the mode signals. The MSDs are applied to the LOAPEX signals to make travel time estimates for modes received at ranges of 50 km and 250 km. The estimated sound speed inverse for the mid-water depths is consistent with spot measurements made during LOAPEX. Work sponsored by Office of Naval Research Grant N00014-06-1-0223.

## Chapter 1: Introduction

Ocean Acoustic Tomography (OAT) is the science of probing the ocean using sound signals [1]. OAT makes use of the transparency of the ocean to sound to sample large distances. The travel time of the received signal is inverted for the sound speed of the intervening water column. Tomography requires accurate travel time measurements. The ocean environment fluctuates in time across micro and macro scales [1], [4]. The variations in the ocean cause travel time estimation errors. This thesis focuses on signal processing techniques to suppress the micro scale fluctuations caused by internal waves in the ocean. The main challenge in designing the signal processing techniques is to accurately model the effects of internal waves. Hence, the initial part of this thesis is devoted to developing an empirical statistical model for the internal wave effects. This thesis approaches the statistical modeling by analyzing simulations and data recorded during the Long Range Ocean Acoustic Propagation Experiment (LOAPEX). The second part of the thesis applies the statistical model to develop signal processing methods and observables for tomography. The main goal in developing the model and obtaining the observables is to invert for the sound speeds along the LOAPEX path.

The rest of this chapter introduces the specific research questions addressed by this thesis. Section 1.1 briefly describes the underwater sound channel and how it acts as a waveguide to carry sound. Following that, Section 1.2 shows receptions that were recorded during LOAPEX. The sample receptions illustrate underwater sound propagation and, more importantly, show the effects of internal waves on acoustic signals. The variability and complexity in the receptions motivate the need for statistical modeling and signal processing methods. Finally, Section 1.3 outlines the specific objectives of this thesis.

## 1.1 Underwater Sound Propagation: SOFAR channel

Figure 1.1 shows the depth dependent Sound Speed Profile (SSP) for a typical profile in the North Pacific. The SSP is a function of depth. As the figure illustrates, there is a minimum in the SSP at 800 m and it increases towards the surface and bottom. The sound speed minimum is called the sound channel axis. The anisotropic nature of the SSP gives the underwater sound channel its characteristic features. For the sake of simplicity, consider an underwater isotropic source that radiates equal energy in all directions. The energy around the sound speed minimum is refracted towards the axis. The curved nature of the SSP traps the axial sound and carries it to megameter ranges. On the other hand acoustic energy propagating at steep angles with respect to the horizontal is attenuated. The underwater sound channel thus acts as an acoustic waveguide. This is called the Sound Fixing and Ranging or SOFAR property of the underwater sound channel. Long range tomography relies on the SOFAR property to transmit signals across long distances.

A typical tomographic experiment consists of a low frequency underwater source and a receiver separated in distance. The receiver consists of either one or multiple hydrophones. In the case of multiple hydrophones, they are usually arranged as a linear array. The signal at the receiver is matched filtered to increase the SNR. When the receiver is a linear array, spatial filtering techniques are also used to increase the signal level. The travel time of the received signal is estimated and the the travel time estimate is inverted for the sound speed of the intervening water column.

## 1.2 Recent experiments: LOAPEX

Multiple experiments have taken place in the last 15 years. Figure 1.2 shows the location of the major long range propagation experiments conducted in the past 15 years. The Acoustic Thermometry of Ocean Climate (ATOC) 1996 and the North Pacific Acoustic Laboratory (NPAL) 1998 transmitted acoustic signals to receiver VLAs at ranges on the order of 3000 km. The Long Range Ocean Acoustic Propagation Experiment (LOAPEX)

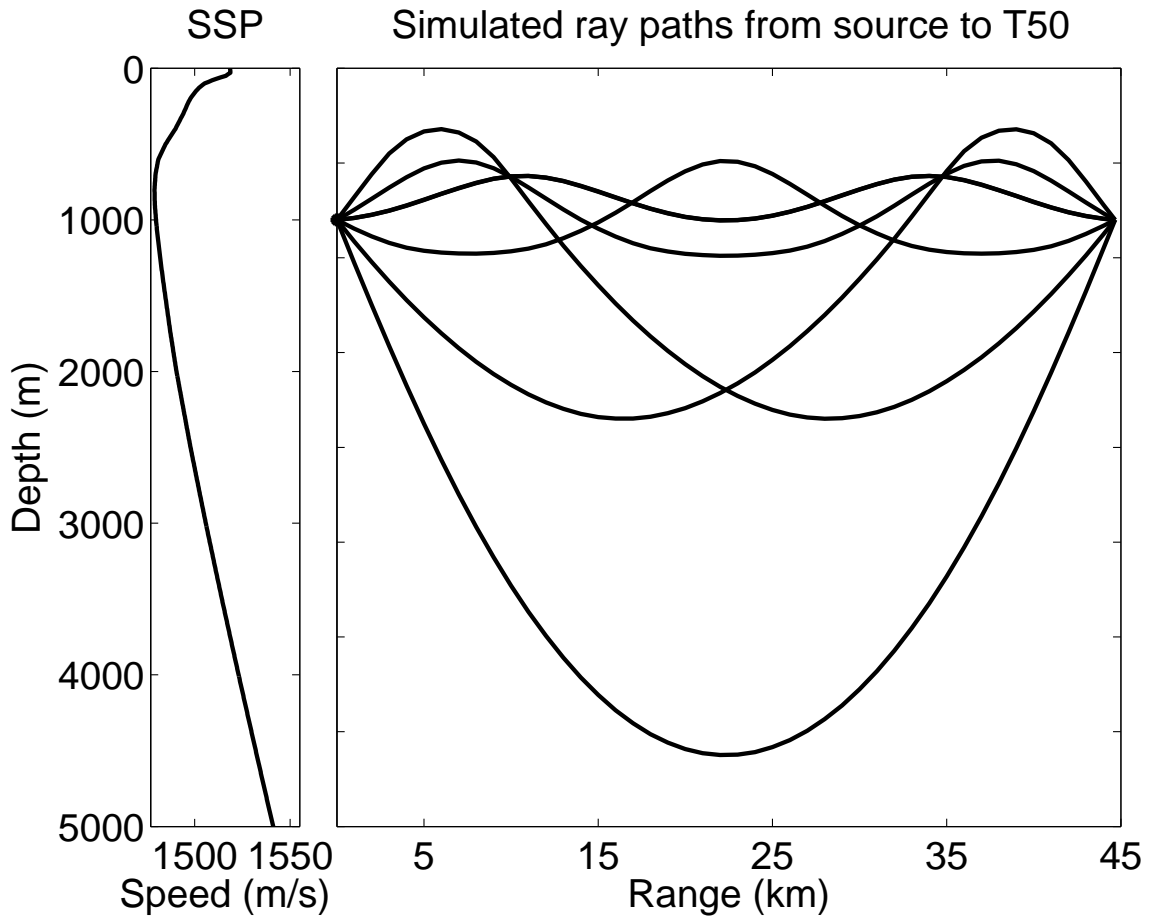


Figure 1.1: Deep water sound speed and SOFAR propagation. The left panel shows a typical North Pacific sound speed profile and the right panel shows refracted ray paths from a 800 m source to a receiver located at the same depth at a range of 45 km.

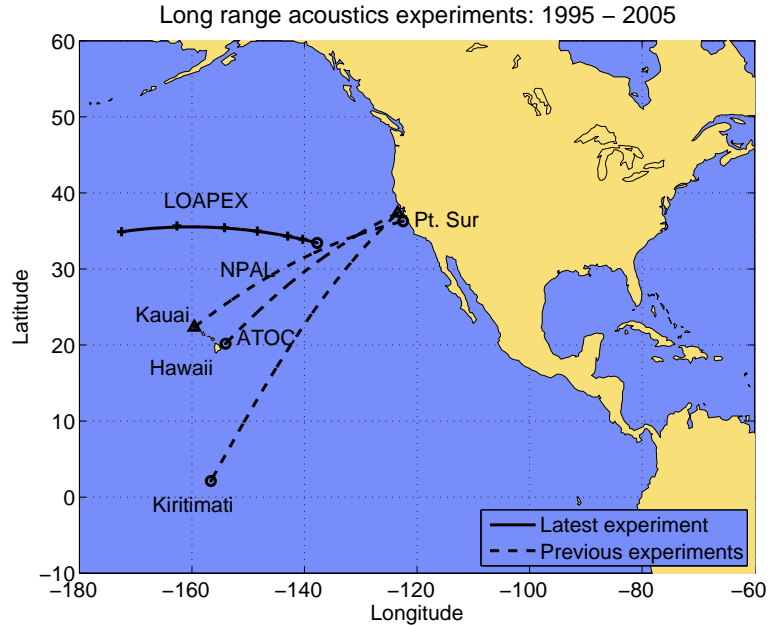


Figure 1.2: Location of LOAPEX. The propagation paths for the ATOC 1996 and NPAL 1998 experiments are also indicated.

was later conducted in 2004. Unlike the ATOC and NPAL experiments, LOAPEX had transmissions at different ranges across the same propagation path. During LOAPEX, a 75 Hz source with a bandwidth of 30 Hz made acoustic transmissions at distances of 50 km, 250 km, 500 km, 1000 km, 1600 km, 2300 km and 3200 km to a Vertical Line Array (VLA) spanning depths of 350 m to 1750 m. Analysis of the LOAPEX signals forms a significant portion of this thesis. The next two paragraphs describe the LOAPEX signals at different ranges.

Figures 1.3 to 1.6 show sample LOAPEX receptions at ranges of 50 km, 250 km, 500 km and 1000 km. The top subplots of Figures 1.3 to 1.6 show the entire pressure field across depth, whereas the bottom subplots shows the result of spatial filtering of the pressure field. This section discusses the pressure field and then describes the output of the spatial filters. Plots of the measured pressure field at the different LOAPEX ranges illustrate the main features of acoustic propagation. The early parts of the pressure field at all the ranges consist of arrivals spanning the whole VLA (1400 m aperture). The later parts of

the pressure field are concentrated near the axis. Munk likens the structure of the pressure field to that of an accordion [1]. The early arrivals are typically analyzed using ray theory and the later arrivals are analyzed in terms of depth dependent orthogonal functions called modes. The rays and modes are a manifestation of the depth dependent SSP in Figure 1.1. The rays sample the shallow and deep portions of the waveguide that have higher sound speeds, thus they are associated with the early arrivals in the accordion. The modes, on the other hand, sample the water around the sound speed axis, thus they are associated with the late arrivals.

The late modes are of importance to the tomographers for two reasons. First, these modes are usually at a high SNR, thus they may be detectable at longer distances than the rays. Second, the modes populate the axis, which is affected by mesoscale activity [4], [1]. Most of the heat fluxes in the ocean take place through mesoscale activity [1], thus tracking mesoscale changes is of great interest to oceanographers. Spatial filters can be used to isolate the low modes from the pressure field. Later chapters describe the spatial filtering in more detail. For now, it is sufficient to consider the outputs of the mode filters for the LOAPEX receptions. The bottom subplots of Figures 1.3 to 1.6 show the output of the mode filter for modes 1, 5 and 10 for ranges of 50 km to 1000 km. The nomenclature for LOAPEX station consists of labeling each station with a 'T' followed by the nominal range for the particular station, e.g., T50, T250 etc. The different mode signals from LOAPEX stations, T50 to T1000 show two kinds of dispersion. First, the different modes sample the different depths of the SSP in Figure 1.1, thus arrive at different times. This is known as intermodal dispersion. Second, modes propagating in the SOFAR channel undergo chromatic dispersion, meaning that the different frequencies in the mode arrive at different times. While the two types of waveguide dispersion explain the overall structure of the modes, the modes also show increasing amounts of multipath with range. The reasons for multipath are as follows. The LOAPEX environment contained internal waves. Due to internal waves, the background environment is seldom stationary with respect to range. The internal waves in the ocean cause small scale fluctuations to the background SSP. The internal wave perturbations vary

across range and time. The sound speed perturbations induce scattering of the acoustic signals. Internal wave induced scattering increases with range. The cumulative effects of internal wave induced multipath are obvious while considering the mode signals at ranges much farther than 50 km. The reception at T250 in Figure 1.4 compared to the reception at T50 in Figure 1.3, shows an extra peak for mode 10. Figure 1.5 shows that at T500, the modes 1, 5 and 10 all contain more than one peak. Moving on to T1000, Figure 1.6 shows that the number of peaks for each mode is significantly higher than at all the preceding ranges. The nature of the multi-peaks modes at all the ranges lack an obvious analytical representation. The complicated nature of internal wave effects makes it challenging to decide the right observables for tomography.

### 1.3 Objectives of this thesis

The last section indicated that modes are attractive for tomography but may be difficult to use due to their sensitivity to internal wave induced scattering. A statistical model for the internal wave effects as a function of range and time should help in mode tomography. This thesis has three objectives. The first objective is to develop a statistical model for internal wave effects on mode signals in the LOAPEX environment. Dozier and Tappert's [5, 6] work on internal wave effects on modes across range is the most widely cited work on mode coupling. Although Dozier and Tappert's work has been influential, it has not been completely experimentally verified. LOAPEX has provided a unique data set that can be used to study the evolution of mode statistics at different ranges. This thesis uses simulations and the LOAPEX signals to build a model for mode signals as a function of range. The second objective is to use the statistical model to suggest signal processing techniques and suggest observables for mode tomography. The third objective is to use the signal processing techniques and the observables for mode tomography.

To address these objectives, this thesis is organized into the following chapters. The next chapter gives a more detailed explanation of the characteristics of the underwater channel and how the received pressure field in the ocean can be expressed in terms of rays and modes.

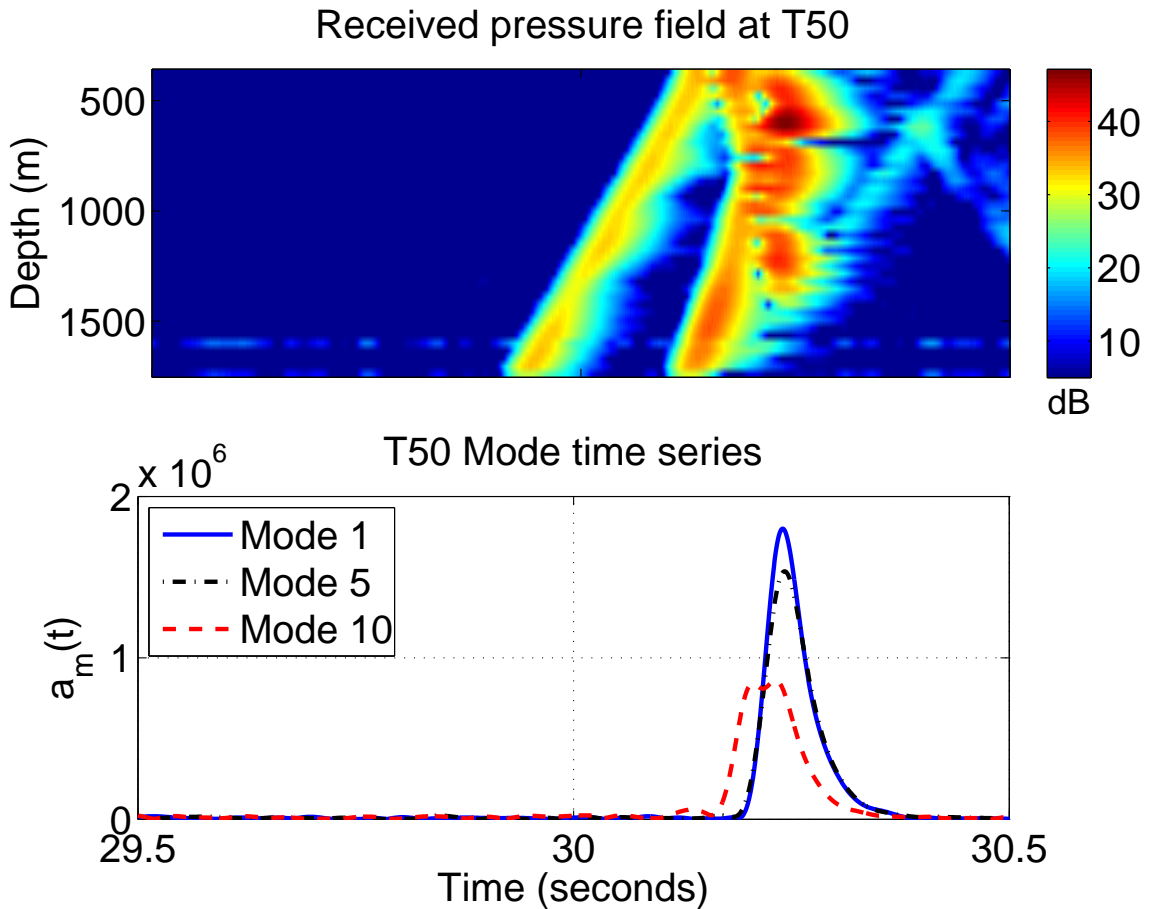


Figure 1.3: LOAPEX reception at T50 (Yearday 259, hour 6). The top subplot shows the pressure time series across depth and the bottom subplot shows the mode time series for modes 1, 5 and 10. Modes 1, 5 and 10 (bottom subplot) are concentrated towards the finale of the pressure field. Mode 10 contains a null and has a lower amplitude than modes 1 and 5.

Chapter 3 uses the coupled mode theory [5,6] to describe mode scattering in more detail and then uses simulations to build a statistical model for mode signals at different ranges. Chapter 4 analyzes the mode signals received during LOAPEX and compares the measured statistics with the statistics derived from the simulations. Chapter 5 uses the estimated statistical model to define Matched Subspace Detectors (MSDs) that make optimal travel time estimates for the modes affected by internal waves. Chapter 6 uses the model and the MSDs to perform mode tomography for the SSPs along the LOAPEX path. Chapter 7 presents conclusions and future directions.

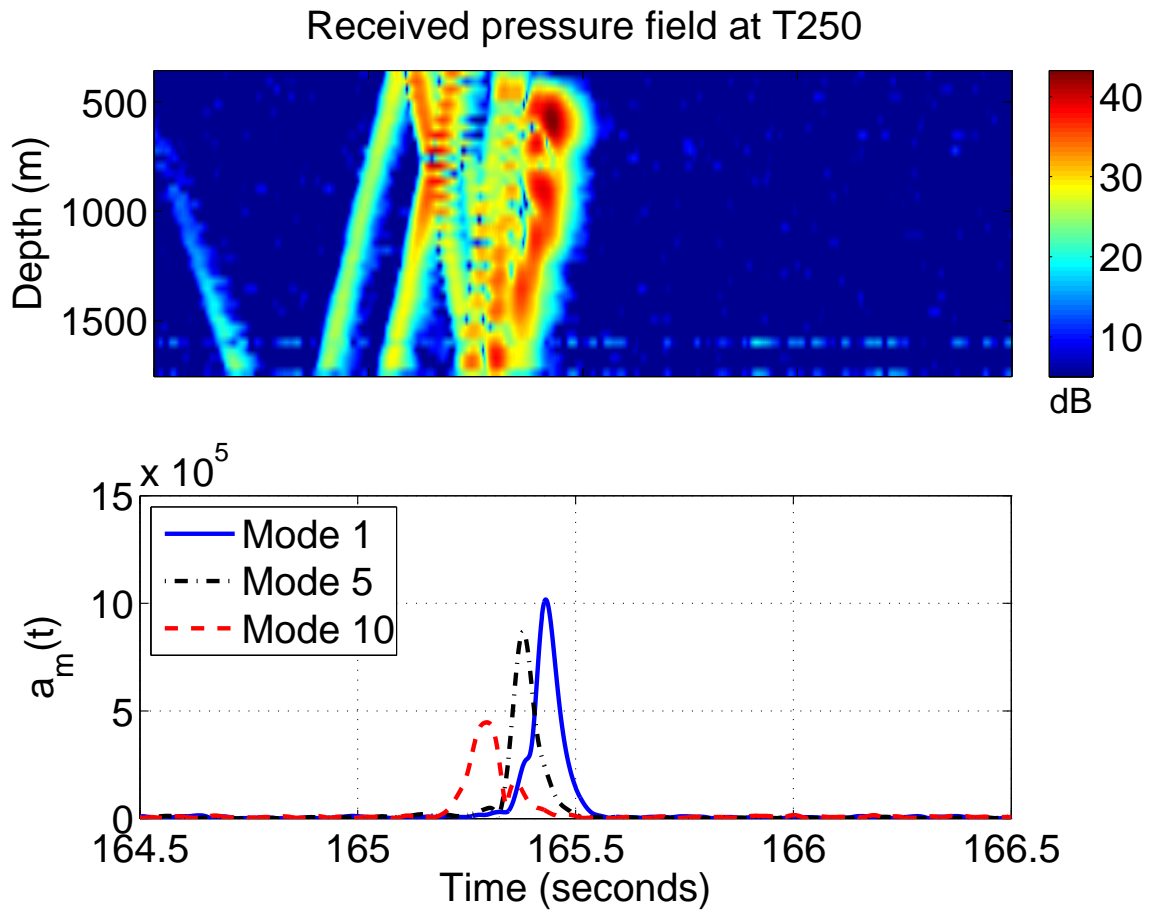


Figure 1.4: LOAPEX reception at T250 (Yearday 260, hour 21). Compared to T50, the pressure field and the modes 1, 5 and 10 have a wider time spread. Modes 1 and 5 are single peaked arrivals. Mode 10 contains multiple peaks.

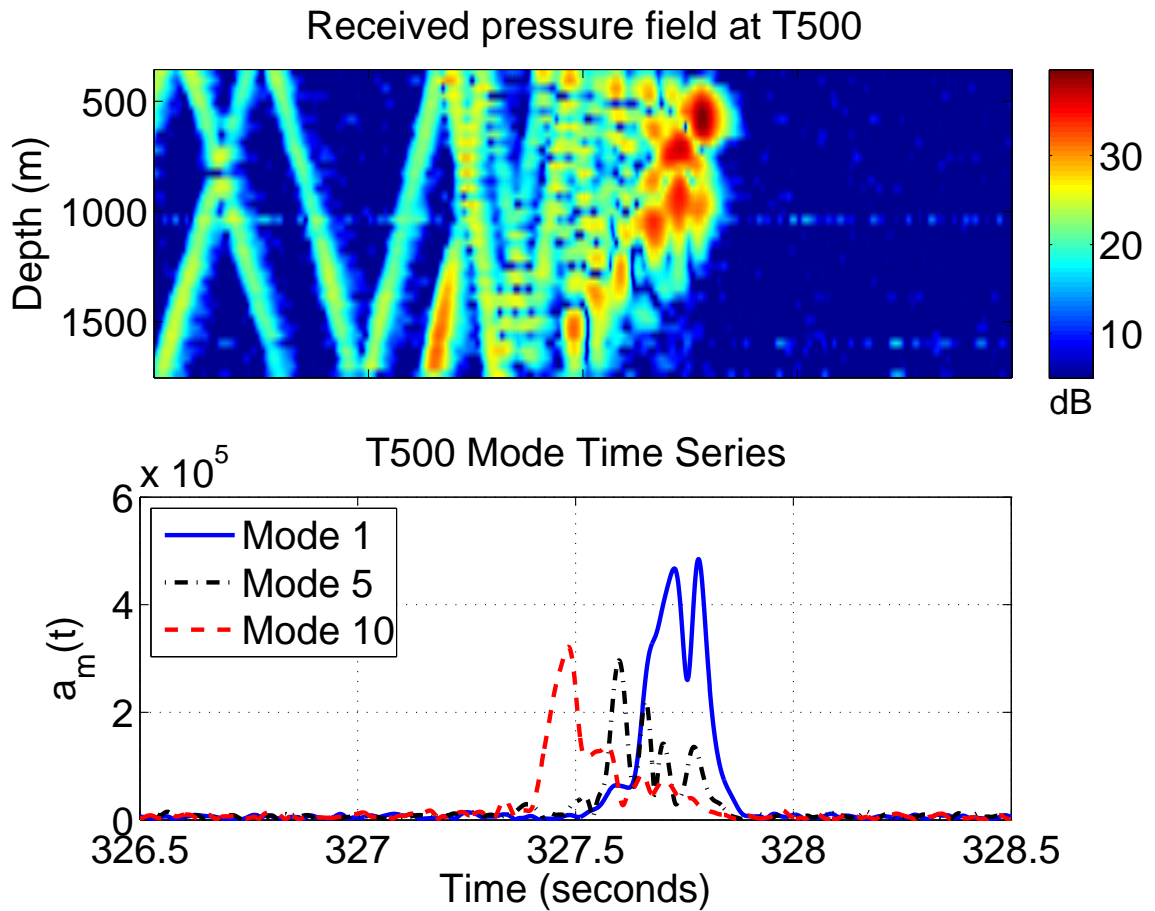


Figure 1.5: LOAPEX reception at T500 (Yearday 262, hour 22). The pressure field has a greater time spread and resembles an “accordion” [1]. Modes 1, 5 and 10 contain multiple peaks.

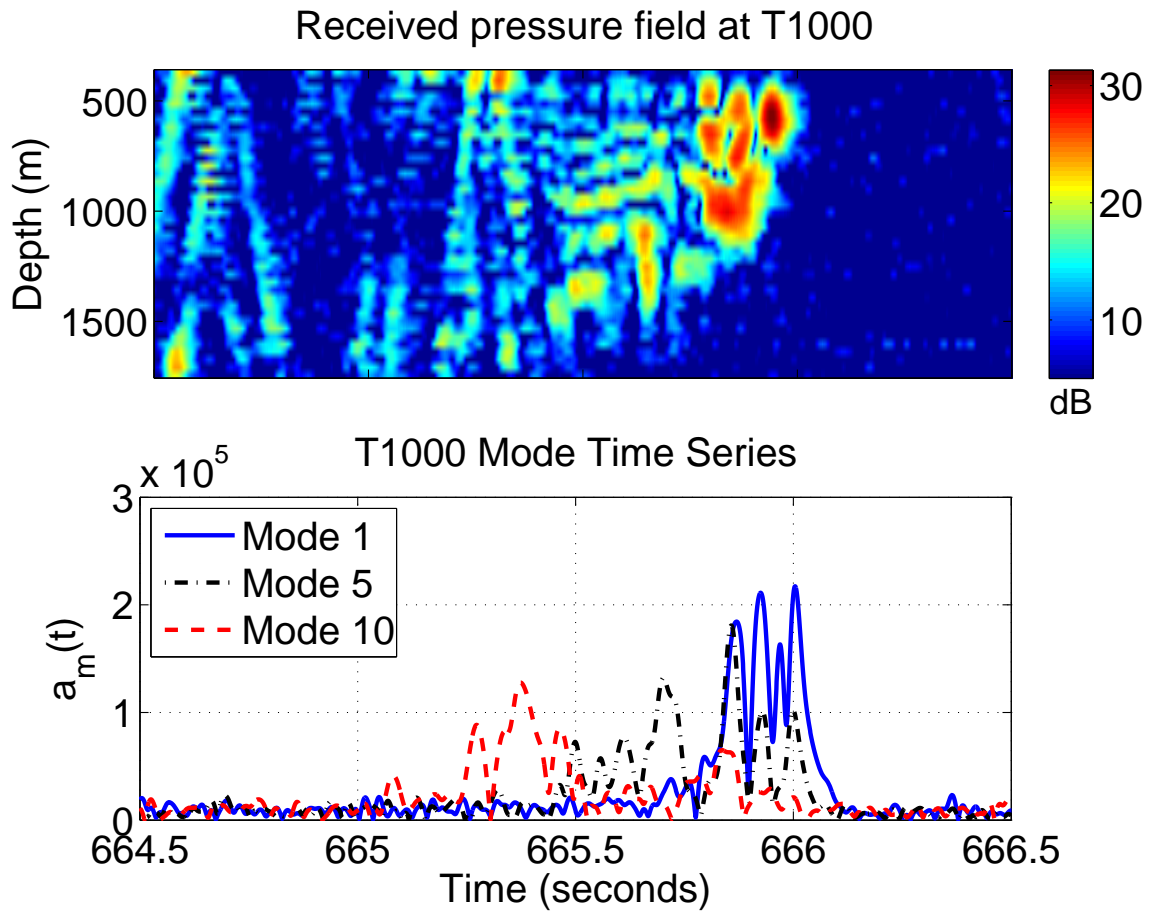


Figure 1.6: LOAPEX T1000 reception (Yearday 265, hour 14). The later arrivals near the axis are a relatively higher SNR than the earlier arrivals. The axial arrivals however contain deep fades. Compared to shorter ranges, modes 1, 5 and 10 show more multipath. The multipath is mainly due to internal wave scattering, which increases with propagation distance.

## Chapter 2: Mode propagation in the underwater sound channel

Underwater acoustic propagation has been extensively studied and excellent textbooks have been written on it ([7], [8]). The theory behind underwater propagation can be explained in terms of rays or modes. This chapter focuses on mode propagation through range-independent and range-dependent environments. The material in this chapter is organized in three parts. The first part describes underwater sound propagation in terms of modes. The second part uses simulations to illustrate mode propagation through range-dependent environments. The third part reviews literature on mode tomography and describes how internal waves pose challenges for tomographic applications.

### 2.1 Underwater acoustic propagation: Modes

Chapter 1 briefly discussed the nature of SOFAR propagation. This section gives a more detailed explanation of the characteristics of underwater sound propagation. The material on underwater sound propagation is explained using both theory and simulations. Section 2.1.1 expresses the pressure field across depth in terms of orthogonal functions called modes. Section 2.1.2 uses simulations to show how the structure of the pressure field is given by the modes of the waveguide.

#### 2.1.1 Depth dependent equations for underwater acoustic modes

The SSP or the depth dependent sound speed structure is the most important factor influencing underwater sound propagation. Figure 2.1 shows a typical deep water SSP for temperate latitudes. Using the Helmholtz equation for the SSP in Figure 2.1 it can be shown that the narrowband pressure field across depth and range can be written as

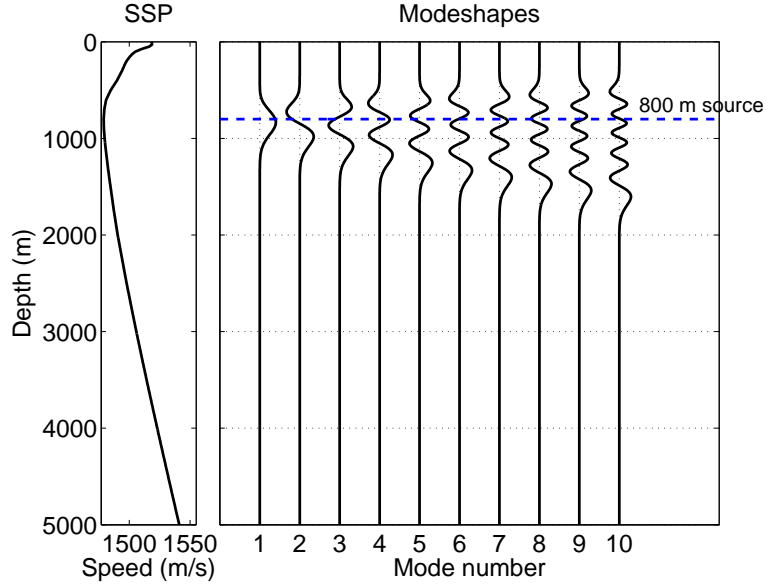


Figure 2.1: Sound speed profile and modeshapes for the LOAPEX path. The left subplot shows the average sound speed profile for the LOAPEX path derived from the World Ocean Atlas [2,3] database. The right subplot shows the modeshapes for modes 1 to 10 at 75 Hz calculated from the sound speed profile.

$$p(r, z) = \sum_{m=1}^{\infty} a_m(r) \psi_m(z) \quad (2.1)$$

Equation 2.1 gives the pressure field  $p$  at range  $r$  and depth  $z$  as a linear combination of mutually orthogonal functions  $\psi_m(z)$  each weighed by range-dependent functions  $a_m(r)$ . The depth dependent functions are called modes, likening them to modes of a vibrating string. The modes are the solution to the depth dependent wave equation,

$$\frac{d^2 \psi_m(z)}{dz^2} + \left( \frac{\omega^2}{c^2(z)} - k_m^2 \right) \psi_m(z) = 0 \quad (2.2)$$

with the boundary conditions,

$$\psi_m(0) = 0 \text{ and } \left. \frac{d}{dz} \psi_m(z) \right|_{z=D} = 0 \quad (2.3)$$

where  $D$  is the depth of the bottom. Equation 2.2 with the boundary conditions in Equation 2.3 is an eigenvalue problem with eigenvalues  $k_m$  and the eigenfunctions  $\psi_m(z)$ . The eigenfunctions are orthonormal to each other, i.e.,

$$\int_0^D \psi_m(z)\psi_n(z)dz = \delta(m - n). \quad (2.4)$$

Note that for an SSP that is constant in depth, the solution to Equation 2.2 is a complex exponential of the form  $e^{jk_m z}$ . In typical deep water environments the SSP  $c(z)$  is not constant, rather it is curved with a minimum around 700 m to 1000 m. In these environments, the modes  $\Psi_m(z)$  are similar to sine waves near the axis but they exponentially decay away from the axis. Figure 2.1 shows the SSP and the corresponding modeshapes computed using Prufer normal code. Each mode has a unique depth dependent structure and has exactly  $m - 1$  zeroes (where  $m$  is the mode number) between the surface and the bottom.

In a range-independent environment the SSP and the boundary conditions remain constant across range, the range functions for a range-independent environment are given by,

$$a_m(r) = \psi_m(z_s) \frac{ie^{-i\pi/4}}{\sqrt{8\pi}} \frac{e^{ik_m r}}{\sqrt{k_m r}}. \quad (2.5)$$

The above equation is a well-known solution for the amplitudes of underwater modes [7]. Equation 2.5 shows that for a range-independent environment, the mode amplitudes at a range  $r$  are a function of the excitation amplitude of the mode  $\psi_m(z_s)$  at the source depth  $z_s$  and the  $\frac{1}{\sqrt{r}}$  range dependence due to cylindrical spreading. While the modeshapes  $\psi_m(z)$  specify the mode structure as a function of depth  $z$ ,  $a_m(r)$  describes the mode as a function of range  $r$ .

The depth dependent equation in 2.2 is a narrowband equation i.e, it describes the pressure field and the modes at a single frequency  $\omega$ . The modeshapes  $\psi_m(z)$  and the

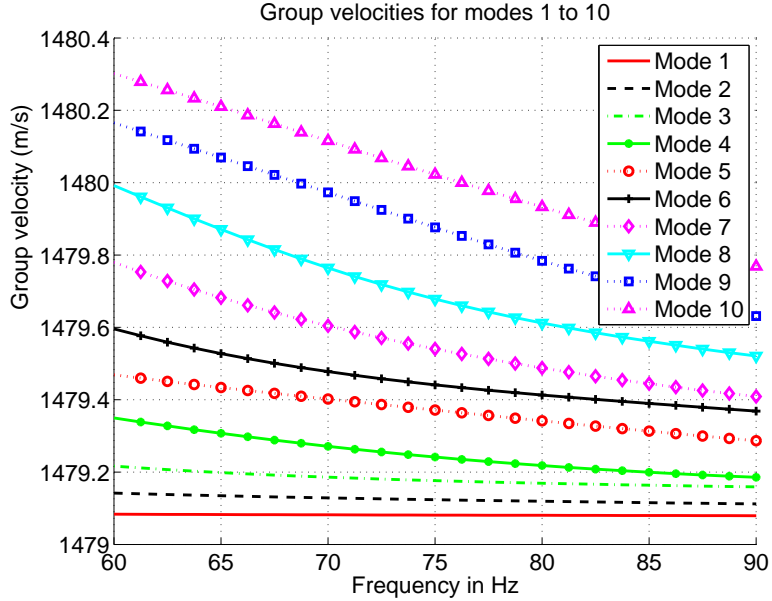


Figure 2.2: The group velocity for the modes shown in figure 2.1. Note that the group velocity varies as a function of mode number and frequency.

wavenumbers  $k_m$  vary as a function of frequency which causes the group velocities of the modes to vary with frequency. Figure 2.2 shows a plot of the group velocities for frequencies between 60 Hz and 90 Hz for the modes plotted in Figure 2.1. A simple calculation based on the group velocities for the 60 Hz to 90 Hz in Figure 2.2 gives the times of arrival plotted in Figure 2.3 for ranges of 50 km and 250 km. Figure 2.3 shows that the amount of dispersion within each mode increases with range. The time separation between the modes also increases with range.

### 2.1.2 A deep water broadband simulation example

A simulation for the pressure field in an environment described by the SSP in Figure 2.1 clarifies the relationship of the pressure field to the modeshapes and the mode amplitudes. There are a number of simulation methods used in underwater acoustic modeling. The Parabolic Equation (PE) method and the coupled mode method are the most relevant to this thesis [9]. The following paragraphs provide a brief description of these methods. The PE method is flexible and computationally fast and hence a popular numerical method

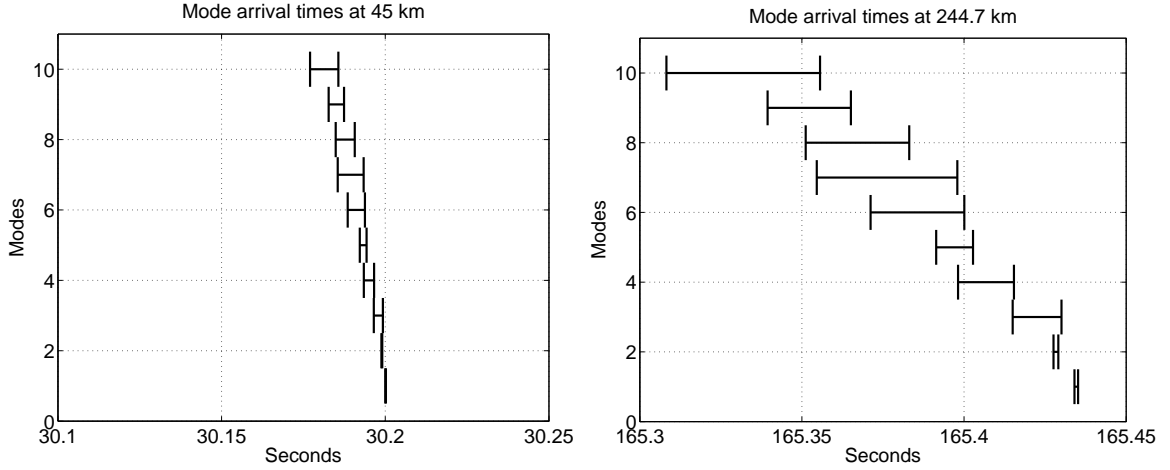


Figure 2.3: The arrival times of modes 1 to 10 for frequencies 60 Hz-90 Hz at 45 km and 244.7 km. The two ranges correspond to LOAPEX T50 and T250 distances. Note that the modes spread out in time as they propagate in range.

to solve range-dependent propagation problems. The inputs to the PE method are the frequency  $\omega$ , the source depth  $z_s$ , the boundary conditions and the sound speed profiles as a function of range. The PE method assumes that the initial field at the source is restricted to a finite set of angles near the source. The PE numerical solver then marches the approximate equation in finite range steps to calculate the pressure field at different ranges. The output of the PE method is the pressure field amplitude and phase at the desired depth resolution.

The coupled mode method, as the name suggests, uses the modal basis functions to calculate the pressure field. The coupled mode method obtains the pressure field via Equation 2.1. This thesis will use both the PE simulations and the coupled mode method alternatively. For PE, the RAM code by Michael D. Collins [10] and for coupled mode simulations, Kraken code by Michael B. Porter [11] is used. The PE and the coupled mode method have their advantages and disadvantages which, will become relevant when discussing mode propagation through range-dependent environments. For now, it is sufficient to know that PE is preferred for solving long distance acoustic propagation problems because of its relatively high computational speeds. This chapter uses only PE simulations.

The SSP in figure 2.1 was input to the PE code which simulated a 30 Hz bandwidth,

800 m deep source transmitting to a 1400 m long array at a range of 3200 km. The narrowband pressure field output by the PE was then inverse frequency transformed to obtain the pressure time series. Figure 2.4 shows the time series. In the simulated pressure field, the low modes are evident in the later arrivals. The final 0.5 s of the simulations contains arrivals that are similar to modes 1 to 5 of figure 2.1. The earlier parts of pressure field contain the higher order modes. The predicted arrival times in Figure 2.3 showed that the high order modes which have greater depth spreads generally arrive earlier than the low order modes. The high order modes constructively interfere to result in the early arrivals. The steep structure of the early part of the pressure field resembles up and down going rays. The early arrivals are thus usually studied in terms of ray theory. On the other hand, the later mode arrivals that consist of low order modes can also be interpreted as a function of shallow angled rays that propagate at relatively small angles to the sound speed axis. Rays and modes can hence be expressed in terms of each other. The principle of using rays to construct the modes and vice-versa is called the ray mode duality [1, 7].

Tomographers typically use different approaches to study the different parts of the pressure field. Ray theory is used to study the early arrivals while the later parts are studied in terms of mode theory. The mode time series was obtained as follows. For an ideal case where the depth is sampled continuously, the pressure field can be projected on to the modes to isolate the different modes from the pressure field. According to Equations 2.1 and 2.4, the mode amplitudes  $a_m(r)$  can be calculated by projecting the modeshapes on to the pressure field such that,

$$a_m(r) = \int_z p(r, z)\psi_m(z)dz \quad (2.6)$$

The simulation in Figure 2.4 had a depth resolution of 2 m which rendered the sampled modeshapes to be orthogonal to each other. The pressure field at different frequencies was projected on to the modeshapes at different frequencies and the narrowband mode amplitudes inverse frequency transformed to obtain the mode time series. Figure 2.4 shows

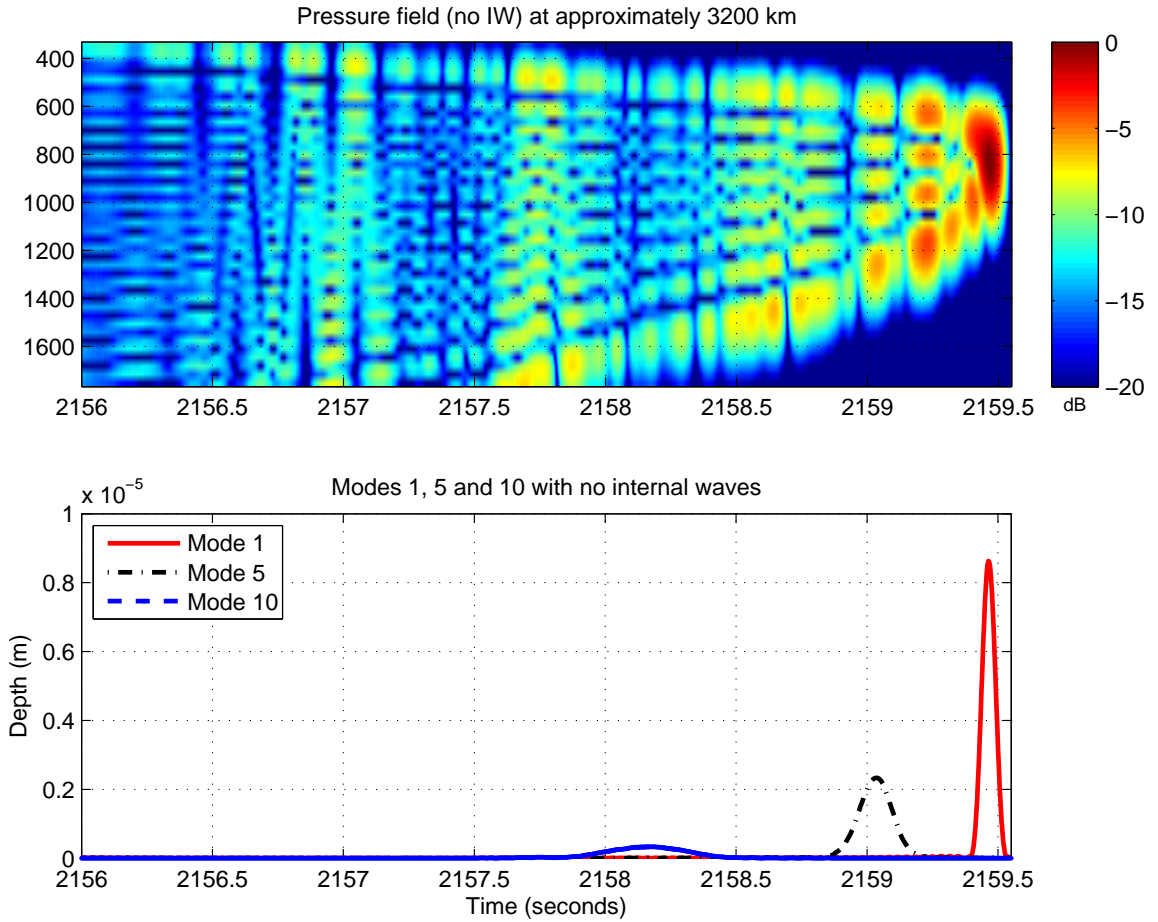


Figure 2.4: Simulated reception at 3200 km. The bottom subplot shows the mode time series for modes 1, 5, and 10. The pressure field and the modes 1, 5 and 10 are dispersed in time.

the mode time series for modes 1, 5 and 10. As expected from section 2.1, in a range-independent environment, modes 1, 5 and 10 arrive at different times and have time spreads in proportion to the mode number. The amplitude of each of these modes is directly proportional to the amplitude of the modes at the source depth. The times of arrival of each of these modes depends on the background sound speed.

The points in this section can be summarized as follows. First, the modes are a complete orthonormal basis set for the pressure field. The modeshape refers to the depth dependent function  $\Psi_m(z)$  and the mode amplitude refers to the complex amplitude  $a_m(r)$ . For a range-independent environment, the narrowband mode amplitudes are a function of the

source excitation level of each mode and the phases are a function of the wavenumber. The simulations showed that for a range-independent environment the different modes arrive at different times. The time spread of each mode is a function of the source bandwidth and the chromatic dispersion of each mode.

## 2.2 Mode propagation through range-dependent environments

The previous section assumed that the SSP was constant across range. The underwater environment is rarely constant across range. In the ocean, there are a number of small and large scale inhomogeneities that induce range dependency. Equation 2.5 describing the mode amplitudes does not hold true for a range-dependent environment. The coupled mode model is used to calculate the range functions for the range-dependent case. The coupled mode model is implemented as follows. The total propagation range is divided into segments such that the SSP is constant within each segment. The modeshapes in each segment are calculated by solving the depth dependent equation (Equation 2.2). The range-dependent functions are obtained by matching the pressure and velocity at the boundaries between the interfaces. The mode signal at range segment  $j + 1$  is obtained by matching the interface conditions is given by,

$$a^{(j+1)} = C^j a^j \quad (2.7)$$

where  $C^j$ , the coupling matrix depends on the local modeshapes  $\psi_m^j$  and the wavenumbers  $k_m^j$  of the range segment  $j$ . The elements ( $c_{lm}^j$ ) of the coupling matrix ( $C^j$ ) are given by,

$$c_{lm}^j = e^{(ik_m r)} \int_z \psi_l^{(j+1)} \psi_m^j(z) dz \quad (2.8)$$

Note that for a range-independent profile,  $C$  is a diagonal matrix. For a range-dependent profile where the modeshapes vary as a function of range, the coupling matrix has non-zero off-diagonal terms, which represents coupling from other modes. This phenomenon is known

as mode coupling. In a range-dependent environment, modes share energy with each other, which is unlike the range-independent case where modes propagate independently of each other. The rest of this section discusses range dependency due to internal waves.

### 2.2.1 The Garrett Munk model

Internal waves, unlike surface waves, occur in the interior of the ocean. The ocean at equilibrium, is stratified in density across depth. When this equilibrium is disturbed by the Earth's rotation, gravity and the buoyancy of the ocean try to restore the water to its equilibrium state. This causes an oscillation in the water about the equilibrium state, which leads to internal waves. Colosi and Brown used the GM model to represent the internal wave induced sound speed perturbations  $\delta c(z)$  as [12],

$$\delta c(z, r, t) = c(z) \left( \frac{\mu}{g} \right) N^2(z) \zeta(z, r, t) \quad (2.9)$$

where  $\mu = 24.5$  is a dimensionless constant,  $g$  is the acceleration due to gravity and  $N(z)$  is the buoyancy profile across depth. Garrett and Munk used observations from multiple sources to derive the Garrett-Munk (GM) model for the internal wave induced displacements  $\zeta(z, r, t)$  [13, 14]. According to the GM model, the displacement  $\zeta(r, t)$  in range  $r$  and time  $t$  can be written as a linear combination of depth-dependent internal wave modes  $W(z)$  such that,

$$\zeta(z, r, t) = \sum_{k,j} G(k, j) W(k, j, z) e^{i(kr - \omega(k,j)t)} \quad (2.10)$$

where  $j$  is the internal wave mode number,  $k^1$  is the wavenumber and  $\omega$  is the frequency. Each of the internal wave modes  $W(z)$  satisfy the equation,

---

<sup>1</sup>The internal wavenumber  $k$  is different from the acoustic mode wavenumbers  $k_m$  discussed earlier in this chapter.

$$\frac{\partial^2}{\partial z^2}W(z) + \left( \frac{n^2(z) - \omega^2}{\omega^2 - \omega_i^2} \right) k^2 W(z) = 0 \quad (2.11)$$

The coefficients  $G(k, j)$  are complex Gaussian random variables, that satisfy the spectrum  $F(j, \omega)$  such that,

$$F(j, \omega) = \frac{2B^2EN_0f}{\pi MN(z)\omega^3} (\omega^2 - f^2)^{\frac{1}{2}} \frac{1}{(j^2 + j_*^2)} \quad (2.12)$$

The various quantities in the GM spectrum  $F(j, \omega)$  are

- $\omega$  : Angular frequency of internal waves
- $j$  : Internal wave mode number
- $j_*$  : 3 constant
- $E$  :  $6.3 \times 10^{-5}$
- $f$  :  $2\Omega \sin(\text{latitude})$ ,  $\Omega = 2\pi$  radians per day, the angular velocity of the earth
- $B$  : approximately 1 km, the thermocline depth scale
- $N_0$  : Surface extrapolated buoyancy frequency
- $N(z)$  : Buoyancy profile
- $M$  : Normalization constant

Equation 2.12 models the depth and range dependence of internal waves. At a global scale, the internal waves are highest at the equator and decrease towards the poles. The horizontal correlation scales of internal waves are on the order of tens of kilometers. The overall depth structure of the internal wave effects are determined by magnitude of the buoyancy profile at each depth. The buoyancy profile peaks at the shallow depths and decreases at much deeper depths. Since the depth of the ocean is around 5000 m, the depth scales of the internal waves are much shorter than the range scales. The frequency scales of internal waves range from the earth's rotational frequency to the buoyancy frequency  $N(z)$ .

### 2.2.2 A simulation example for mode propagation through internal waves

The following broadband simulation example illustrates the effects of internal waves on modes. Sound speed perturbations due to internal waves that obey the GM spectrum described in Section 2.2.1 were simulated using a method given in [12]. The simulated perturbations were added to the background SSP in Figure 2.1. The PE method simulated the pressure field in the range-dependent environment. Figure 2.5 shows the results of a PE simulation for one of the internal wave realizations at a range of 3200 km. There is a difference in the pressure field plotted in Figure 2.4 and the pressure field in Figure 2.5. Figure 2.5 also shows the mode time series that was obtained by projecting the pressure field on to the modeshapes. Figure 2.5 shows that internal waves cause additional multipath. The increase in time spread due to multipath is due to cross-modal scattering from other modes. Although this thesis does not deal with travel time estimation at 3200 km, the simulation examples illustrate very well the amounts of multipath due to internal waves.

This section reviewed mode propagation in range-independent and range-dependent environments. Different approaches to numerical modeling were discussed. The PE method was used to simulate propagation through range-independent and range-dependent environments. The simulations showed that propagation through internal waves induces mode coupling which causes interference among modes. Internal waves could thus cause problems for tomography. The next section reviews the mode tomography that has been performed to date.

## 2.3 Mode tomography and the problems of internal waves

The goal of this section is to briefly discuss mode tomography and difficulties of implementing tomographic inversions in the presence of internal wave scattering. This section discusses how the low order modes can be used for tomography and consists of three parts. The first part explains the rationale for using modes for tomography. The second part discusses the few instances when mode tomography was performed and the observables that were used in

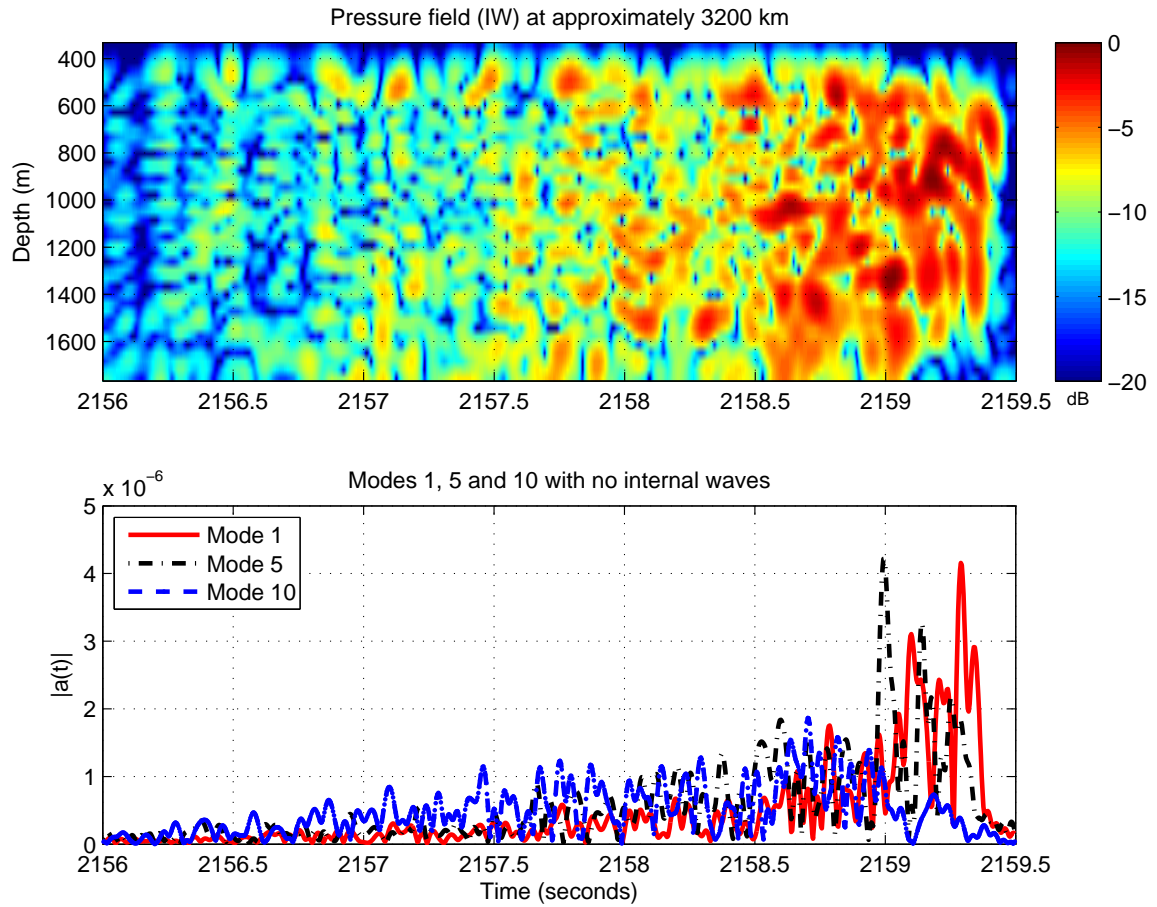


Figure 2.5: Simulated LOAPEX reception at 3200 km. The top subplot shows the pressure time series across depth. The bottom subplot shows the mode time series for modes 1, 5 and 10. The finale of the pressure field (top subplot) shows scattering. Modes 1, 5 and 10 contain significant multipath.

the inversions. The discussion mainly concentrates on the observables that were used and the quantities that were measured. The exact details of the inversion schemes are given only in later chapters. The last part explains the challenges for mode based tomography due to internal waves.

Ray based tomography as suggested by Munk [1] relies on inverting the arrival times of different rays for sound speed. The different rays sample different depths of the water column thus the entire sound speed across depth can be estimated. Section 2.1 showed that the later arrivals in the pressure field can be explained better in terms of modes. The modes sample the midwater depths and arrive at different times and could be used for tomographic inversions for the midwater depths. The low modes, unlike the rays, are separated in wavenumber and thus the modal phases estimated with a linear array could be used in tomographic inversions. Ray theory is only a high frequency approximation to propagation and at low frequencies, the modes are a more suitable basis. Low frequencies propagate over longer distances and are more applicable to long range tomography. Mode based tomography thus enables sound speed inversion at axial depths and make tomography possible over longer distances.

With the view that modes can improve sound speed resolution, Munk and Wunsch [15] suggest using a hybrid approach that takes into account both ray and mode travel times to invert for the sound speed profile. They also suggest a perturbation-based approach where the difference in travel times with respect to a reference profile is used to quantify sound speed variations as a function of depth. Shang used simulations of a perturbation based inverse to show that the low modes can be used to measure eddies [16]. Shang's method [16] consisted of using both narrowband and broadband simulations through a range-independent ocean perturbed by an eddy of range scale 500 km. The simulations showed that either the perturbations in the phases of the narrowband signal or the perturbations in arrival times of the broadband signal of modes 1 to 7 can be used to invert for the depth structure and the average strength parameter of the eddy.

Underwater acoustics can also be used to infer the bottom properties. At short ranges,

the bottom bounce is quite strong and can be detected. The attenuation and the phase change suffered by the bottom bounce depends on the bottom properties and thus the bottom bounce can be used to measure the bottom properties. This procedure is known as geo-acoustic inversion. Ray based tomography for shallow water is complicated because of the significant amount of multipath. A mode based approach has thus been used to estimate the bottom properties in shallow water. References [17], [18] and [19] are some of the main references for shallow water geo-acoustic inversions.

Mode tomography has been performed with data collected from experiments. The two prominent instances are the mode tomography that was performed on data collected during experiments are the Norway Sea experiment [20] and the Greenland Sea experiment [21]. The Norway Sea experiment used a ship suspended continuous wave source of frequency 105 Hz to make acoustic transmissions to a 560 m long vertical array with 29 hydrophones. Transmissions were recorded at two different ranges: 55 km and 105 km. The data recorded on the VLA was used to estimate the modal phases and these phases were used to estimate the range averaged sound speed along the two propagation paths. The sound speed obtained from the modal phases agreed with SSP obtained from a ray-based inversion and with spot measurements along the path. Mode tomography was also performed with data collected during the Greenland Sea experiment in 1989 [21]. This experiment used a 6 hydrophone VLA to measure broadband receptions from a source located 106 km away. The acoustic signals received at the array were used to obtain the mode time series of modes 1 to 6. The times of arrival of each mode at different frequencies were used to obtain the group velocities of the modes. The group velocities of the modes and the arrival times of the rays were inverted to measure the average sound speed of the propagation path. For the arctic profile, the low modes are concentrated near the surface. Two types of tomographic inversions were considered. One scheme used only ray data while the second scheme used both ray and mode data. Compared to an inversion scheme based only on rays, the mode data significantly improved the near surface resolution. Mode tomography performed more recently includes the tomography from the NPAL 1998 experiment [22]. The NPAL 1998

experiment consisted of 5 VLAs spread across a 1.1 km distance. Voronovich and Ostashev in [23] showed that the phase differences of the modes at the different arrays could be used to measure the horizontal refraction angle suffered by the acoustic signals. The refraction angle measured via modes agreed with the refraction angle obtained using ray measurements.

### **2.3.1 Challenges to mode tomography due to internal waves**

In spite of the fact that modes have the potential to improve tomographic inversions very few experiments have incorporated mode tomography. There are several reasons for this. First, Munk and Wunsch's original formulation for mode tomography assumes that the modes propagate adiabatically, implying that for slow range dependence, the modes do not exchange energy [15]. In the presence of internal waves, modes are not adiabatic invariants. Tomographic inversions may suffer significant errors. Internal wave effects accumulate with range and are thus a bigger concern at long ranges. Shang's simulation study did not take into account internal waves [16]. Sound speed perturbations due to internal waves cause phase variations and time of arrival perturbations that would result in errors in the estimation of an eddy. The mode tomography for the Norway Sea experiment [20] was performed only over a range of 106 km. The authors in [20] do mention that their results could be better if internal waves are included in the mode inversion procedure. It should also be noted that the tomographic inverses for Norway Sea experiment and the Greenland Sea experiment were performed only over a range of 106 km and that internal wave effects increase across range. To calculate the average sound speed profile across longer ranges, internal wave effects would have to be reduced or taken into account in the inversion procedure.

There are also experimental limitations to using modes for tomography. At shorter ranges the low modes are not separable in time and thus array processing techniques have to be employed. Deploying arrays at sufficient spatial resolution would result in higher experimental costs. The recent years have however seen more number of experiments which had linear arrays with mode resolving capabilities. Chapter 1 described experiments such

as ATOC, NPAL and LOAPEX, which deployed VLAs with sufficient resolution for mode processing. These recent experiments should motivate more attempts at mode tomography and also help in understanding internal wave effects on modes. In contrast to the no internal wave case, the internal wave affected mode signals are so complicated that there seems to be no straightforward way to pick a time of arrival or phase information and use them in tomographic inversions.

## 2.4 Conclusions

This chapter discussed the fundamentals of underwater sound propagation. The modes are a suitable basis set to describe the pressure field across depth. The mode amplitudes in a range independent environment only undergo waveguide dispersion. However, in a range-dependent environment such as an environment containing internal waves, the coupled mode model predicts multipath due to inter-modal dispersion. The next chapter discusses mode propagation in the presence of internal waves in more detail.

## Chapter 3: A statistical model for the modes at short range

The last two chapters used simulation examples and LOAPEX signals to illustrate the effect of internal waves on modes. This chapter provides more detail about mode coupling induced by internal waves and estimates a statistical model for the effect of internal waves on modes. The organization of this chapter is as follows. Section 3.1 gives additional background on mode coupling and explains the current theories for mode coupling. The current literature does not contain much information on mode statistics at ranges on the order of hundreds of kilometers. This chapter uses simulations to get insights into mode coupling at these ranges. Section 3.2 explains how the simulations were set up to estimate the mode statistics. Section 3.3 estimates the statistics of modes affected by internal waves up to a range of 400 km.

### 3.1 Background on mode coupling

Dozier and Tappert's work is the most widely cited work on mode coupling [5, 6]. Those authors used the coupled mode equations (Equations 2.7 and 2.8) to derive the "coupled power" equations that enable a study of mode coupling across range [5]. The coupled power equations are given by,

$$\frac{\partial \xi_n(r, t)}{\partial r} = -i \sum_{m=1}^N \Gamma_{nm}(r, t) e^{ik_{nm}r} \psi_m(r, t) \quad (3.1)$$

The quantities in Equation 3.1 are defined below

$$\xi_n = e^{-ik_n r} (k_n)^{\frac{1}{2}} a_n \quad (3.2)$$

where,

- $a_n$  Mode amplitude with initial conditions  $a_n(0, t) = a_n^0(t)$ ,  $1 \leq n \leq N$
- $k_n$  Mode wavenumber
- $k_{mn}$   $k_m - k_n$

The matrix  $\Gamma_{nm}$  is given by,

$$\Gamma_{nm}(r, t) = \frac{\omega^2}{c_0^2 (l_n l_m)^{\frac{1}{2}}} \int dz \frac{\delta c(r, z, t)}{c_0} \psi_n(z) \psi_m(z) \quad (3.3)$$

where  $c_0$  is the sound speed at the axis. The matrix  $\Gamma_{nm}$  is equivalent to the coupling matrix in Equation 2.8 except that the integrand in Equation 3.3 is defined in terms of the modeshapes of the background SSP. Dozier and Tappert made what they called certain “dishonest approximations” to the coupled power equations to analyze mode propagation across range and came up with a set of conclusions [5]. The predictions were later verified by performing simulations [6]. The main conclusions were as follows. The coupling matrix depends on the sound speed perturbations  $\delta c(z)$ , which are described by the statistical GM model (Equation 2.12). The elements of the coupling matrix are random and vary with one realization to the other. Thus the scattering contributions from the other modes are a random variable. The coupling contributions from the different modes are determined by the amount of overlap in modeshape  $\psi_m(z)$  in Equation 3.3. The amount of overlap is higher for neighboring modes, which leads to the phenomenon called nearest neighbor coupling where the modes receive more amounts of scattering from the neighboring modes. Dozier and Tappert also predicted that multiple coupling events across range cause the modes to mutually exchange energy, eventually resulting in an equal distribution of energy in all modes. The range at which equipartition is reached is called the “equilibrium range”. Dozier and Tappert also showed that, at equilibrium range, the modes have effectively undergone an infinite number of coupling events and by the central limit theorem achieve Gaussian statistics.

As mentioned earlier, Dozier and Tappert simulated only an approximate version of Equation 3.1. For their 1978 results, Dozier and Tappert were constrained by the available computing resources and were not able to test their predictions using PE simulations. Colosi *et al.* [24] in 1996 performed PE simulations to model the internal wave effects on modes at ranges of 1000 km, 2000 km and 3000 km. The PE simulations showed that apart from multipath scattering, cross-modal coupling also causes a change in the group velocity of each mode. The change in group velocity is due to the exchange of energy among modes that propagate with different velocities. The change in group velocity causes a modal travel time bias. According to Colosi, the travel times of the lower modes (modes 1 to 6) show a negative bias with respect to the background travel time indicating a preference for coupling from the higher modes that travel at a faster velocity. The higher modes showed a positive bias indicating a coupling from lower modes that traveled at a slower velocity. The PE simulations showed that, although mode coupling caused complicated interference patterns, there was some regularity. The lowest modes showed the least time spread and the least travel time bias. The time spread and the bias increased with mode number. The time spread and the travel time bias showed a range ( $r$ ) scaling on the order of  $r^{\frac{3}{2}}$  and  $r^2$ , respectively. Unlike Dozier and Tappert's simulations in [5, 6], Colosi's simulations in [24] treated the bottom as an absorbing bottom which is more realistic. With the absorbing bottom, the modes interacted with the bottom and lost energy as they propagated. Recently, Udovydchenkov and Brown [25] used simulations to show that Colosi's  $r^{\frac{3}{2}}$  predictions for time spreads [24] for the modes caused by internal waves also hold true at ranges typical of LOAPEX.

Dozier and Tappert [5, 6] and Colosi and Flatte [24] noted that the real test of coupled mode theory would be on experimental data. The ATOC experiment (see Section 1.1) conducted in 1995-1996 provided the first opportunity to observe mode signals at megameter ranges and verify some of the predictions. Signals were recorded by two arrays in the Pacific at distances of 3515 km and 5171 km. Wage et al [26, 27] analyzed the broadband mode arrivals received during the ATOC experiment. The signals showed significant fading and

multipath. The time spreads of the modes were significantly greater than time spreads due to chromatic dispersion. The additional time spreads were explained by scattering due to internal waves. The data sets for the modes received at both the ranges had almost the same time spread on the order of 1.5 seconds. The modes had a time coherence on the order of less than 10 minutes. The VLA near Kiritimati and the Hawaii VLA also recorded receptions from the dual frequency Alternate Source Test (AST) source which transmitted at carrier frequencies of 28 Hz and 84 Hz. The AST transmissions facilitated the comparison of mode signals at different carrier frequencies. Wage et.al showed that the time spreads for the 28 Hz source are somewhat smaller than the time spreads for the 84 Hz source [28]. In addition, the 28 Hz mode signals had a longer coherence time of 20 minutes as compared to a 6 minute coherence time for the 84 Hz modes. The shorter time spread and longer coherence time of the 28 Hz signals are due to the fact that internal wave effects are substantially reduced at lower frequencies.

One of the important issues that has not been addressed by any of the studies thus far is the nature of mode coupling at shorter ranges. The rest of this chapter uses simulations to estimate mode statistics at ranges up to 400 km.

## **3.2 Statistics for modes affected by internal waves**

This section uses simulations to model the statistics of the modes affected by internal waves and is organized into three parts. The first part discusses how the simulations were set up. The second part discusses the narrowband statistics from the simulations and the third part discusses the broadband simulation statistics.

### **3.2.1 Setting up the PE and the coupled mode simulations**

A range dependent environment similar to LOAPEX containing internal waves was simulated by adding random internal wave perturbations to a background profile. The background SSP was estimated from archival profiles in the World Ocean Atlas (WOA) [2, 3] for the LOAPEX path (Figure 1.2). Specifically SSPs were computed every 5 km across

Table 3.1: Internal wave simulation parameters

Parameter	Value
Garrett Munk Strength (GM)	.5
$k_{min}$	$\frac{2\pi}{1000km}$
$k_{max}$	$\frac{2\pi}{500m}$
Number of internal wave modes $j_{max}$	150

the 3200 km path from the temperature and salinity profiles in WOA. The profiles were averaged to obtain the background SSP. Internal wave induced sound speed perturbations obeying the Garrett-Munk model (Equation 2.12) were generated by using the method suggested by Colosi and Brown [12]. The internal wave simulations were performed at a range resolution of 100 m using the parameters shown in table 3.1. The IW simulations used an average buoyancy profile derived from WOA data. To simulate a range-dependent environment, the IW sound speed perturbations are added to the background SSP. 50 such range dependent environments were simulated for independent internal wave realizations. Each of the IW simulations was performed at time instants of 0, 200, 400, 800, 1200 and 2400 seconds.

The simulated SSPs were used in coupled mode and PE simulations as follows. Equation 2.7 can be rearranged as follows,

$$a_n^{(j+1)} = \underbrace{a_n^{(j=0)} C_{nn} a_n^{(j)}}_{\text{Unscattered component}} + \underbrace{\sum_{m \neq n} C_{nm}^{(j)} a_m^{(j)}}_{\text{Scattering contribution}} \quad (3.4)$$

According to Equation 3.4, the mode signal affected by internal waves is the sum of two components: the first part which propagates only in the mode and the second part, which consists of scattering contributions from other modes. This thesis refers to the first part as the “unscattered component”. The unscattered component takes into account only the terms along the main diagonal of the coupling matrix and does not include the cross-modal contributions from the off-diagonal elements. Assuming that the sound speed profile

is effectively constant across a range segment ( $\Delta r$ ), the expression for the unscattered component using Equation 2.8 is

$$C_{nn}^j = e^{ik_n^j \Delta r} \int_z \psi_n^{j+1}(z) \psi_n^j(z) dz. \quad (3.5)$$

By recursively applying Equations 3.4 and 3.5 and omitting the phase term in equation 3.5, the amplitude of the unscattered component at range segment  $j + 1$  is given by,

$$|a_n^{(j+1)}|_{unscattered} = a_n^0 \prod_{m=1}^j \int_z \psi_n^{(j+1)}(z) \psi_n^{(j)}(z) dz \quad (3.6)$$

The phase of the unscattered component in range segment  $j + 1$  is given by

$$\angle a_{nn}^{j+1} = k_n^{j+1} \Delta r. \quad (3.7)$$

The modeshapes  $\psi_n^j$  are of unit norm, thus  $|c_{nn}^j| \leq 1$  for all  $j$ . This implies that the amplitude of the unscattered component should exponentially approach zero as  $j$  approaches infinity. However for small values of  $j$ , i.e., for shorter ranges, the amplitude of the unscattered component will be significant. At short ranges, the unscattered component is likely to have a major influence on the characteristics of the mode signal. The unscattered component consists of a single component with a random phase and a random amplitude, whereas the coupled mode energy is the sum of random contributions from other modes. The unscattered component is less complicated, thus somewhat easier to model. Baggeroer and Scheer used PE simulations in a similar study to model the unscattered component [29]. In order to model the decay of the desired mode, the PE simulations were modified as follows. The PE simulations were initialized with a single mode. These authors refer to the initial mode as the “start mode”. For every 50 km, all the other modes other than the start mode were reinitialized to zero. This minimized the cross modal leakage into the start mode. The simulation study using modes 1 and 10 showed that the start mode was coherent

for up to 1000 km. The start mode simulations had the following inaccuracies. Although reinitializing the other modes to zero minimizes the coupled mode energy from other modes it does not completely cancel all the scattering contributions. The start mode simulations used a range spacing  $\Delta r$  of 1 km which are much larger than the minimum wavelengths for internal waves (around 200 m). The larger range spacing could lessen the amount of scattering events across range. The 1000 km coherence length, reported by Baggeroer and Scheer for the unscattered component (start mode) is hence not completely accurate.

Coming back to describing the simulations in this section, the perturbed SSPs from the internal wave simulations were input to the Kraken mode program [11] to calculate the modeshapes for a range spacing of  $\Delta r$  of 100 m. The computed modeshapes for modes 1 to 10 were input to equation 3.4 to calculate the unscattered component ( $a_{nn}$ ) across range. PE simulations using the RAM program [10] was used to calculate the total mode signal  $a_n$  for different values of  $j$ . The rest of this section is organized as follows. Sections 3.2.2 and 3.2.3 discuss the narrowband and broadband statistics for the modes were measured at ranges of 50 km, 100 km, 250 km and 400 km. Instead of describing all the narrowband statistics for all the modes between 1 to 10 we focus on modes 1 and 10 as representative examples.

### 3.2.2 Narrowband amplitude and phase statistics of the mode signals

This section first discusses the amplitude and phase statistics of the unscattered component and then discusses various coherence measures such as time coherence, cross modal coherence and the coherence between the scattered and unscattered parts. All the narrowband statistics are for 75 Hz (the center frequency of the LOAPEX source).

For these simulations modes were initialized with amplitude of one. Figure 3.1 shows the average amplitude of the unscattered component up to a range of 400 km for modes 1 and 10. The simulation shows that the amplitude of the unscattered component decays with range. Mode 1 has a slower rate of decay than mode 10, implying that the unscattered component of mode 1 is less sensitive to internal-wave-induced sound speed perturbations. Figure 3.2

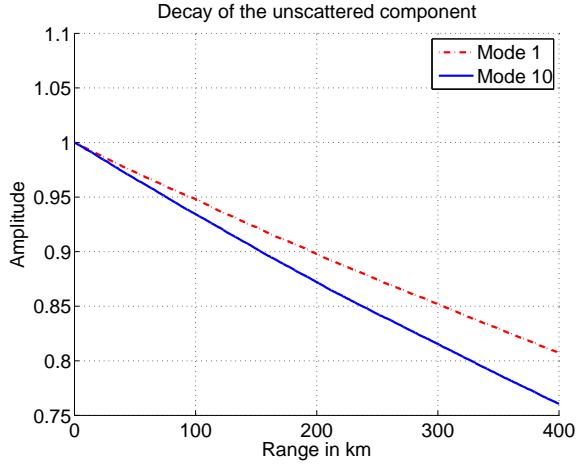


Figure 3.1: The amplitude of the unscattered component for modes 1 and 10 for up to 400 km. Modes 1 and 10 were initialized with an initial amplitude of 1 at the source. The unscattered component decays across range. Mode 1 decays slower than mode 10.

shows the statistics of the mode wavenumbers at 75 Hz for modes 1 and 10. The histogram plots have a Gaussian shape. The wavenumber of mode 1 has the larger variance indicating that it is more sensitive to IW effects than mode 10. A student's T-test [30] was implemented to verify if the mean of the wavenumbers from the simulations is the same as that of the wavenumber of the background profile. The null hypothesis that the wavenumbers of the internal wave perturbed unscattered component had the same wavenumber as that of the unscattered component was accepted at a 5% significance level. Based on the results presented thus far, the narrowband unscattered component has a random amplitude and a random phase. The mean wavenumber of the unscattered component is equal to the background wavenumber.

The rate of decay plot (Figure 3.1) for the unscattered component only explains the amplitude dependence of the unscattered component with respect to range. It does not indicate how the amplitude of the unscattered component compares to the scattered component. The total mode signal consists of both unscattered and scattered components. It is helpful to define a measure of the relative proportions of the unscattered and scattered components. The Signal to Interference Ratio (SIR) defined in the context of the unscattered component is,

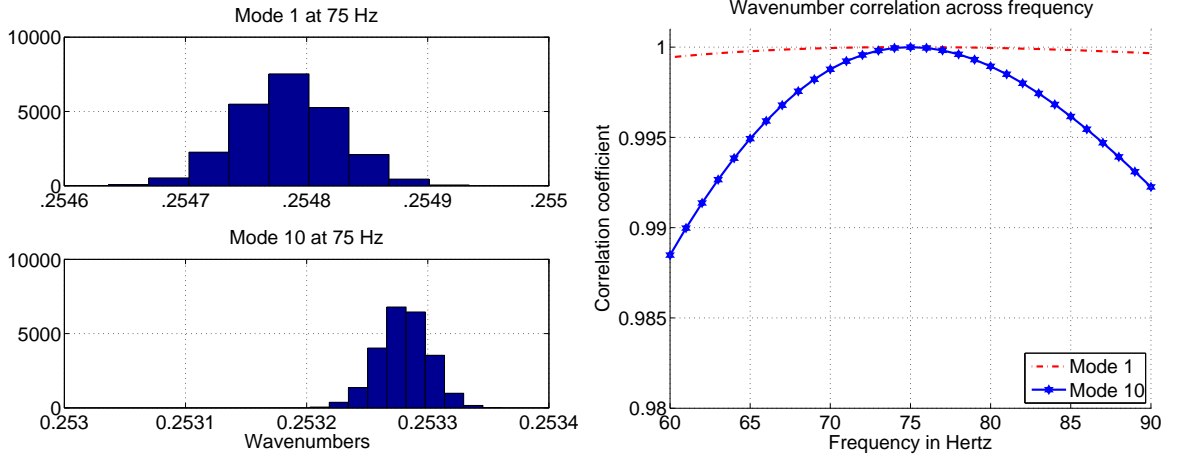


Figure 3.2: The left plot shows the histogram of the wavenumbers of modes 1, 5 and 10 at 75 Hz. The histograms were generated from wavenumbers calculated for a 1000 km range. The wavenumbers are Gaussian distributed. The right plot shows the correlation of the wavenumber at 75 Hz with wavenumbers at frequencies 60 Hz to 90 Hz. The wavenumbers are highly correlated across frequency.

$$\text{SIR} = \frac{\text{Mean energy of the unscattered component}}{\text{Mean energy of the scattered component}} \quad (3.8)$$

The SIR was calculated as follows. All the modes were initialized with their narrowband mode amplitudes at 800 m source depth (LOAPEX source depth). The energies of the unscattered and scattered components were calculated using Equations 3.4 and 2.8 for each simulation. The energies of the unscattered and scattering contributions were averaged across 50 simulations and used in Equation 3.8. Figure 3.4 shows the SIR for modes 1 and 10 at 75 Hz. Mode 1 that was excited at a much higher amplitude has a high SIR sound 15 dB whereas mode 10 which had a null near the source and has an SIR around -5 dB. The unscattered mode 10 is thus buried under scattering contributions from other modes. The SIR values for farther ranges show that although mode 1 initially has an SIR of above 0 dB, scattering contributions eventually take over and the SIR decreases with range. The SIR for mode 1 at 400 km is below 0 dB. The main finding from the SIR plots is that irrespective of the source excitation amplitude, beyond 250 km scattering contributions exceed the unscattered component.

The internal wave perturbed wavenumbers ( $k_m$ ) for modes  $m = 1$  to  $m = 10$  for a given range segment across different internal wave realizations were calculated from Kraken. Figure 3.5 shows that the perturbations between the different modes are highly correlated. Figures 3.7 and 3.8 show the narrowband time coherence of the PE mode signal and the unscattered component at 75 Hz. Figure 3.2 showed that the wavenumber of mode 1 is the most sensitive to perturbations due to internal waves. The unscattered component for mode 1 is expected to decorrelate faster with time than mode 10. The time coherence of the total mode signal is a function of the time coherence of the different modes that couple into it. Assuming predominantly nearest neighbor coupling, the scattered part of mode 1 mostly contains mode 2. The sensitivity of modes 1 and 2 (not shown here) to internal wave perturbations are quite similar which leads to the the time coherence of the unscattered and the total mode signal look almost identical. On the other hand, mode 10 has two neighboring modes 11 and 9 contributing to the scattering energy. The scattering energy for mode 10 consists of the sum of random contributions of two modes, whereas the unscattered part has only one mode. Modes 9 and 11 interfere to have a time coherence less than the unscattered part of mode 10.

Chapter 2 showed that the overall pressure field is a combination of the modes and thus the cross correlation of the different modes has implications for the stability of the whole pressure field. Figure 3.3 shows the narrowband cross correlation among modes 1 and 10 at ranges of 50 km, 100 km, 250 km and 400 km. Modes 1 through 10 have a significant ( $>.5$ ) cross modal coherence at 50 km. At 250 km, modes 6 to 10 are coherent with each other. At 400 km all the modes are uncorrelated with each other. The high coherence between modes at short ranges shows that that Dozier and Tappert's assumption on which some of Dozier and Tappert's conclusions are based is false for ranges less than 250 km. It is also worth noting from Figure 3.3 that the higher modes decorrelate slower than the low order modes. Figure 3.6 shows the narrowband cross-correlation of the unscattered component with the scattered component. The scattered and unscattered components are uncorrelated at all ranges.

The important conclusions about the narrowband mode statistics are as follows. The unscattered component is a signal with random amplitude that decays exponentially with range and has a random phase. The wavenumber of the unscattered component is Gaussian and has a mean about the wavenumber of the background environment. Comparing the amplitude and the phase of the unscattered component, the amplitude of unscattered mode 1 decays slower across range than mode 10 (Figure 3.1). In contrast, the phase of mode 1 is more sensitive to internal wave effects (Figure 3.2). The higher sensitivity of the phase of mode 1 has implications for both narrowband and broadband time coherence. For the low modes, Dozier and Tappert's assumption that cross-correlation between modes is zero does not hold true until 400 km.

### Narrowband cross-modal correlation

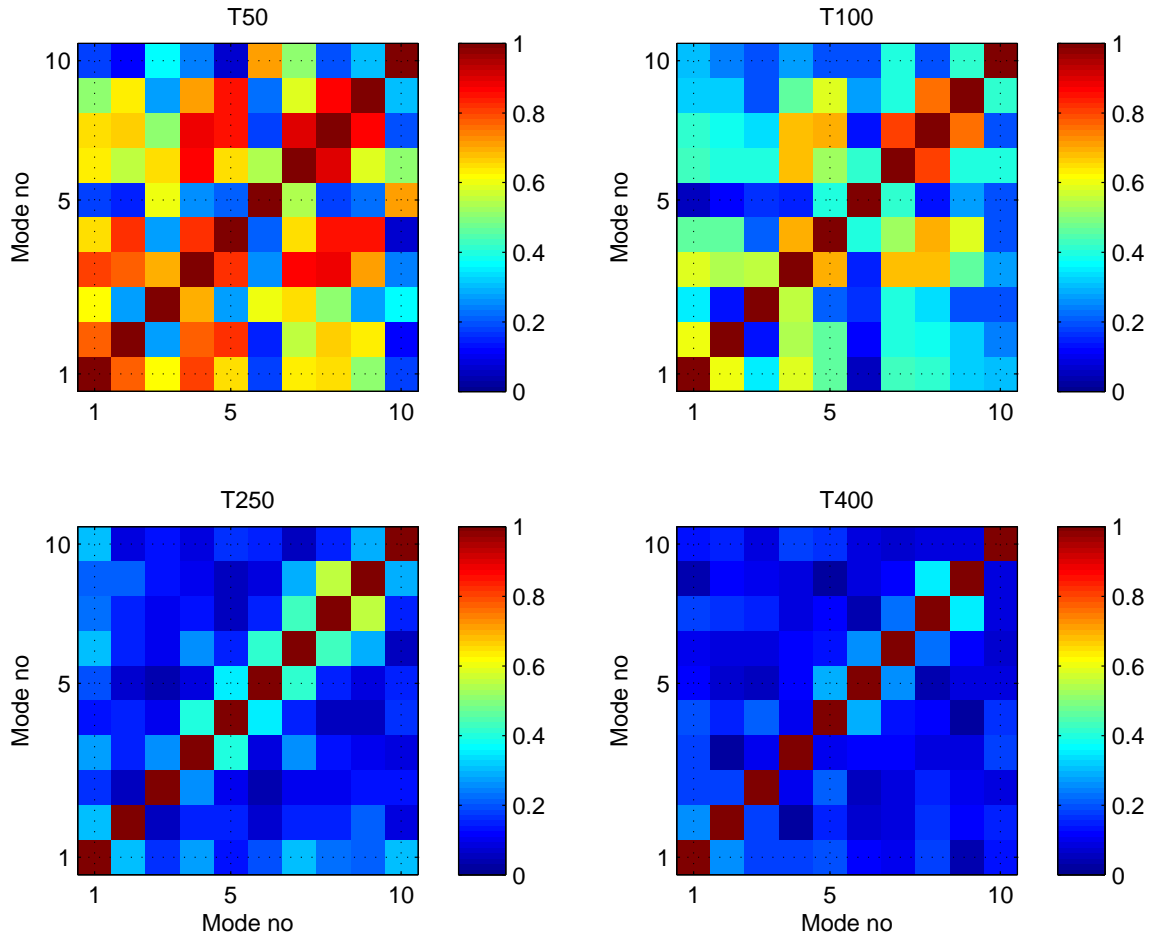


Figure 3.3: Cross coherence between modes 1 to 10 at 75 Hz across range. At 50 km the modes are correlated with each other. The modes however decorrelate with each other as they propagate farther in range.

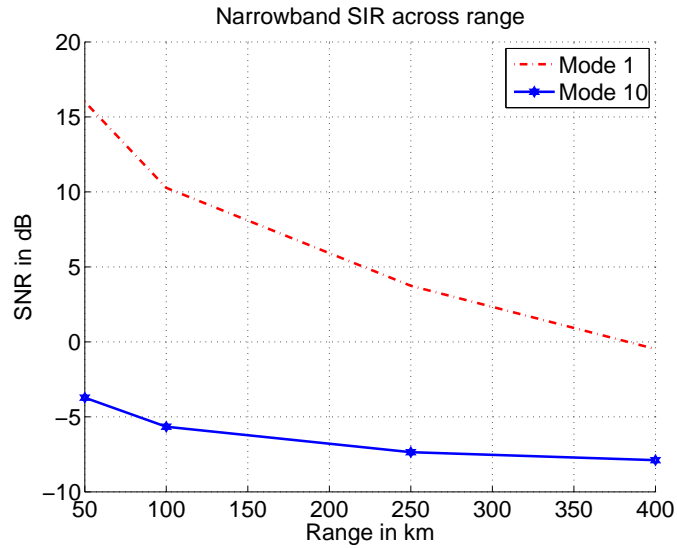


Figure 3.4: SIR of the unscattered component of modes 1 and 10 obtained via narrowband simulations at 75 Hz. Plot includes the effect of the source excitation amplitudes and the  $\frac{1}{\sqrt{r}}$  dependence across range. The modes were excited at amplitudes proportional to the mode amplitudes at the LOAPEX source depth of 800 m. Mode 1 was strongly excited while mode 10 was not. Irrespective of the source excitation level, both the modes have an SIR of below 0 dB at 400 km.

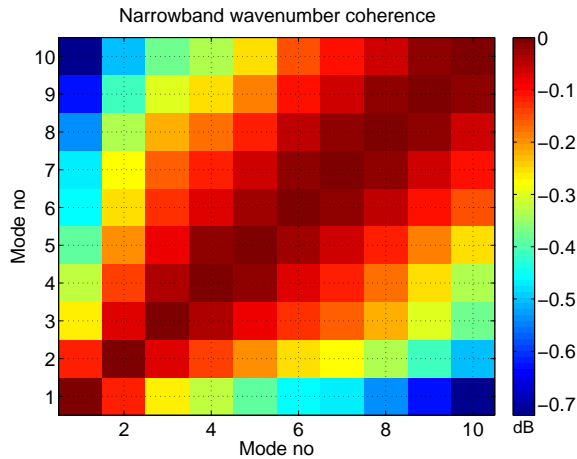


Figure 3.5: The cross coherence of the wavenumbers of modes 1 to 10. The wavenumbers show significant cross-correlation.

Narrowband cross-coherence between scattered and unscattered parts of the mode signal

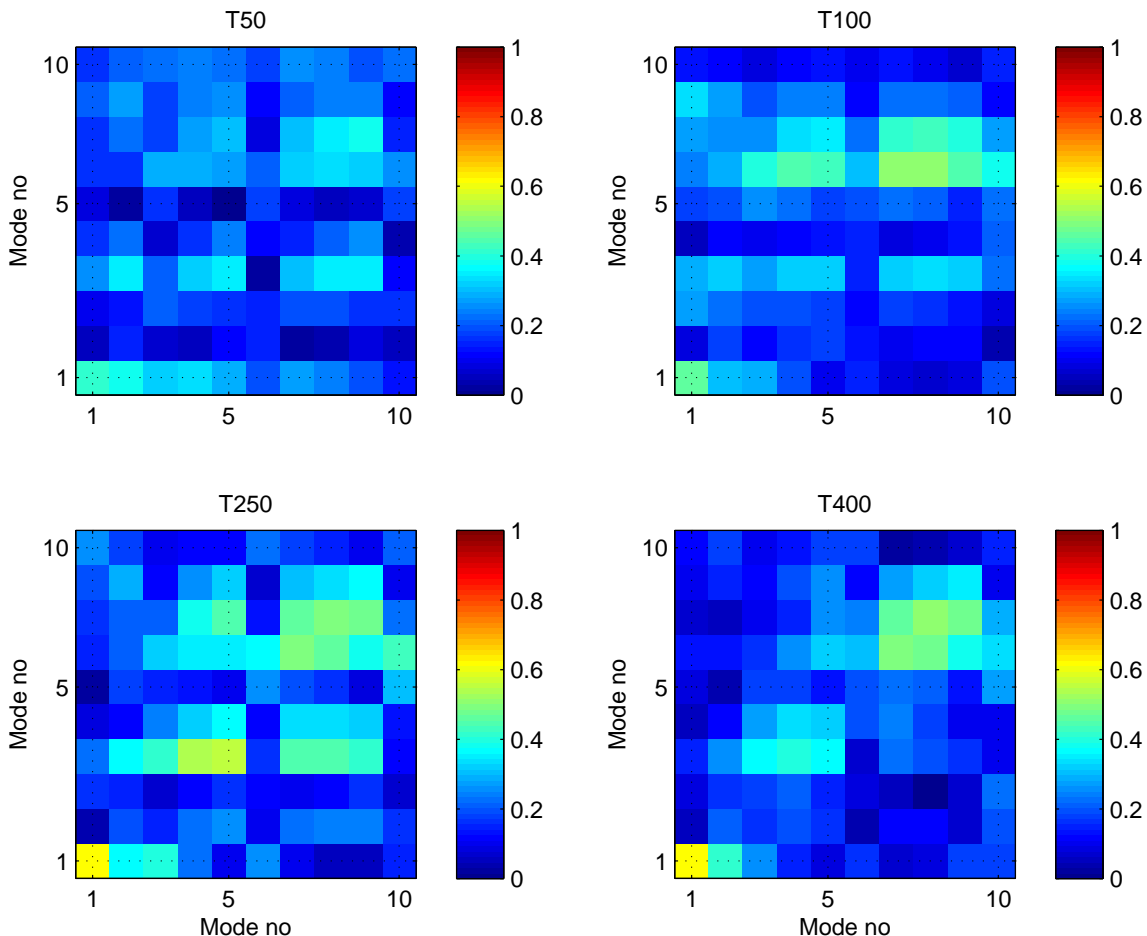


Figure 3.6: Cross coherence of modes 1 to 10 at 75 Hz between the scattered and unscattered parts of the mode signals. The unscattered and scattered parts of the modes are uncorrelated with each other.

### 3.2.3 Broadband statistics for modes affected by internal waves

Equation 2.5 in the last chapter showed that for a no internal wave case, the narrowband mode amplitudes are directly proportional to the source excitation amplitudes. Internal waves at the source perturb the SSP at the source, which in turn perturbs the mode excitation spectrum. Figure 3.9 shows the variations in the source spectrum for modes 1 and 10. The error bars indicate the variance of the amplitudes. Mode 10 in comparison to mode 1 is excited at a much lower level. The variance for mode 10 is greater than for mode 1. Based on Figure 3.9, the source excitation amplitudes of mode 10 are more sensitive to

### Mode 1 at 75 Hz

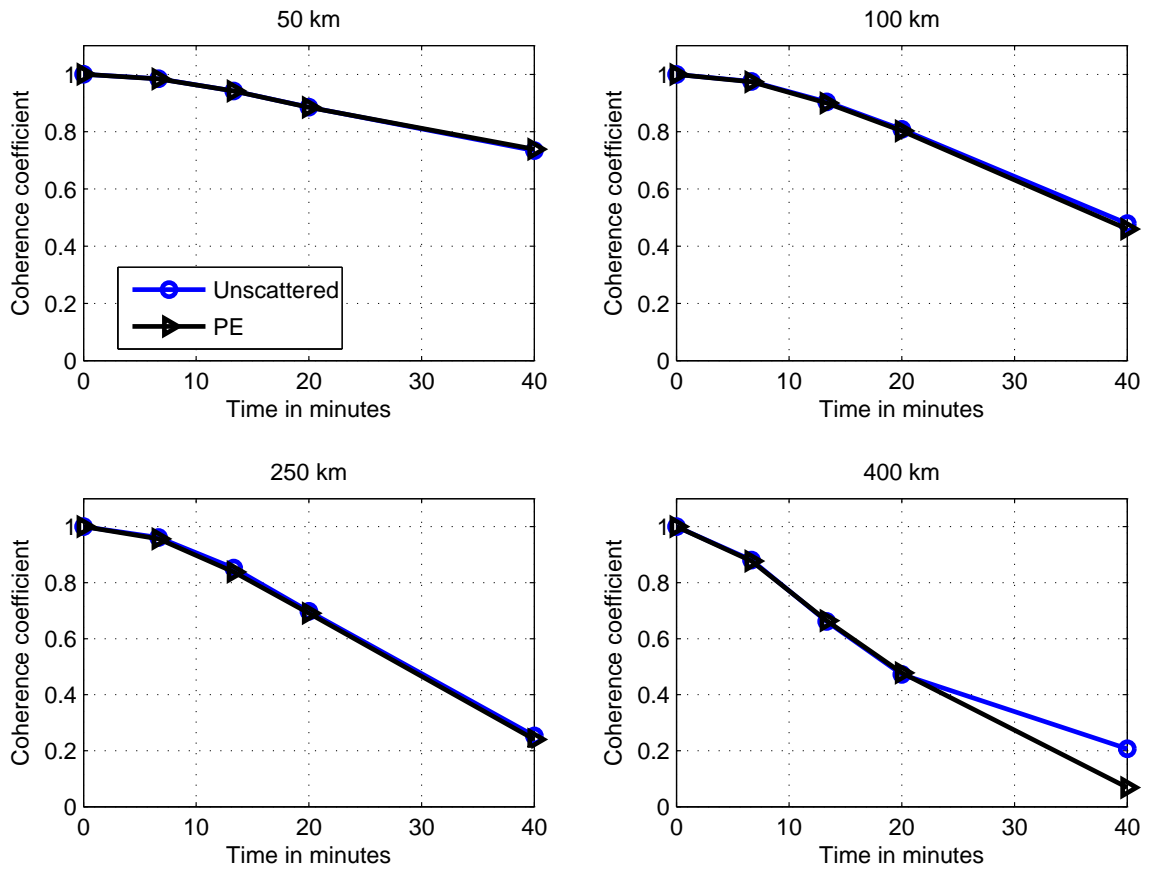


Figure 3.7: The time coherence of mode 1 at 50 km, 100 km, 250 km and 400 km. For mode 1, the unscattered and the scattered mode have similar coherence times at all ranges.

### Mode 10 at 75 Hz

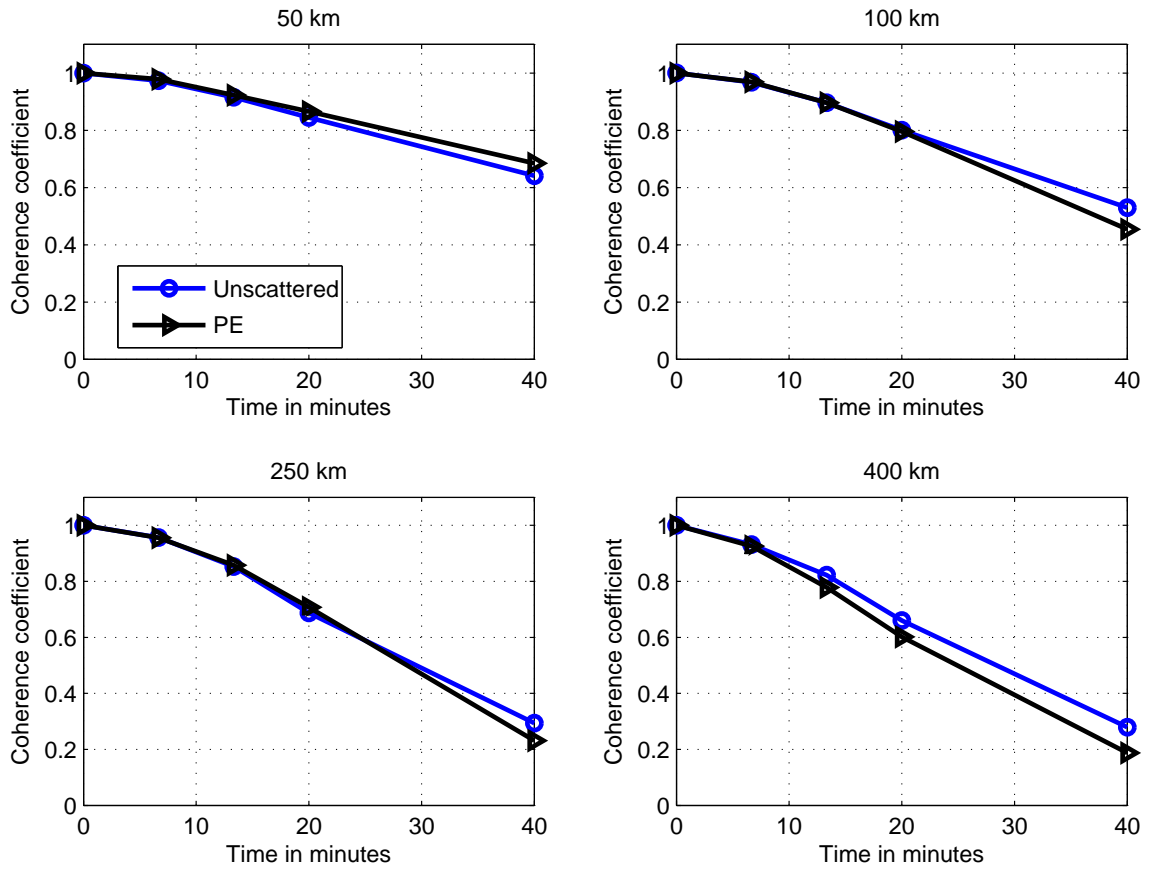


Figure 3.8: The time coherence of mode 10 at 50 km, 100 km, 250 km and 400 km. The unscattered mode is more coherent than the scattered mode. The difference in coherence times between the unscattered mode and the scattered mode increases with range.

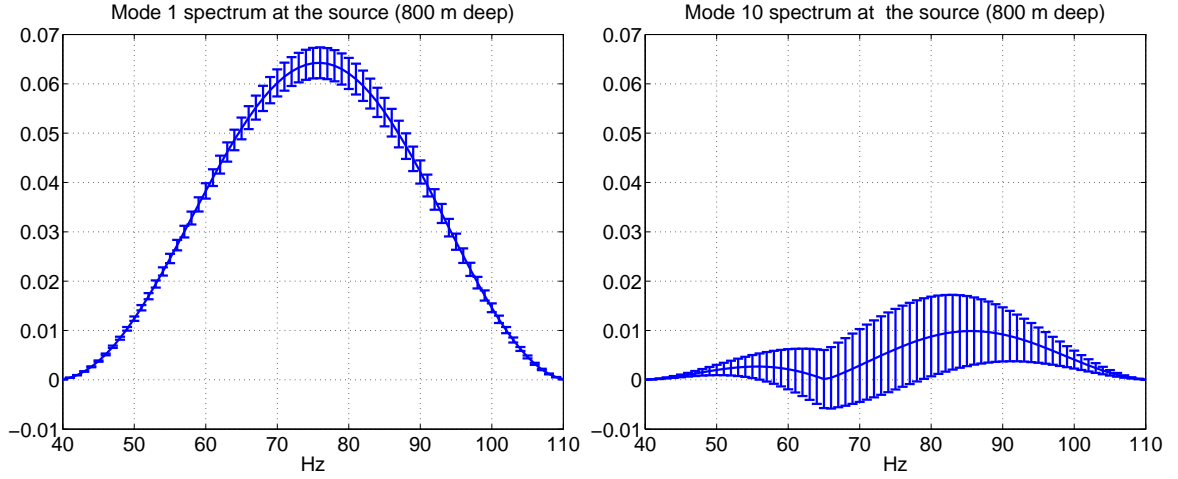


Figure 3.9: The absolute value of the source excitation spectrum of modes 1 and 10. The source depth was set to 800 m (which is the LOAPEX source depth). The error bars, indicate the variance of the amplitudes. At 800 m source depth, the variance in mode 10 amplitudes are greater than mode 1.

internal wave perturbations. Equation 3.6 indicates that the amplitude of the unscattered component depends on the initial source amplitude and the inner product of the mode-shapes at different ranges. Figure 3.10 compares the source excitation spectrum with the spectrum of the unscattered component for modes 1 and 10 for two different internal wave realizations. This section calls the two internal wave realizations as ‘IW realization 1’ and ‘IW realization 2’. The background spectrum for mode 1 is symmetric with respect to the center frequency 75 Hz. The spectrum of the unscattered component in comparison to the background spectrum has a higher amplitude for lower frequencies. This can be explained as follows. As mentioned earlier internal wave effects decrease as a function of frequencies, which implies that the unscattered component decays slower for low frequencies. The amplitude of the unscattered component is thus comparatively higher for lower frequencies. The overall structure of the spectrum of the unscattered component however still resembles the structure of the source excitation spectrum. For mode 10, the source excitation spectrum contains a null for both the simulations. The location of the null varies from one internal wave realization to the other. The location of null in the unscattered component matches the excitation spectrum.

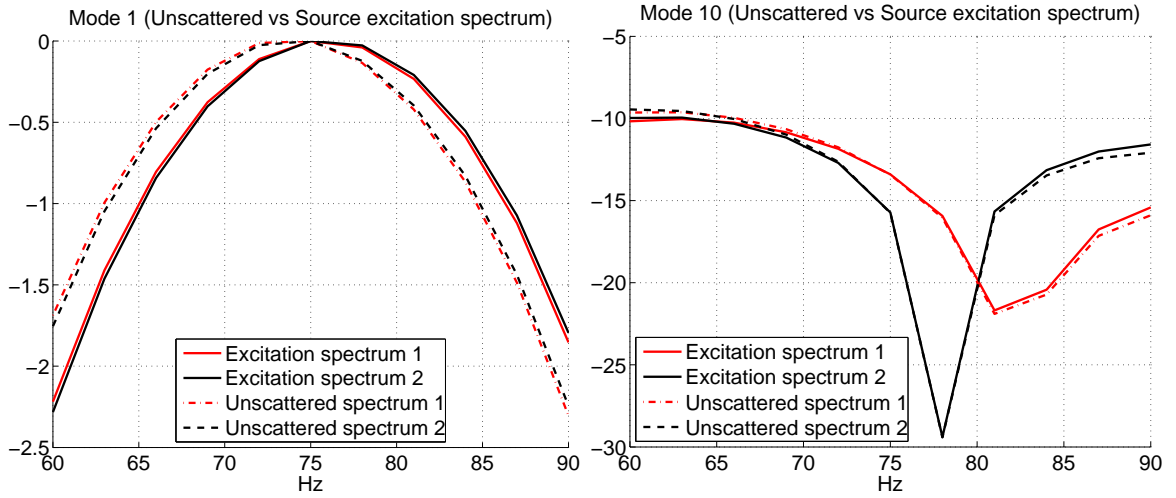


Figure 3.10: The source excitation spectrum and the spectrum of the unscattered spectrum of modes 1 and 10. Mode 1 excitation spectra is symmetric with respect to the center frequency (75 Hz). Mode 10 excitation spectra contains nulls. The location of the nulls varies between the two IW realizations. The unscattered component for modes 1 and 10 is similar to the excitation spectrum.

While the mode amplitudes at the source mostly determine the amplitude spectrum, the wavenumbers of the respective mode determine the phase variations across frequencies. Figure 3.2 shows the phase coherence of the wavenumbers across frequency. Figure 3.2 shows that the mode wavenumbers are highly correlated across frequency. This implies that internal waves perturb the phase of the unscattered component but the different frequencies still constitute one coherent arrival. The net effect of the internal waves on the unscattered component is to randomize the amplitude and to perturb the time of arrival. Based on the results presented thus far, the broadband unscattered component is predicted to be a single arrival with a time of arrival that varies with the internal wave realization. The amplitude spectrum of the unscattered component arrival depends on the source excitation spectrum. Figure 3.11 shows the plots for the unscattered mode and total mode signal for modes 1 and 10 at 50 km and 250 km for IW realizations 1 and 2. The unscattered component for mode 1 consists of a single arrival. The unscattered mode 10 at 50 km corresponding to internal wave realization 2 contains a null in the arrival while the mode arrival for internal wave realization 1 does not contain a null in its arrival. The null in the mode arrival is because of

the deep null in the frequency spectrum in Figure 3.10. Mode 1 at 50 km and 250 km, for both the realizations consists of a single peak and resembles the unscattered component. The peak arrival of mode 1 at 250 km arrives earlier than the unscattered component. The negative time bias is due to the effects of coupling from the higher modes which have a faster velocity (as discussed in Section 3.1). The mode 10 time series resembles the unscattered component. The null in the mode 10 signal for internal wave realization 2 is similar to the null in the unscattered mode time series. At 250 km, the mode signal for the internal wave realization 2 does not contain the null it did at 50 km. The total mode signal for both the realizations differs from the unscattered component. Based on the results presented until now, the following can be said about the mode signal at short ranges. The internal waves perturb the mode excitation spectrum and the phase. On one hand, the perturbations to the excitation spectrum cause changes to the received mode time series. On the other hand, the perturbations to the phase induce travel time wander in the mode time series.

The PE simulations were averaged to calculate the mean spectrum of modes 1 to 10 at different ranges. Figure 3.12 compares the spectrum of modes 1 and 10 at different ranges, to the background spectrum. For modes 1 and 10, the mean spectrum at 50 km is similar to the background source excitation spectrum. The null in the T50 mode 10 spectrum occurs at the same location that the background spectrum has a null. At T100, the average spectrum still contains a null. At T250, and T400, the nulls for mode 10 are completely filled up. In modes 1 and mode 10 more nulls starts appearing at T400. The new nulls at T250 and T400 for mode 10 are due to multipath fading induced by scattering. Figure 3.13 shows the mean spectrum for modes 1 to 10. At T50 all the modes 1 to 10 in Figure 3.13 are similar to the background source spectrum. Other than mode 10, the average spectrum for mode 6 also has a null that matches the null for the background spectrum. Similarly at T100, the nulls for modes 6 and 10 average spectrum still exists, but the average spectrum is skewed to the left. At T400 all the modes contain nulls in their spectrum. The main conclusion from the broadband spectrum plots is that for a range of up to 100 km, the mean mode spectrum closely matches the background excitation spectrum.

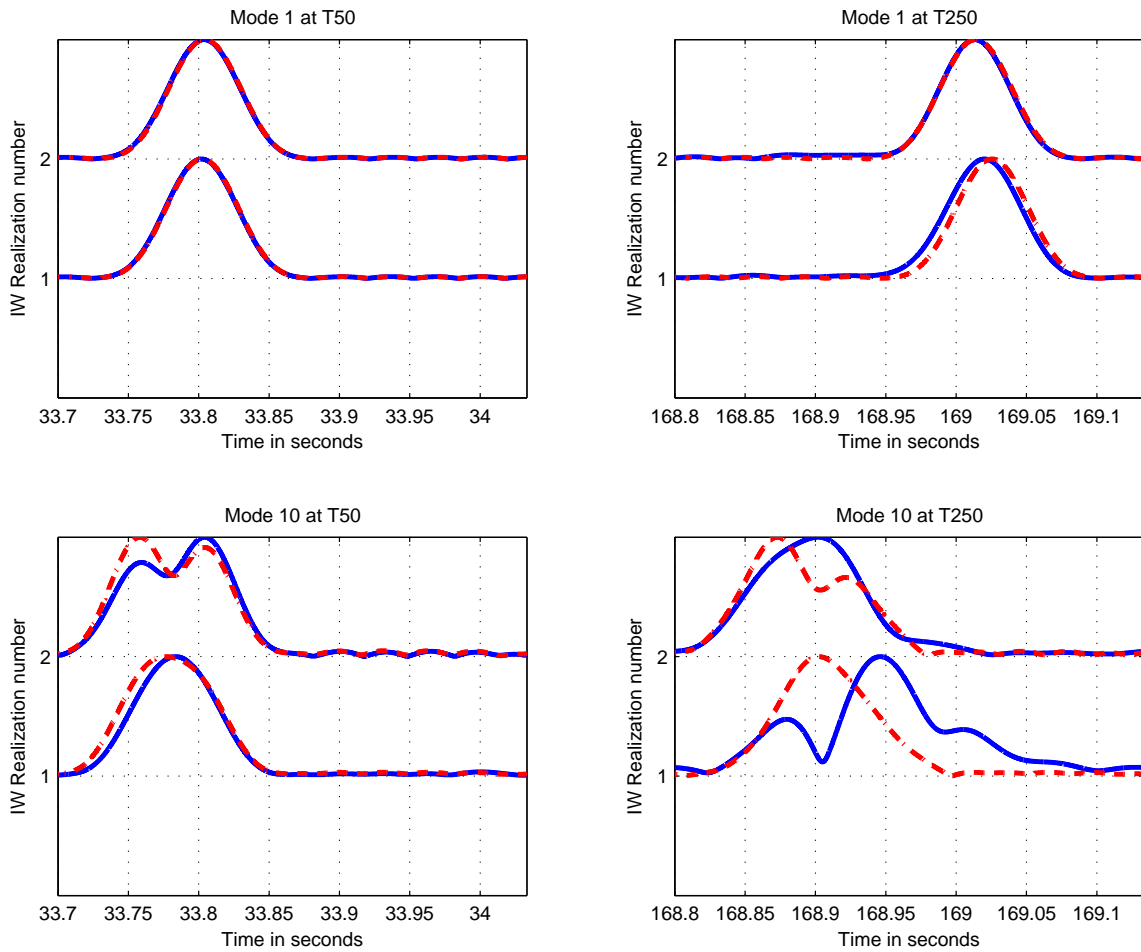


Figure 3.11: Modes 1 and 10 for two different realizations (blue '-' for the mode signal and red '-' for the unscattered signal). For modes 1 and 10 at 50 km, the unscattered component has a significant influence on the total mode signal. That does not hold true at 250 km.

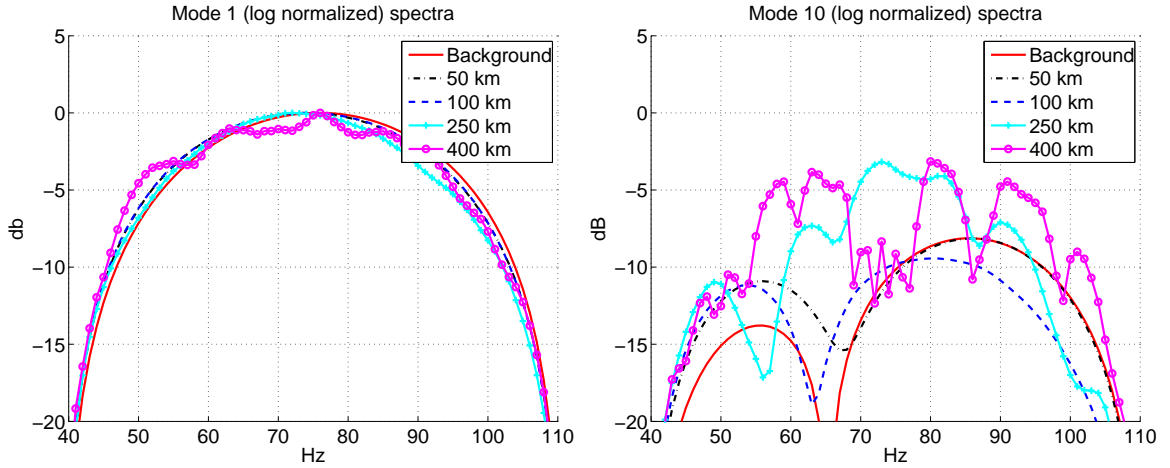


Figure 3.12: The normalized spectra for mode 1 and 10 at ranges of 50 km, 100 km, 250 km and 400 km. At 50 km and 100 km, modes 1 and 10 have a spectra that is close to the background spectrum. At 400 km, nulls appear in the spectrum for modes 1 and 10. Mode 10 appears to have deeper nulls than mode 1.

The travel time of mode 1 for each simulation were estimated by picking the peak (maximum) of the broadband time series. Figure 3.14 shows the standard deviation in peak times of arrival for mode 1 at ranges of 50 km, 250 km and 400 km obtained from the PE simulations. The standard deviation of the arrival times for the PE modes are compared with travel time variance of the broadband unscattered time series and the travel time predictions for the narrowband unscattered component. For up to 250 km, the standard deviation in the travel times is the same as that of the unscattered component. This shows that the unscattered component statistics are useful to predict the statistics of the total mode signal. However at 400 km, the travel time standard deviation for mode 1 is much greater than the unscattered component. This implies that for range greater than 250 km, the broadband unscattered component is insignificant and the scattering contributions dominate the mode 1 signal. As the simulations demonstrated, the mode 10 time series contains two peaks, which causes problems with peak picking approach to travel time estimation. The travel time estimation methods and the travel time statistics for mode 10 are discussed in Chapter 5.

In order to suppress the internal wave interference in a desired mode, tomographers typically average the mode signals across receptions received at different times. The efficacy

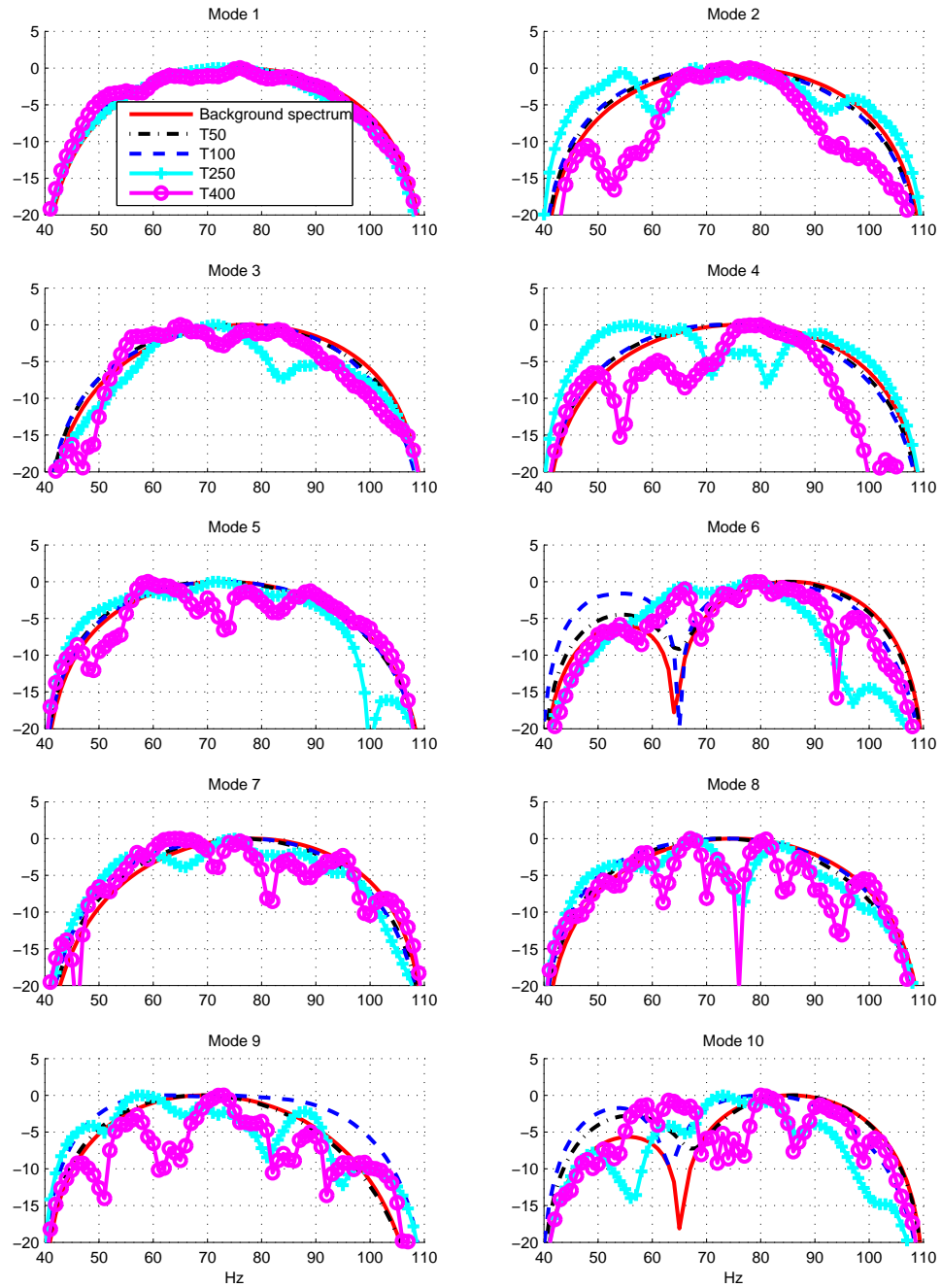


Figure 3.13: Mode (log normalized) spectra for modes 1 to 10 at different ranges. At 50 km and 100 km, the mean mode spectrum for each mode is similar to the background spectrum. At 250 km and 400 km, the mode spectra contain more scattering. At T400, mode 1 shows the least fading.

of this method depends on the stability of the internal wave induced noise with respect to the desired mode signal. Section 3.2.2 discussed the narrowband time coherence of the mode signals. In order to analyze the broadband loss/gain induced by averaging, this section uses the following measure. The loss in averaging for the broadband mode signal across receptions is defined as,

$$\text{Loss in averaging} = \frac{\text{Maximum value of the mean (time average) of the mode signals}}{\text{Mean of the maxima (peak amplitudes) of the mode signals}} \quad (3.9)$$

The above measure is defined with respect to a given mode  $m$  signals for a particular internal wave realization at different times (0, 200, 400, 800, 1200 and 2400 seconds). The loss in averaging is defined as the ratio of the maximum of the time averaged signal to the mean of the maxima of the mode signals included in the average. Equation 3.9 was used to calculate the loss in averaging for the scattered time series and the unscattered time series. The estimated losses for the scattered and unscattered time series' were averaged across the multiple internal wave realizations. Figures 3.15 shows the mean loss in averaging the broadband mode signal at different times. The plots for broadband loss show that the unscattered parts and the scattering contributions suffer almost the same amount of loss with time averaging. Averaging does not result in an increase in SIR for the unscattered signal.

Based on the results for the broadband spectrum, the following can be said. Mode scattering up to 400 km, occurs in three different regimes. In the first regime, up to 50 km, the mean spectrum of the modes is described by the background spectrum. In the second regime between 50 km to 250 km, the scattering from other modes cause the mode spectrum to deviate from the background spectrum. In the third regime, for ranges beyond 250 km the coupling contributions dominate the mode spectrum and cause significant amounts of frequency selective fading.

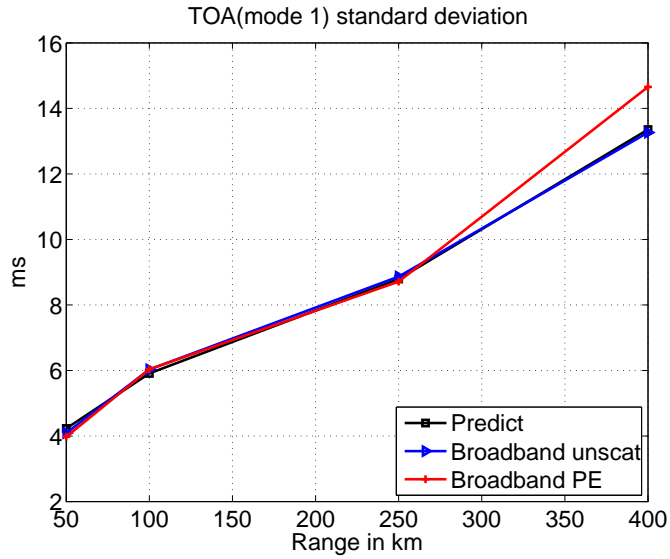


Figure 3.14: Standard Deviation (SD) of the TOA of mode 1 from PE simulations, Unscattered component simulations and numerical calculations. For ranges less than 250 km, the TOA SD of the unscattered mode matches the the SD of the PE simulated mode signal implying that the TOA variations of the unscattered component are responsible for the TOA variations of the total mode signal. At 400 km mode 1 is more scattered than at shorter ranges and thus has a higher TOA SD than the unscattered mode 1.

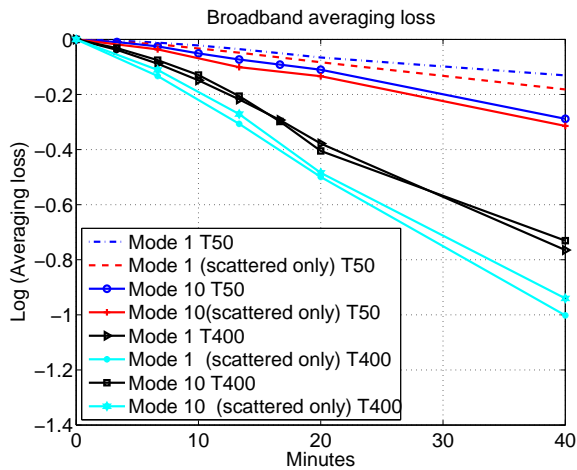


Figure 3.15: Averaging losses for modes 1 and 10 at 50 km and 400 km. Averaging across time, causes loss of up to 1 db for mode 1 and 10 at 400 km. Averaging in time does not provide SNR gain.

### 3.3 Summary

The simulation work in this chapter is a significant contribution to the literature on mode coupling. The unscattered component is a useful characterization to calculate the statistics of the mode signal and to gain insights into mode coupling at short ranges. The current literature on the effects of internal waves on modes has only concentrated on internal wave induced multipath and travel time wander. The analysis of the effect of internal waves on the source excitation spectrum is a new result presented in this chapter. The three different scattering regimes and the travel time statistics show that the modes have to propagate beyond 250 km for significant amount of scattering to occur.

## Chapter 4: LOAPEX mode signals

Previous chapters used simulations to describe the statistics of modes 1 to 10 up to ranges of 400 km. This chapter describes the mode signals received during LOAPEX at ranges of up to 500 km. The statistics derived from the simulations are compared with the statistics from LOAPEX. This chapter is organized as follows. Section 4.1 describes LOAPEX and gives the details relevant to processing the receptions. Section 4.2 describes how mode processing was implemented for LOAPEX. Section 4.3 shows the different SSPs measured during LOAPEX as a measure of the LOAPEX range variability. Section 4.4 discusses the mode signals received during LOAPEX and compares the statistics of the LOAPEX modes to simulations. Section 4.5 draws conclusions based on the results presented.

### 4.1 The Long Range Ocean Acoustic Propagation Experiment (LOAPEX)

LOAPEX was conducted in 2004 as part of a larger experiment conducted by the NPAL group. One of the objectives of LOAPEX was to study the evolution of the axial arrivals with respect to range. Figure 4.1 shows the geographical location of LOAPEX. The map shows the locations of the different transmission stations and the path of the LOAPEX signals. As mentioned before, LOAPEX had 7 transmission ranges at distances of 50 km to 3200 km along the same propagation path. At each range, a source suspended at a depth of 800 m from a ship made M-sequence transmissions to a mid-water spanning Vertical Line Array (VLA). The different transmission stations are labeled by T followed by the nominal transmission range. For example, the first station corresponding to the 50 km transmission range is named as ‘T50’, the second station ‘T250’ and so on. The VLA consisted of 40 hydrophones spanning depths of 350 m to 1750 m. The hydrophones spacing was 35 m.

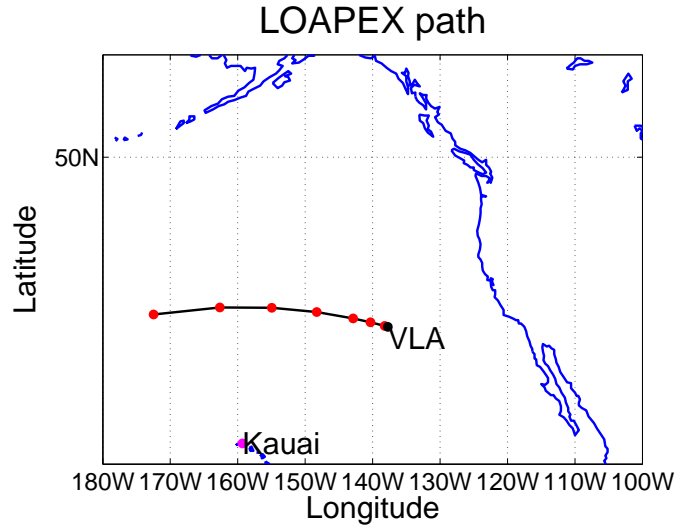


Figure 4.1: LOAPEX geographical location. The experiment consisted of a ship suspended source that made mid-water transmission from 800 m depth to an array from 7 different ranges of 50 km to 3200 km along the same propagation path.

The transmitted M-sequences were 1023 chips long and each chip Binary Phase Shift Key (BPSK) modulated 2 periods of a 75 Hz carrier. The transmissions lasted 20 minutes and the VLA sampled the received signals at 1200 Hz. The 20 minutes transmissions were recorded as 3 groups of 11 M-sequence periods. The different groups had start times of 0, 400 and 800s respectively. The x,y,z positions of the hydrophones in the array were tracked by a long baseline navigation system. The next section describes the mode processing for the T50, T250, and T500 stations.

## 4.2 Mode processing

The objective of the mode processor is to extract the time series for modes 1 to 10 from the pressure field recorded by the LOAPEX VLA. Figure 4.2 shows the diagram of a broadband mode processor. The sequence of steps in the mode processor are as follows. The reception across the array is matched filtered to obtain the pressure time series across each channel. The pulse compressed pressure field is then corrected for source and receiver delays and the processing offsets induced by the low pass demodulation filter and matched filter. The next

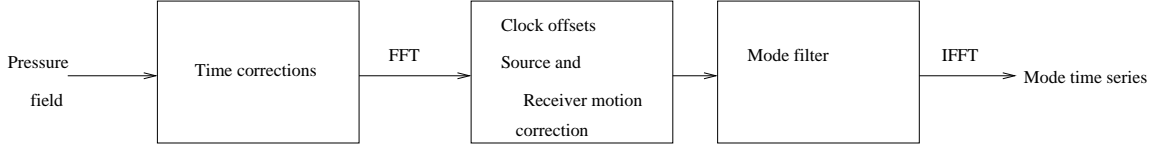


Figure 4.2: The different stages in broadband mode processing for LOAPEX

sequence sequence of steps happen in the frequency domain. The FFT algorithm is used to frequency transform the time compensated pressure field into separate bins. The phase errors due to receiver clock offsets and source and receiver motion is compensated in the frequency domain. Spatial filters are then applied for each of the frequencies of the pressure field to obtain narrowband mode signals ( $a_m(\omega)$ ). The narrowband mode signals are then inverse frequency transformed to obtain mode time series.

#### 4.2.1 Timing corrections for LOAPEX

The pressure field received across the array was complex demodulated, low pass filtered and matched filtered with the reference M-sequence waveforms. The output of the pulse compression is the pressure time series across the array. The LOAPEX experimental setup and the processing for LOAPEX signals had a number of delays to be accounted for. This section calls the uncompensated time as the nominal reception time. The nominal reception time should be offset to obtain the actual time of reception ( $t$ ) such that,

$$t = \underbrace{\hat{t}}_{\text{Nominal reception time}} + \underbrace{t_{src}}_{\text{Source delay}} + \underbrace{t_{Rx}}_{\text{Receiver filtering delay}} + \underbrace{t_{proc}}_{\text{M-sequence filtering delay}} \quad (4.1)$$

Equation 4.1 gives the actual time of reception as the sum of the nominal reception time and the source delay  $t_{src}$ , the receiver filtering delay  $t_{Rx}$  and the M-sequence processing delay  $t_{proc}$ . The receiver delays and the M-sequence filtering delays were estimated from cruise reports and via private communication with Peter Worcester<sup>1</sup> and Matthew Dzieciuch<sup>2</sup>. The

---

<sup>1</sup>Scripps Institution of Oceanography

<sup>2</sup>Scripps Institution of Oceanography

source delay was estimated from acoustic predictions for T50 and private communication with Rex Andrew<sup>3</sup>. This section describes the various delays and the amounts for each delay.

*Receiver and M-sequence processing delay:* At the front end of the receiver are the hydrophone and the high pass anti-strum filter. The total delay due to these two factors is equal to 2.1 ms. There were other factors contributing to further amounts of delay. The first A/D sample at the receiver occurs exactly 1 ms after the nominal reception time. The receiver clock had an offset that varied across receptions. The clock compensation  $t_{clock}$  was obtained from the clock correction files and included in the timing corrections. Each transmission consisted of a total of 12 multiple M-sequence periods that were sequentially transmitted one after the other. The recording at the receiver started midway through the first M-sequence period. Hence, each LOAPEX transmission effectively consisted of 11 M-sequence periods and the travel times recorded actually correspond to the second M-sequence period onwards. This causes an offset of one M-sequence period equal to 27.28 seconds. To compensate for that a time delay of -27.28 seconds is added to the time delay corrections. The total receiver delay is,

$$t_{Rx} = -2.1 \text{ ms} + 1 \text{ ms} - 27.28 \text{ s} + t_{clock} \quad (4.2)$$

The matched filtering operation uses a 9-pole low pass Bessel filter. Calculations using the phase response of the Bessel filter showed that the Bessel filter had a group delay of .0408 s. The processing time delay due to the match filtering is,

$$t_{proc} = -0.0408 \text{ s} \quad (4.3)$$

*Source delay:* Unfortunately, the delay for the LOAPEX source is not known exactly. The source delay is approximately between 13 ms to 27 ms [31]. An unaccounted source delay on the order of 13 ms to 27 ms would cause sound speed estimation errors of 0.5 m/s to

---

<sup>3</sup>Applied Physics Lab at the University of Washington

1 m/s, which are quite significant. In order to avoid sound speed estimation errors of that magnitude, the source delay had to be estimated and accounted for.

The source delay is assumed constant across time for each reception. Numerical simulations provide a travel time estimate for the LOAPEX signals across depth. Provided the other processing delays have been accounted for, the receptions at each station should be offset from the predictions by an amount equal to the source delay. As mentioned in the previous chapters, the axial arrivals have more multipath scattering that varies across depth and time. On the other hand, the early arriving ray arrivals are usually more stable across depth, making it easier to estimate their travel times. Thus the estimated travel times are used to infer the source delay as described below.

Numerical predictions of the ray travel times were obtained as follows. Environmental measurements made at a time close to the transmissions made during T50 were averaged to obtain a reference SSP  $c_0(z)$ . The reference SSP  $c_0(z)$  was used to predict the actual LOAPEX times of arrival for the ray arrivals. Note that for long range propagation it is important to take into account the spheroidal shape of the earth. This can be accomplished by measuring the propagation distances along circular arcs at each depth that are parallel to the earth's surface. Another way to implement this is by, scaling the sound speeds at the respective depths. This is called as the flat earth transformation [32]. The flat earth transformation for an SSP  $c(z)$  is given by,

$$\begin{aligned}\hat{z} &= z\left(1 + \epsilon + \frac{\epsilon^2}{3}\right) \\ \hat{c} &= c\left(1 + \epsilon + \epsilon^2\right)\end{aligned}\tag{4.4}$$

where  $\epsilon = \frac{z}{R_e}$ , where  $R_e$  is the earth's radius. The value of  $\epsilon$  increases with respect to depth which implies that flat earth transformation increases the sound speed at deeper depths. This intuitively makes sense because the rays traveling at deeper depths propagate across smaller arcs and thus travel faster, whereas rays at shallower depths travel across longer arcs and have a slower velocity across depth. The reference SSP  $c_0(z)$  was substituted in

equation 4.4 to account for the earth's curvature. The modeshapes of the modified SSP were substituted in Equation 2.1 to simulate the acoustic pressure field at T50. The LOAPEX signals were initially time compensated with the receiver ( $t_{Rx}$ ) and processing delays ( $t_{proc}$ ) described in the last section. Figure 4.3 shows the comparison between the mean LOAPEX peak arrivals at each depth and the predictions made using the sound speed profile measured at the array. The time offset between the mean LOAPEX peaks and the predictions for the first ray arrival has a mean of -17.2 ms and a variance of 2 ms. As explained below, it is plausible that the 2 ms variance can be explained by internal wave variability. The sound speed perturbations for a Garrett-Munk strength of 0.5 have a mean standard deviation of 0.1 m/s across the whole water column. The rays travel through the whole water column, thus they effectively propagate across the mean sound speed perturbation across depth. For a sound speed of approximately 1500 m/s, a sound speed perturbation of 0.1 m/s causes a 2 ms travel time perturbation, which correlates well with the 2 ms standard deviation of the travel time perturbation for the LOAPEX ray arrivals. Discounting the 2 ms travel time perturbations due to internal waves, the travel time offset induced by the source is equal to -17.2 ms. Figure 4.4 shows the LOAPEX signals that were also compensated with a -17.2 ms source delay. The source delay is constant for the different ray arrivals hence the source delay compensation is also enough to align the time arrivals of the later ray arrival that arrives between 30.1 s and 30.2 s. This implies that the source delay  $t_{src}$  is given by,

$$t_{src} = -0.0172 \text{ s} \quad (4.5)$$

Substituting the time delays in equations 4.2, 4.3 and 4.5 in equation 4.1, the system of time delays is,

$$t = \hat{t} - 0.0021 \text{ s} + 0.001 \text{ s} - 27.28 \text{ s} + t_{clock} - 0.408 \text{ s} - 0.0172 \text{ s} \quad (4.6)$$

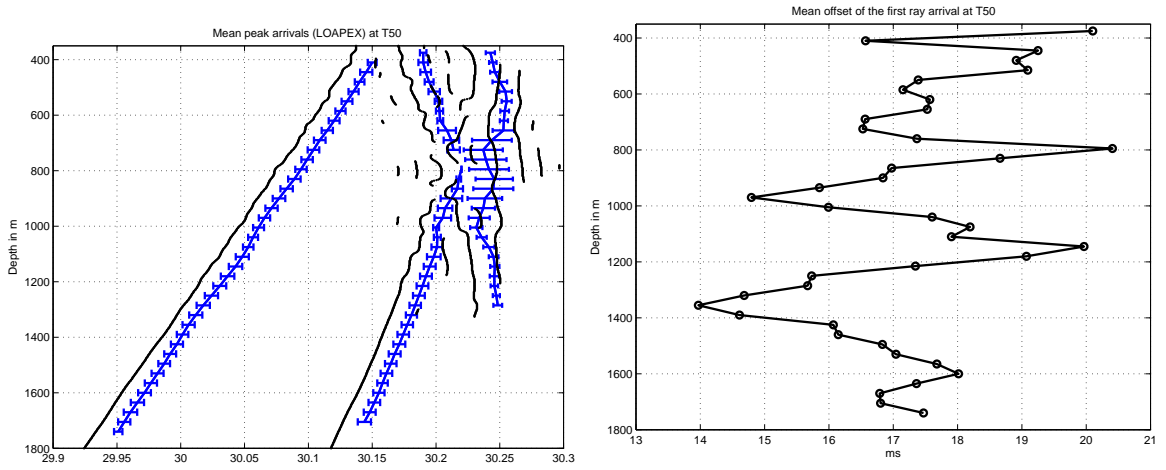


Figure 4.3: LOAPEX arrivals vs predictions at T50. The left subplot shows the peak arrivals of LOAPEX at each depth. The right subplot shows the difference between the time of arrival of the peak at each depth and predicted times of arrival of the peak at each depth. The right subplot shows the difference between the peak arrival for LOAPEX and the predictions across depth. The travel time offset has a mean of 17.2 ms.

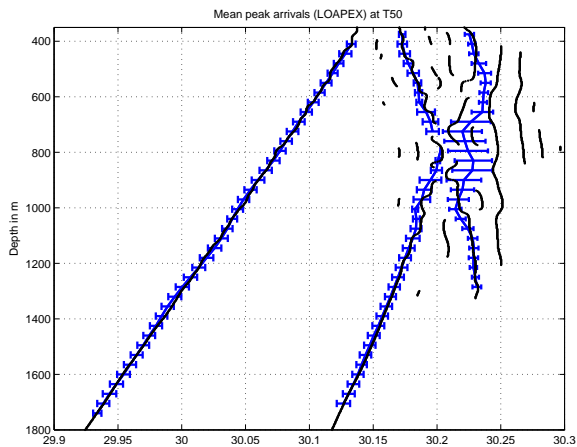


Figure 4.4: The T50 LOAPEX signals compensated only for receiver delays, processing delays and a source delay of 17.2 ms.

### 4.2.2 Mode filtering

The spatial filter is the heart of the mode processor. This section describes the spatial filters for LOAPEX and is organized into two parts. The first part defines the spatial matched filter for modes. The second part provides specific details about how the spatial filter was designed for LOAPEX.

*Spatial filters for modes:* Extracting the mode signal from the pressure field is a problem in spatial filtering. Ferris [33] and Ingenito [34] used a matched filter to extract the mode signals received in shallow water. A matched filter for the spatial processor is given by

$$\mathbf{W}_{\text{mf}} = \Psi_{\mathbf{n}} \quad (4.7)$$

$\Psi_{\mathbf{n}}$  is matrix of modeshapes of modes 1 to  $N$  such that it contains the modeshapes (of the type plotted in Figure 2.1) sampled at the array. The working of the matched filter can be explained as follows. Given a narrowband pressure field  $\mathbf{P}$  measured across depth  $z$ , such that,

$$\mathbf{P} = \sum_m \Psi_m a_m \quad (4.8)$$

$$\mathbf{P} = \Psi \mathbf{a} \quad (4.9)$$

$$\Psi^H \Psi \approx \mathbf{I} \quad (4.10)$$

By equations 4.8 to 4.10,

$$\Psi^H \mathbf{P} = \begin{bmatrix} a_1 \\ a_2 \\ \vdots \\ a_N \end{bmatrix} \quad (4.11)$$

For more information on the matched mode filter refer Wage *et al.* [26]. Note that according to Equation 4.10, the matched filter relies on the mutual orthogonality of the sampled modeshapes to separate them. The rest of this section, discusses how the matched filter was constructed for LOAPEX and the effect of the array resolution on the MF performance.

*Mode filters for LOAPEX:* The modeshapes depend on the SSP, which may vary significantly across time. Mismatch in modeshapes causes loss in array gain and additional cross mode coupling. During LOAPEX, continuous environmental measurements were made by Seabird sensors clamped to the VLA cable. The Seabird SBE 39 microtemps measured the temperature and pressure and the SBE 37 microcats measured temperature, pressure and salinity. These continuous environmental measurements provide a means to estimate the SSP at a time close to the LOAPEX transmission. The SSP was estimated from the environmental measurements made during the day the T50 transmissions were made and averaged over a day. The LOAPEX SSP was then substituted in the depth dependent Equation 2.2 to estimate the LOAPEX modeshapes. The transmissions at T50, T250 and T500 occurred between year days 259 to 263. The daily average of the SSP suppresses the internal wave variability. The averaged SSP is fairly constant across several days. The estimated modeshapes from the T50 Seabird profile are hence similar to the modeshapes during T250 and T500. The T50 modeshapes were hence used to construct the mode filters for T250 and T500 also.

Figure 4.5 shows MF beam pattern for the profile measured at the LOAPEX array. The MF is able to separate modes 1 to 10 with no cross talk from other modes. The cross talk

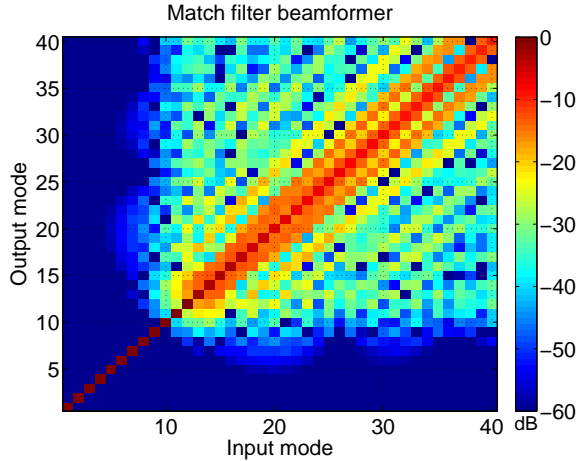


Figure 4.5: The MF beamformer beampattern for modes 1 to 40 for the measured profile. The beampattern is defined as  $20 \log_{10}(\mathbf{W}^H \mathbf{\Psi})$  where  $\mathbf{W}$  is the MF beamformer defined in equation 4.7 and  $\mathbf{\Psi}$  is the matrix of modeshapes sampled at the array. The MF beamformer resolves modes 1 to 10 with minimal crosstalk.

from modes higher than 10 is in the order of -30 dB, which is negligible. Note that at T50 and beyond, modes higher than 40 arrive at an earlier time and are temporally separable from modes 1 to 10. Modes greater than 40 are not plotted in the beampattern. This thesis aims to analyze modes 1 to 10. The MF filter beamformer shows that matched filter beamformer is able to separate modes 1 to 10 with minimal crosstalk.

The modeshapes in Equation 4.7 vary as a function of frequency. Wage showed that when the MF filter does not use the frequency dependent modeshapes, the performance of the MF filter suffers from loss in white noise gain and additional cross talk [26]. In order to accommodate the change in modeshapes with frequency, the MF beamformer must vary as a function of frequency. The modeshapes across frequency were estimated by solving Equation 2.2 for different frequencies. The frequency dependent modeshapes were then used to construct the mode filter as a function of frequency. Mode processing is sensitive to array motion and source motion. The next section discusses array and source motion compensation for LOAPEX signals.

### 4.2.3 Array motion correction

*Compensation for array motion:* The narrowband output  $a_m$  of the spatial filter  $\mathbf{W}_m$  for mode  $m$  with uncorrected array motion is given by,

$$\hat{a}_m(\omega) = \sum_n w_m^H(z_n) \Psi_m(z_n) e^{ik_m r_n} \quad (4.12)$$

where  $r_n$  is the displacement of the  $n^{\text{th}}$  hydrophone. The uncompensated array motion in Equation 4.12 causes phase errors across the array. Uncompensated phase leads to two problems. First, phase error across the entire array leads to loss of spatial gain for the narrowband mode signal  $\hat{a}_m(\omega)$ . Second, phase errors cause travel time errors in the broadband time series  $\hat{a}_m(t)$ . The array motion must hence be estimated and accounted for.

Section 4.1 noted that the x,y and z locations of the array elements were estimated by a baseline navigation system [35,36]. Given the location of the array, it is a straightforward problem to calculate the radial displacements from the navigation data and use it in equation 4.12 to compensate for array motion. Unfortunately the navigation data was missing for the upper half of the VLA at stations T50, T250 and T500. Estimation of the navigation data for one half of the VLA from the other half is an extrapolation problem across depth. The extrapolation method suitable for this problem should take into account the general shape of the array. This thesis uses a basis defined by the Empirical Orthogonal Functions (EOFs) to describe the shape of the array. Oliveira estimated missing image data using an approach based on the principal components of the image data [37]. Chandrayadula using a similar approach estimated the missing navigation data using EOFs [38]. The rest of this section describes the relevant details of this method.

The extrapolation method estimates the missing navigation data using a set of EOFs derived from the second order statistics of the navigation data. The approach assumes that these statistics can be estimated during times when complete navigation information is available. The EOFs are the eigenvectors of the correlation matrix, which form a complete

orthonormal basis, thus the navigation data can be written as a weighted sum of the EOFs. When partial navigation information is available, *e.g.*, for half the array, the available data can be used to find a least squares estimate of the weights. The rest of this section describes the details of the approach and shows how the EOF coefficients are solutions to an optimization problem.

The observation vector consists of the navigation data for the array arranged as a column such that

$$\mathbf{d} = \begin{bmatrix} \mathbf{x} \\ \dots \\ \mathbf{y} \\ \dots \\ \mathbf{z} \end{bmatrix}. \quad (4.13)$$

The vector  $\mathbf{d}$  contains the navigation data in the  $\mathbf{x}, \mathbf{y}$  and  $\mathbf{z}$  directions. The observation vector  $\mathbf{d}$  is spanned a matrix of orthogonal column vectors  $\mathbf{U}$  where,

$$\mathbf{d} = \mathbf{U}\mathbf{c}. \quad (4.14)$$

The coefficient vector  $\mathbf{c}$  in Equation 4.14 is modeled as random and unknown. The columns of  $(\mathbf{U})$  constitute a complete orthonormal basis set and are the eigenvectors of the correlation matrix  $\mathbf{R}_{\mathbf{d}\mathbf{d}}$ . As mentioned earlier, it is assumed that for this problem, the eigenvectors  $\hat{\mathbf{U}}$  can be estimated from the data, thus are referred to as EOFs. Consider a matrix  $\mathbf{L}$  which contains ones along the main diagonal except where the data is missing when the elements are set to zero. For instance the matrix  $\mathbf{L}$  for the missing data in LOAPEX where navigation data for half the array is missing is

$$\text{diag}(\mathbf{L}) = \begin{bmatrix} \mathbf{0s} \text{ (20x1 vector)} \\ \mathbf{1s} \text{ (20x1 vector)} \\ \mathbf{0s} \text{ (20x1 vector)} \\ \mathbf{1s} \text{ (20x1 vector)} \\ \mathbf{0s} \text{ (20x1 vector)} \\ \mathbf{1s} \text{ (20x1 vector)} \end{bmatrix}. \quad (4.15)$$

Multiplying the previous equation by matrix  $\mathbf{L}$  to accommodate for the missing data, Equation 4.14 now becomes

$$\mathbf{Ld} = \mathbf{LUc} \quad (4.16)$$

The objective is to estimate the coefficient vector  $\mathbf{c}$  and estimate the navigation data  $\hat{\mathbf{d}}$  by  $\mathbf{d} = \mathbf{Uc}$ . The estimate  $\hat{\mathbf{c}}$  is obtained by minimizing the following function,

$$J = \underset{\mathbf{c}}{\text{Min}} \|\mathbf{L}(\mathbf{d} - \mathbf{U}\hat{\mathbf{c}})\|^2. \quad (4.17)$$

The above function  $J$  is the square of the norm of the distance between the measured navigation data ( $\mathbf{d}$ ) and the reconstructed navigation data ( $\mathbf{d} = \mathbf{Uc}$ ). Minimizing  $J$  is a problem in LS filtering [39]. The LS estimate  $\hat{\mathbf{c}}$  and the estimate  $\hat{\mathbf{d}}$  that contains estimates for the missing data are given by,

$$\hat{\mathbf{c}} = (\mathbf{U}^T \mathbf{L} \mathbf{U})^{-1} \mathbf{U}^T \mathbf{L} \mathbf{d}, \quad (4.18)$$

$$\hat{\mathbf{d}} = \mathbf{U} (\mathbf{U}^T \mathbf{L} \mathbf{U})^{-1} \mathbf{U}^T \mathbf{L} \mathbf{d}. \quad (4.19)$$

During the yearlong deployment of NPAL/LOAPEX, the VLA recorded navigation data

once per hour. Unlike LOAPEX, there were other times of the experiment when navigation data was available for the entire array. It is reasonable to assume that the array dynamics are the same over the entire duration of the experiment. The navigation data recorded during the overall SPICE04 experiment can be used to estimate the EOFs. The EOF estimator was calculated using the navigation samples recorded between yeardays 160 and 240, which correspond to the times before LOAPEX. The sample correlation matrix  $\mathbf{R}_{\mathbf{d}\mathbf{d}}$  was constructed from the measured navigation data. The eigenvectors of  $\mathbf{R}_{\mathbf{d}\mathbf{d}}$  were calculated to obtain the EOFs  $\mathbf{U}$  of the data. Figure 4.6 shows a plot of the 10 most significant eigenvalues  $\lambda$  of the sample correlation matrix. The first 3 eigenvalues significantly differ in amplitude from the rest of the eigenvalues. Figure 4.6 also shows a plot of the measure  $\mu_\lambda$  defined below.

$$\mu_\lambda = 100 \frac{\sum_{i=1}^k \lambda_i}{\sum_{i=1}^N \lambda_i}, k \leq N, N = 120. \quad (4.20)$$

The measure  $\mu_\lambda$  is equivalent to the percentage of energy contained in the subspace  $\mathbf{U}$  for different number of eigenvectors. Figure 4.6 shows that the first 3 eigenvectors contain more than 99.99% of the total energy in the navigation data. Figure 4.7 shows a plot of the corresponding 3 EOFs. The first eigenvector mainly describes the depths ( $\mathbf{z}$ ), while the other two EOFs roughly describe the shape of the array in the  $\mathbf{x}$  and  $\mathbf{y}$  directions. A reduced dimension EOF matrix  $\hat{\mathbf{U}}$  consisting of only the three EOFs shown in Figure 4.7 was used to construct the EOF based LS estimator in Equation 4.18. Figure 4.8 shows a sample reconstruction of the navigation data for yearday 402. The EOF estimator estimated the top 20 hydrophones of the array from the other half. The figure shows the magnitude of the radial displacement of the array and the EOF reconstructed array, both in the direction of arrival of the signal. The reconstructed array shape closely follows the actual array shape.

The error statistics of the EOF-based LS filter were evaluated as follows. Other than times before LOAPEX, SPICE04 also had good navigation data for both the halves of the array for a contiguous time period between yeardays 400 to 480. Note that these yeardays

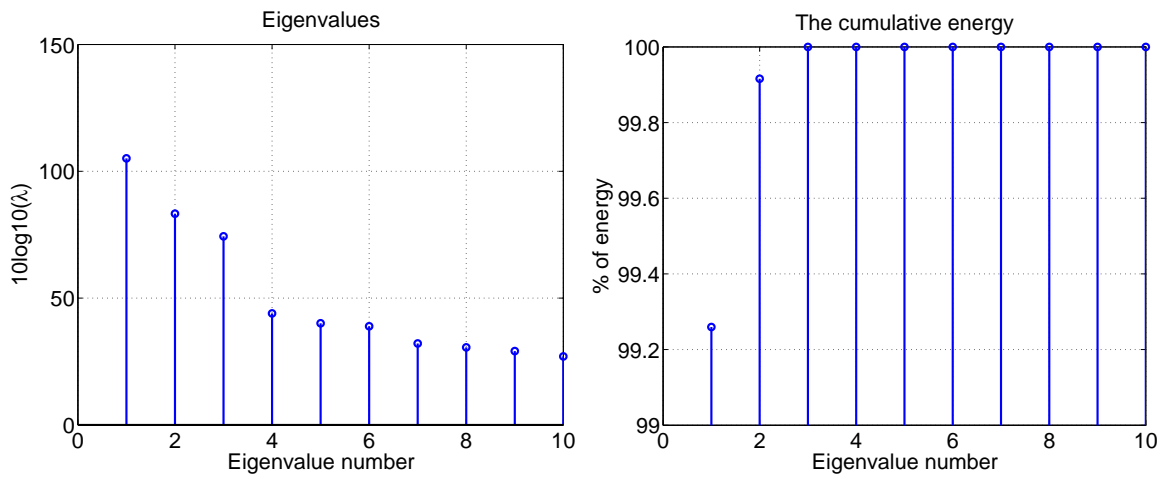


Figure 4.6: The eigenvalues ( $\lambda$ ) of the correlation matrix of the navigation data. The top subplot shows that the first 3 eigenvalues are at least 25 dB higher in amplitude than the rest of the eigenvalues. The bottom subplot shows a plot of the percentage of the cumulative energy contained in the eigenvalues. The first 3 eigenvalues make up more than 99.99 % of the energy in the navigation data.

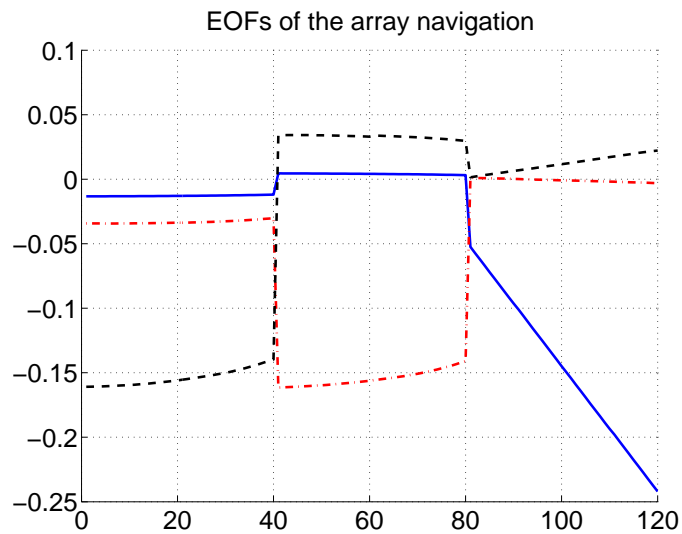


Figure 4.7: EOFs 1 to 3 for the navigation data from yeardays 160 to 240. The 3 EOFs roughly describe the shape of the array in the X, Y and Z directions.

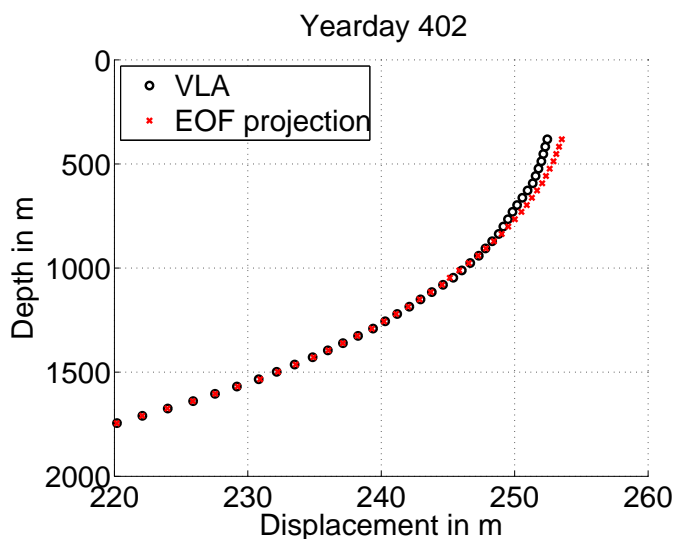


Figure 4.8: EOF sample reconstruction for yearday 402. The black ( $\circ$ ) curve shows the true position of the array and the red ( $\times$ ) curve shows the reconstructed array.

correspond to times after LOAPEX. The EOFs shown in Figure 4.7 were used to estimate the navigation data of the upper half from the lower half. The estimated navigation data was then compared with the actual navigation data. Figure 4.9 shows a plot of the mean error in the displacement of the array as a function of depth. The estimation error decreases with depth. The array moves less as depth increases since it is anchored at the bottom. The shallowest hydrophone is off by a distance of approximately 3 m. The RMSE averaged across the entire array was approximately 1.5 m.

*Sensitivity analysis of mooring estimation errors:* The sound speed of the underwater channel is typically on the order of 1500 m/s, hence a mooring estimation error on the order of 1.5 m results in timing errors of approximately 1 ms. A simulation for the MF beamformer for modes 1 to 40 was performed for different values of linear array tilt. Figure 4.10 shows the spatial gain for different modes as a function of tilt. The tilt is measured with reference to the lowest hydrophone. The left plot shows that modes 10 and 40 are more sensitive to tilt than mode 1. The increase in sensitivity with mode number is because, the higher modes contain more variations across depth. A tilt of more than 10 m causes a loss of more than 3 dB for modes 10 and 40. The right plot shows the loss in gain for a tilt of 3 m,

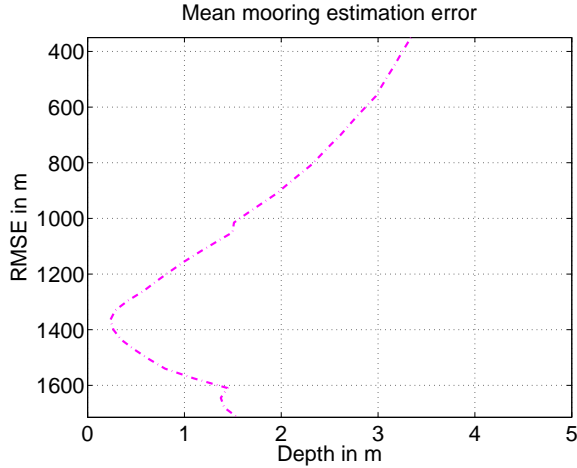


Figure 4.9: The Root Mean Square Error (RMSE) performance of the EOF based reconstruction for yeardays 400 to 480 as a function of depth. The 3 EOFs shown in figure 4.7 were used in the EOF estimator. The RMSE decreases as a function of depth. The mean RMSE is on the order of 1.5 m.

which is the EOF mooring estimation error. The modes suffer a loss of less than 0.2 dB.

The conclusions about the EOF estimation for array navigation data are as follows. The reconstruction result demonstrates that the EOF estimator works well. The sensitivity analysis showed that the estimation errors in the EOF estimation scheme cause an average timing error of 1 ms and a loss of less than 0.2 dB in the spatial gain of the MF beamformer. This shows that the presented estimation scheme works well to recover the missing navigation data with only a minor degradation for mode processing.

#### 4.2.4 Source motion compensation

In addition to array motion the LOAPEX ship suspended source moved in proportion to the ships motion. The source motion induced timing error and phase errors have to be compensated. A GPS system tracked the  $x$ ,  $y$ , and  $z$  positions of the ship. The source positions were inferred from the ship’s motion via cable dynamics model and a tidal model [40], [41]. The radial displacement  $r_s$  was calculated from the estimated source position. The figures below shows the amount of source motion measured at T50 and T250. The plots show that the ship moves up to a maximum of approximately 12 m.

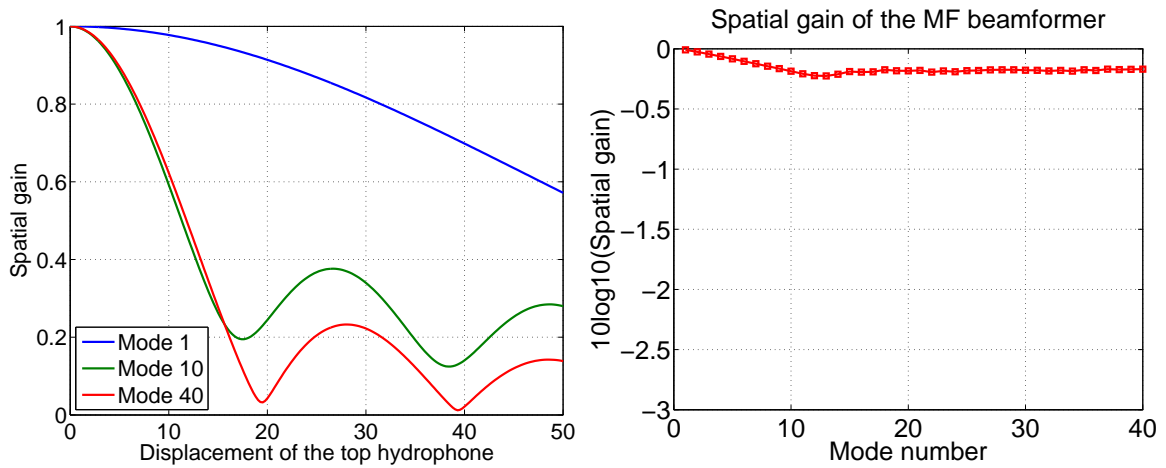


Figure 4.10: Spatial gain for different modes as a function of tilt. The tilt is measured with reference to the lowest hydrophone. The left plot shows that modes 10 and 40 are more sensitive to tilt than mode 1. A tilt of more than 10 m causes a loss of more than 3 dB for modes 10 and 40. The right plot shows the loss in gain for a tilt of 3 m, which is the EOF mooring estimation error. The modes do not suffer more than 0.3 d dB loss.

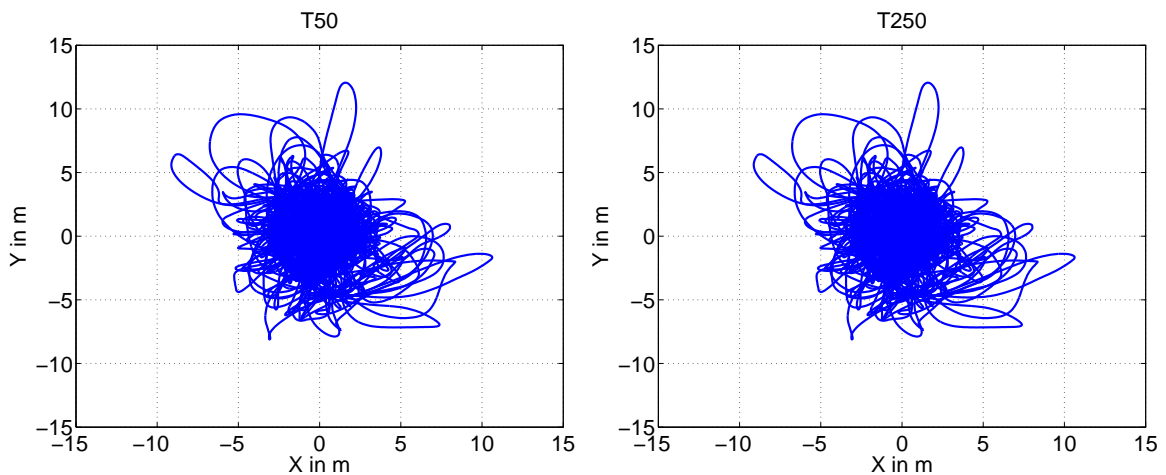


Figure 4.11: Source motion at T50 and T250. The source moves on the order of 10 m to 15 m.

The phase shift due to the source and the receiver motion is incorporated into the narrowband beamformer as

$$\widehat{\mathbf{w}}_{\mathbf{m}} = \begin{bmatrix} w_m(z_1)e^{-jk_m(r_1+r_s)} \\ w_m(z_2)e^{-jk_m(r_2+r_s)} \\ \vdots \\ w_m(z_n)e^{-jk_m(r_n+r_s)} \end{bmatrix} \quad (4.21)$$

The MF beamformer ( $\mathbf{w}_{\mathbf{m}}$ ) for each mode, given by equation 4.7 and the estimated source ( $r_s$ ) and receiver motion ( $r_k$  for  $k = 1, 2, \dots, N$ ) was substituted in Equation 4.21 to estimate the narrowband mode amplitudes. The narrowband mode signals were then inverse frequency transformed to obtain the mode time series  $a_m(t)$  for each mode. The next section discusses the mode time series at T50, T250 and T500.

### 4.3 Range variability in LOAPEX

Before analyzing the LOAPEX receptions it is helpful to consider the background sound speed variability across the LOAPEX path. Figure 4.12 compares the SSPs measured at the stations T50, T250, T500 with the sound speed profiles measured at the array during the transmissions on yearday 259. The signals propagating in LOAPEX should experience considerable changes in the background environment. The travel times and the characteristics of the mode signals are affected by internal waves and changes in the background environment. Given that the SSP varies with range, we expect two things. First, the internal waves should induce variance in the mode travel times. Second, the mean mode travel time at each range should be a function of the average SSP across the propagation path.

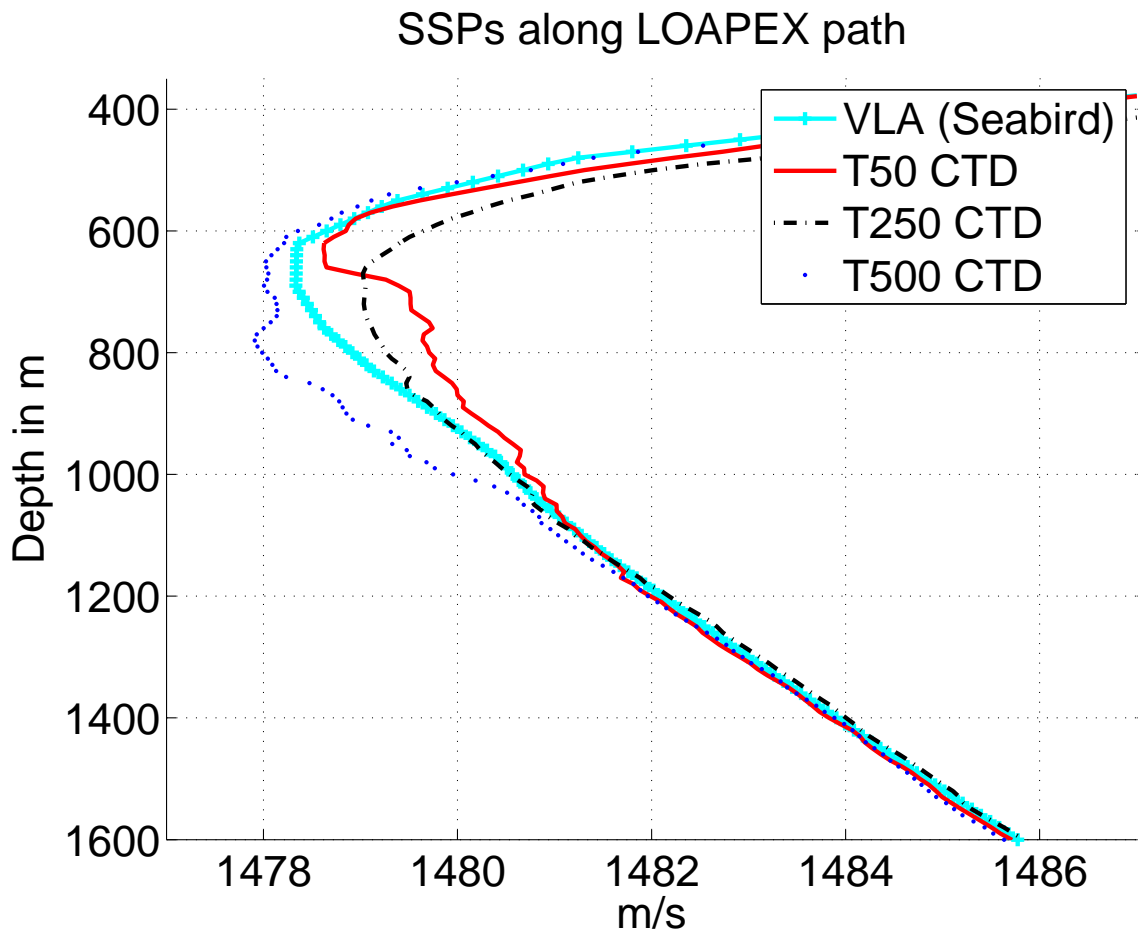


Figure 4.12: Sound speed profiles measured along the LOAPEX path. The SSP (Seabird) at the VLA (cyan -+), the T50 CTD (red '.'), the T250 CTD (black '-.'), the T500 CTD (blue '·') SSPs vary across range. Although the T50 CTD profile and the SSP at the VLA were measured only 50 km apart, the two profiles are much different from each other.

## 4.4 LOAPEX mode signals

This section discusses the broadband and narrowband statistics of the LOAPEX modes that were processed using the filtering methods described in section 4.2. Similar to the previous chapter, instead of discussing the statistics of the different modes, this section concentrates on the statistics for modes 1 and 10. The statistics for the other modes lie in between. This section is organized as follows. Section 4.4.1 discusses the LOAPEX mode time series. The time series for modes 1 and 10 at T50, T250 and T500 are shown to discuss the variability across time and range. The standard deviation of the travel times of the peaks of modes 1 and 10 are estimated and compared with the predictions from the simulations in Chapter 3. Section 4.4.2 discusses the modes in frequency domain. Similar to the discussion on time domain statistics, the range and time variability of the modes 1 and 10 spectrum are emphasized. Section 4.4.3 discusses the narrowband time coherence at 75 Hz. While the last chapter relied on 50 independent internal wave simulations the LOAPEX signals at each station are much less in number. The LOAPEX transmissions are spaced in time at an hour or less apart. Some time scales of internal waves last for more than an hour [13, 14]. The LOAPEX modes hence sample less internal wave variability. Thus the number of independent LOAPEX transmissions is much less in comparison to the simulations in the last chapter.

### 4.4.1 Time domain plots for LOAPEX

All the T50 transmissions took place on yearday 259. There were ten 20 minute transmissions each beginning at the top of the hour between hours 6 and 15. As mentioned before, each transmission consisted of 33 M-sequence periods, split into 3 parts. Figure 4.13 shows modes 1 and 10 for only the first M-sequence period for each of the transmissions. Modes 1 and 10 are dispersed in time with mode 1 arriving before mode 10. The arrival structure for modes 1 and 10 differ from each other. Similar to the simulation examples in the last chapter depicted in Figure 3.11, mode 1 consists of a single peak whereas mode 10 has a multi-peaked arrival. The mode amplitudes vary from one transmission to the other.

Moving on to T250 in Figure 4.14, there were 8 transmissions that occurred between yeardays 260 to 261 from hour 21 to hour 6. Compared to T50, the amount of inter-modal dispersion and the chromatic dispersion is greater. Mode 1 contains small arrivals that precede the main arrival. For some receptions mode 10 contains more than two peaks. The T250 mode time series again match the simulation examples in Figure 3.11. At T500, there were 14 transmissions that occurred between yeardays 262-263. Figure 4.15 shows the LOAPEX modes 1 and 10. The mode arrivals at T500 completely differ from the mode arrivals at T50 and T250. Both, modes 1 and 10 contain multiple peaks. The frequency spectrum plots for the mode simulations in Figure 3.12 predicted multipath induced frequency fading for modes 1 and 10. The frequency domain comparison between the T500 modes and the simulations is done later in this section.

The LOAPEX travel time estimates for the LOAPEX modes were estimated by calculating the time associated with the peak arrival of the LOAPEX modes. This thesis calls this procedure as 'peak picking'. Peak picking was implemented for the first M-sequence period for the three parts of each transmission, thus giving three travel time estimates per transmission. At T50 this provided  $10 \times 3 = 30$  estimates. Figure 4.16 shows the mean and variance of the travel time estimates and compares it with the travel times predicted by the SSP measured at the array and the CTD SSP measured at T50. The travel time estimates for all the modes are closer to the Seabird predictions than the CTD. Modes such as 6, 7, 9 and 10, the LOAPEX peaks have a greater time variance than the other modes. Similar to the T50 mode 10, modes 3, 6, 7 and 9 also had a two-peaked arrival, hence, the result for peak picking oscillates between the two peaks, which results in a higher variance in peak picking for these modes. The plot for the sound speed variability in Figure 4.12 showed a significant difference in sound speeds between stations T50 and the array. The, mean time of the LOAPEX modes is closer to the estimates produced by the SSP measured at the array. This implies that the T50 modes propagated in an environment more similar to environment at the array.

At T250 a total of 8 transmissions were made that were spaced one hour apart between

yeardays 260-261. Figure 4.17 shows that the travel time estimates of modes 1 to 10 lie in between the T50 and T250 predictions. At T500, 14 transmissions were made between yeardays 262-263. Figure 4.18 shows that the travel time estimates of the different modes lie midway among the predictions made using the different profiles. On a mode by mode basis, mode 1 shows a bias towards an earlier time of arrival. This is because, mode 1 receives receives all its coupling energy from higher modes which propagate with a higher velocity. The travel time variances for the different modes show that modes 1, 2 and 3 have a much less variance than the other higher modes. The less travel time variance implies that modes 1, 2 and 3 are less sensitive to internal wave induced scattering at T500.

Figure 4.19 shows the travel time variance for the different modes for the LOAPEX modes at T50, T250 and T500. As mentioned before, the number of transmissions at each station for LOAPEX are much less in terms of environmental variability. The travel time standard deviation for the LOAPEX modes hence differ from the simulation predictions.

#### 4.4.2 Spectrum plots for LOAPEX

*T50 spectrum:* Figure 3.13 in Section 3.2.3 compared the mean mode spectrum at ranges of 50 km, 250 km and 400 km from simulations. The two conclusions from the spectrum plots were as follows. First, the mode spectrum at 50 km and 100 km was mainly a function of the mode spectrum at the source. Second, the mode spectrum for ranges greater than 250 km showed fading due to mode coupling. This section follows an analysis similar to Section 3.2.3 and compares the LOAPEX mode spectrum at different ranges. Figure 4.20 shows the mode 10 spectrum at the source that was estimated using the modeshapes of the CTD profile in Figure 4.12. The mode 10 spectrum at the source and the array significantly differ from each other. The Seabird spectrum at the array contains a null around 75 Hz, whereas the CTD spectrum contains a null at 90 Hz. The T50 profile consisted of a single measurements made just before the T50 transmissions began. The previous chapters noted that point measurements without any averaging in time contain internal wave noise. To appreciate the variability in mode 10 spectrum across time for the LOAPEX environment

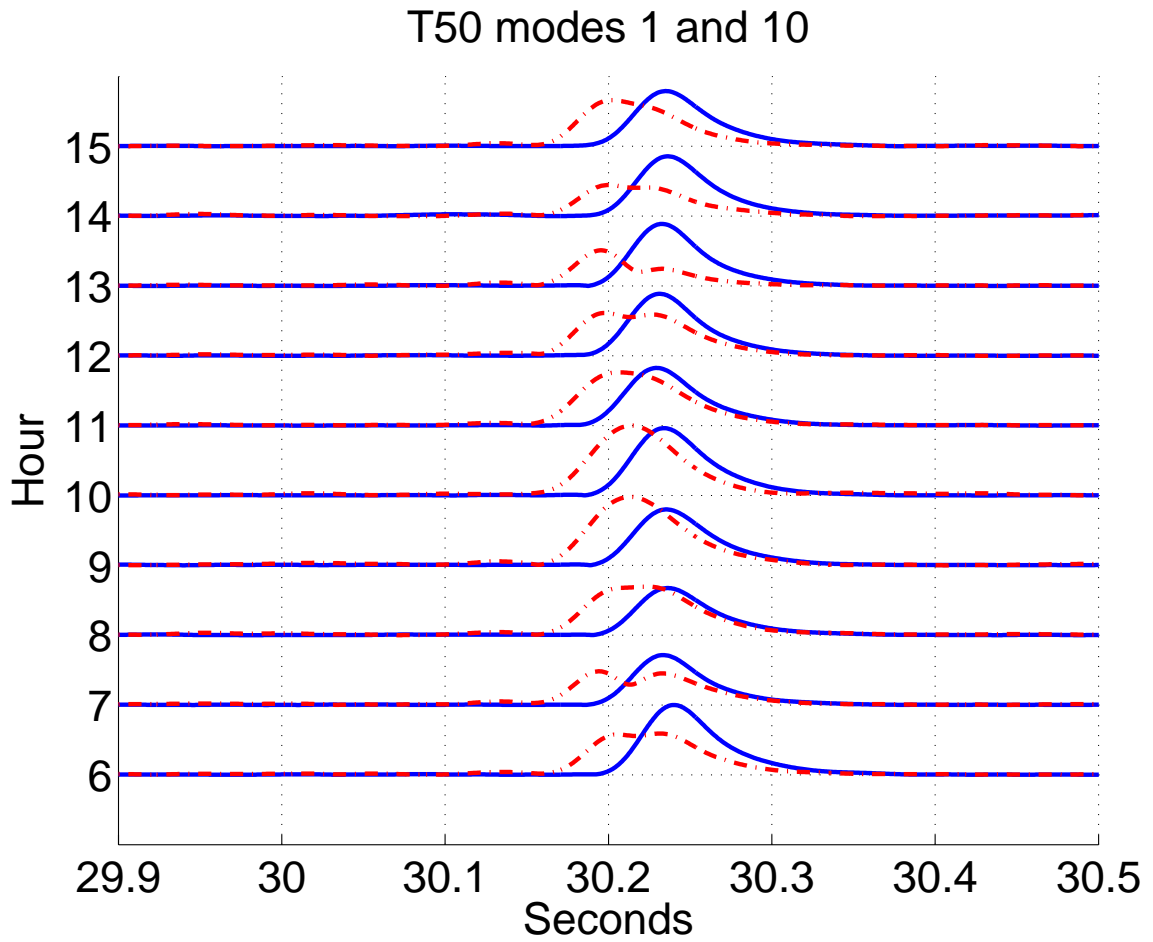


Figure 4.13: Modes 1 (blue) and 10 (red -.) at T50. There were 10 transmissions on yearday 259 between hours 6 and 15. Modes 1 and 10 are dispersed over time. The arrival structure and the time of arrival for modes 1 and 10 changes across time. The arrival structure for mode 1 consists of a single peaked arrival and mode 10 for some receptions consists of a double peaked arrival.

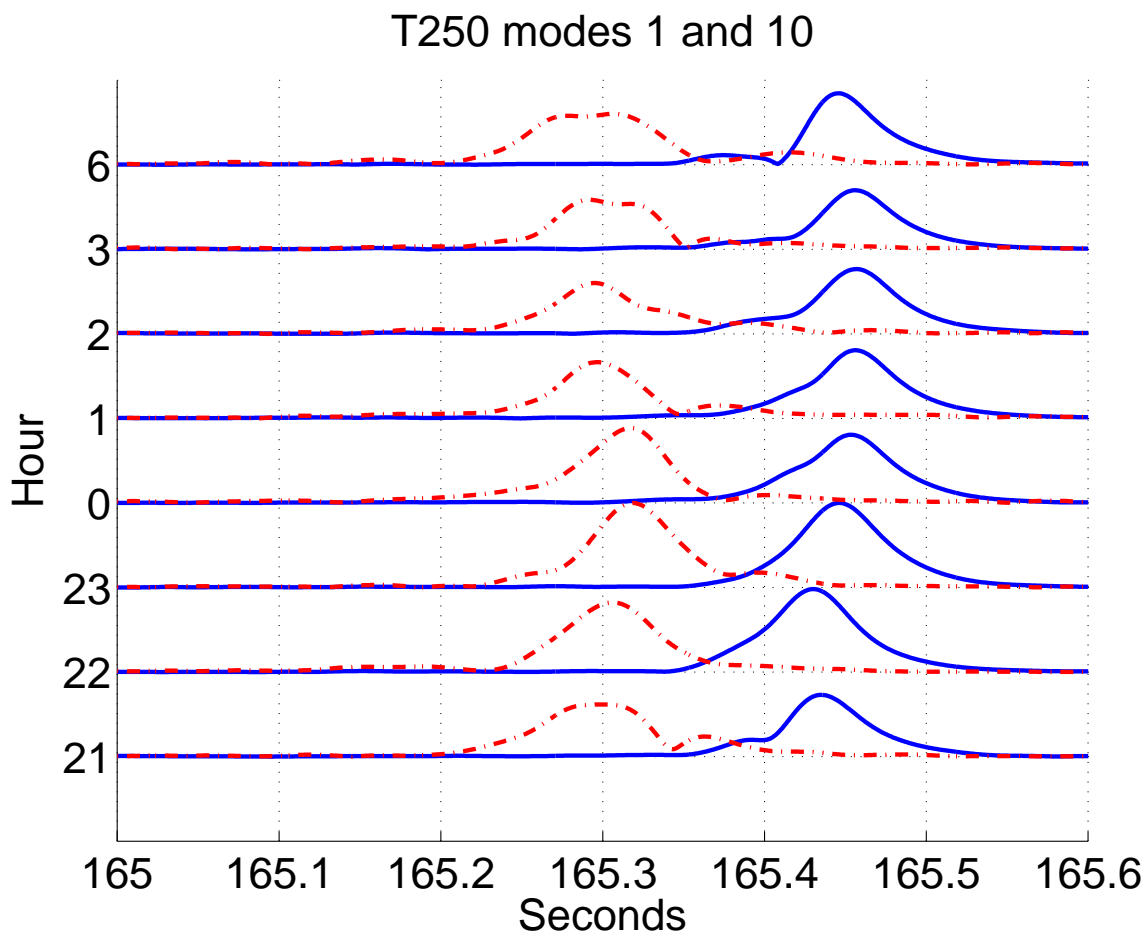


Figure 4.14: Modes 1 (blue) and 10 (red -.) at T250. There were 8 transmissions that occurred between yeardays 260 to 261 from hour 21 to hour 6. Compared to T50, the amount of inter-modal dispersion and the chromatic dispersion is greater. Mode 1 contains small arrivals that precede the main arrival. Mode 10 for some receptions contains more than two peaks.

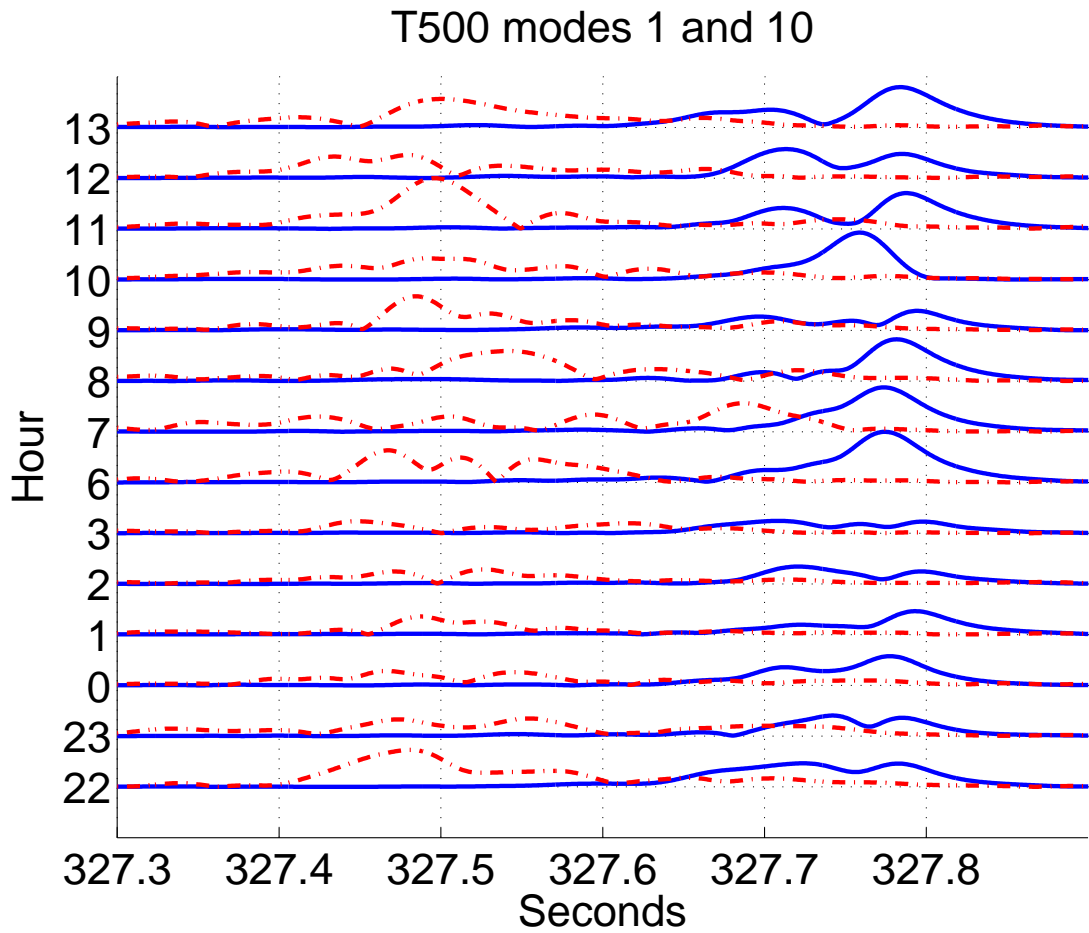


Figure 4.15: Modes 1 (blue) and 10 (red -.) at T500. There were 14 transmissions that occurred between yeardays 262-263 in an intermittent manner. Both, modes 1 and 10 contain multiple peaks/arrivals. This implies that the amount of scattering is significantly higher than at T250. Also note that the amount of variability of the mode arrivals across time is higher than the previous ranges (Figures 4.13 and 4.14).

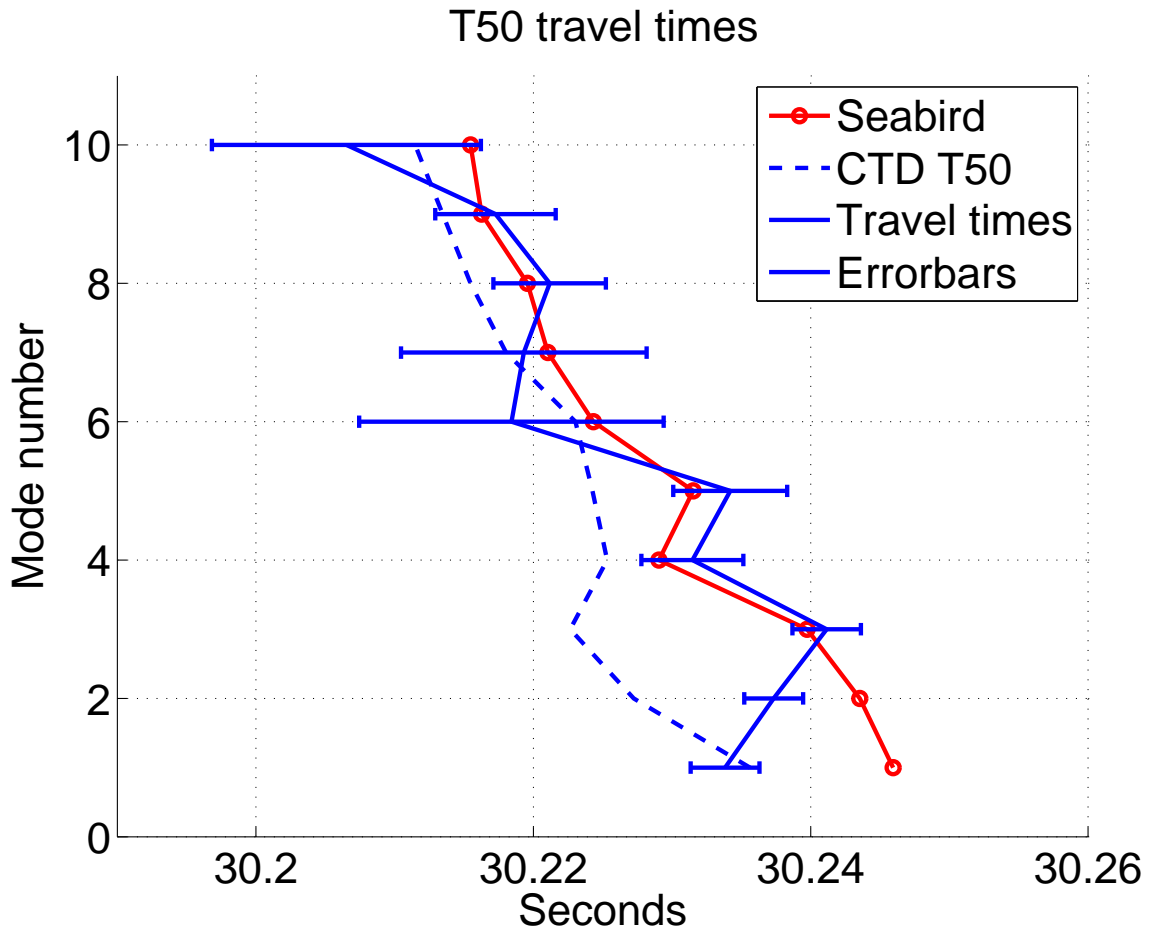


Figure 4.16: Travel time estimates at T50. The errorbars indicate the standard deviation. The travel time estimates are closer to the Seabird SSP measured at the array than the CTD profile measured at the source.

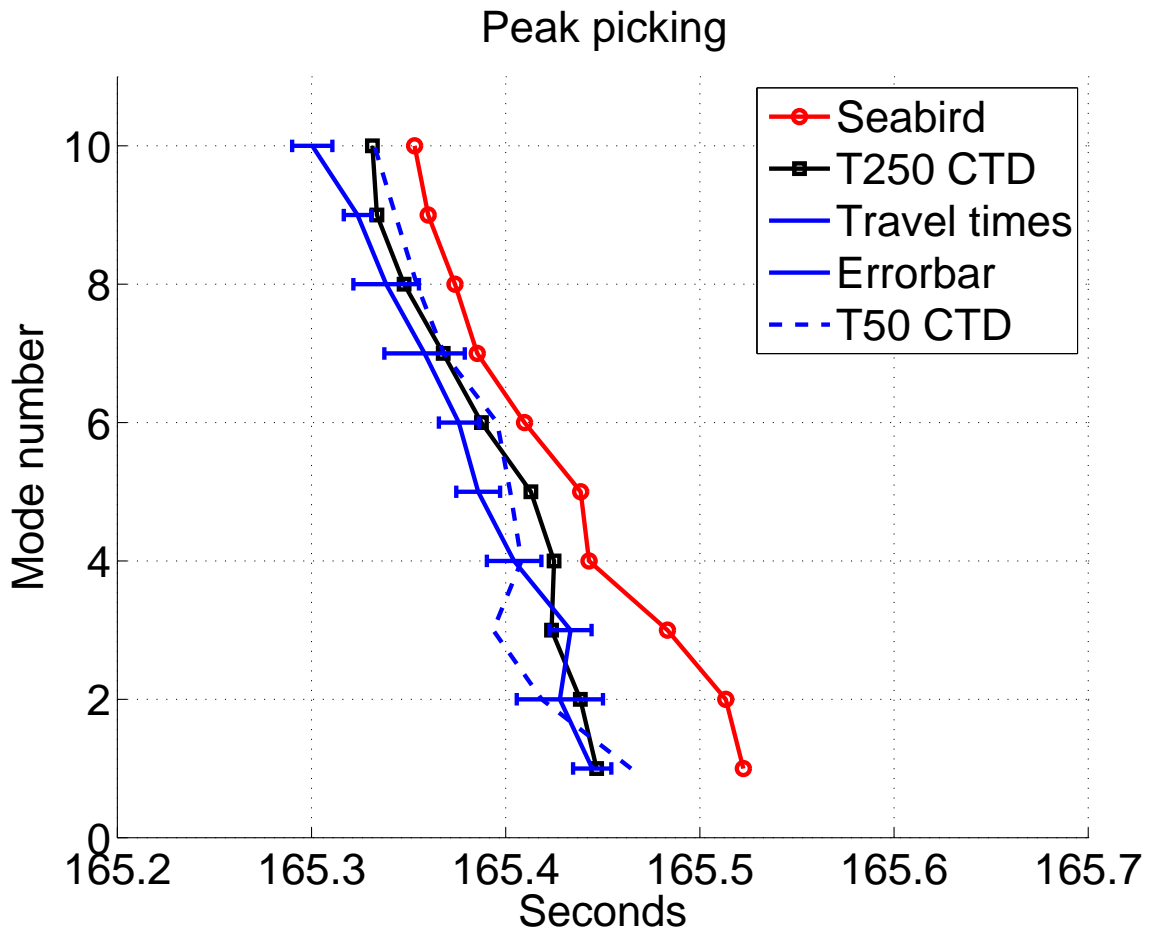


Figure 4.17: Travel time estimates at T250. The errorbars indicate the standard deviation. The travel time estimates for the three different methods all lie close to the travel times predicted by the profiles at T50 and T250.

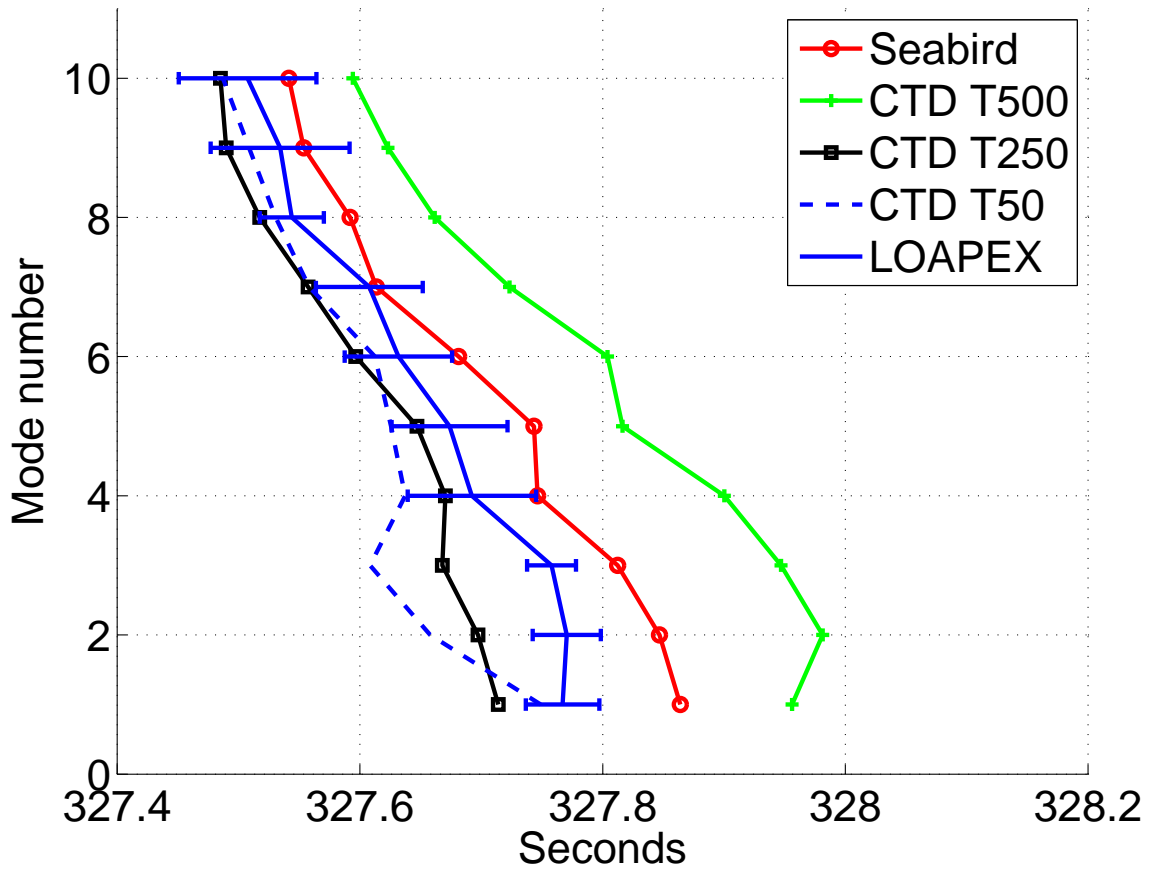


Figure 4.18: Travel time estimates at T500. The errorbars indicate the standard deviation. The mean travel time estimates lie midway between the predictions made using the different profiles. The variance of the travel times is much greater than at T50 and T250.

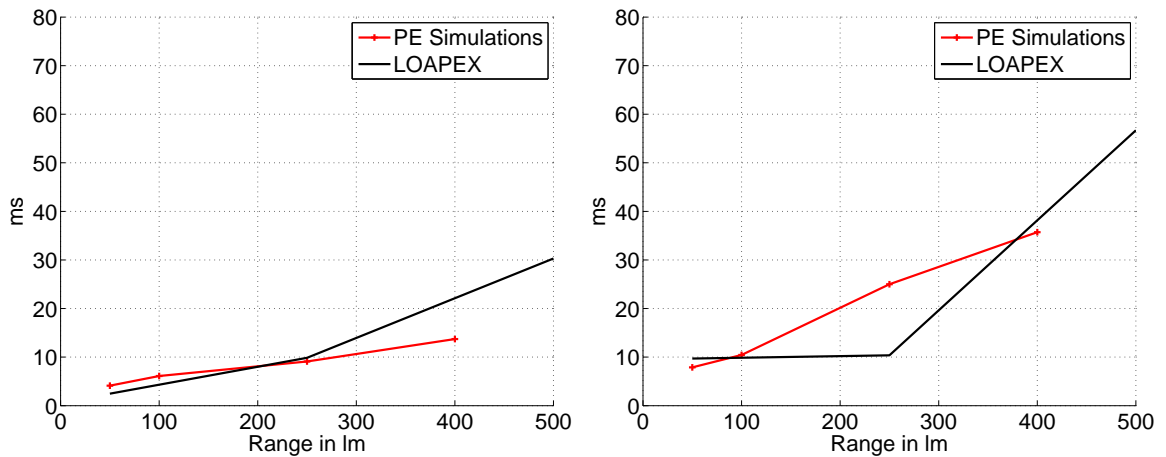


Figure 4.19: Travel time standard deviation for modes 1 and 10 during LOAPEX.

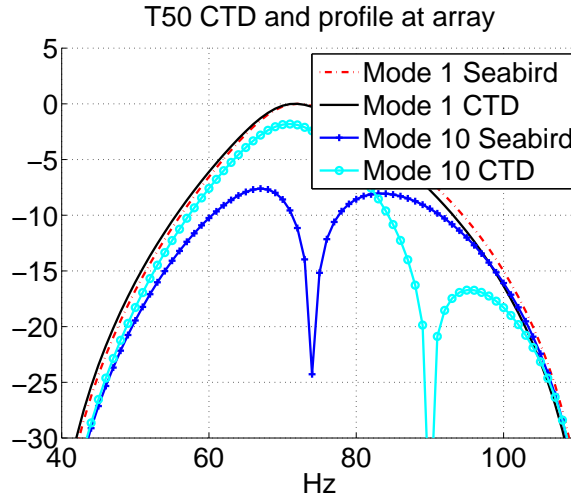


Figure 4.20: Seabird (yearday 259) and the T50 CTD spectrum for modes 1 and 10. The background spectrum varies for the two SSPs. However, mode 10 for both the profiles is weakly excited.

consider Figure 4.22, which shows the mode 10 spectrum at the array estimated using the Seabird measurements made during the T50 transmissions. The Seabird mode 1 spectrum does not vary much with time, whereas mode 10 shows significant variability. Figure 4.21 shows the spectrum for modes 1 and 10 for the different receptions at T50. Mode 1 is relatively constant across time and mostly resembles the source spectrum. However, mode 10 contains nulls in its spectrum. The CTD spectrum has a null at 90 Hz and the LOAPEX mode 10 contains nulls around 80 Hz to 90 Hz. The amount of variability in the mode 10 spectral nulls is similar to the variability in the Seabird mode 10 nulls in Figure 4.22. The variability in modes 1 and 10 is similar to the variability in the Seabird modes in Figure 4.22, which suggests that most of the variations in the T50 modes are due to the variations in the source spectrum.

*T250 spectrum:* Figure 4.24 shows the T250 mode spectra. At T250 the higher frequencies of mode 1 show amplitude variability. Figure 4.23 for the T250 spectrum shows that mode 1 does not contain any null in its excitation spectrum. Further, the Seabird mode spectra in Figure 4.22 showed that mode 1 spectrum does not vary much over time. The amplitude variability in mode 1 spectrum is hence due to the constructive and destructive interference

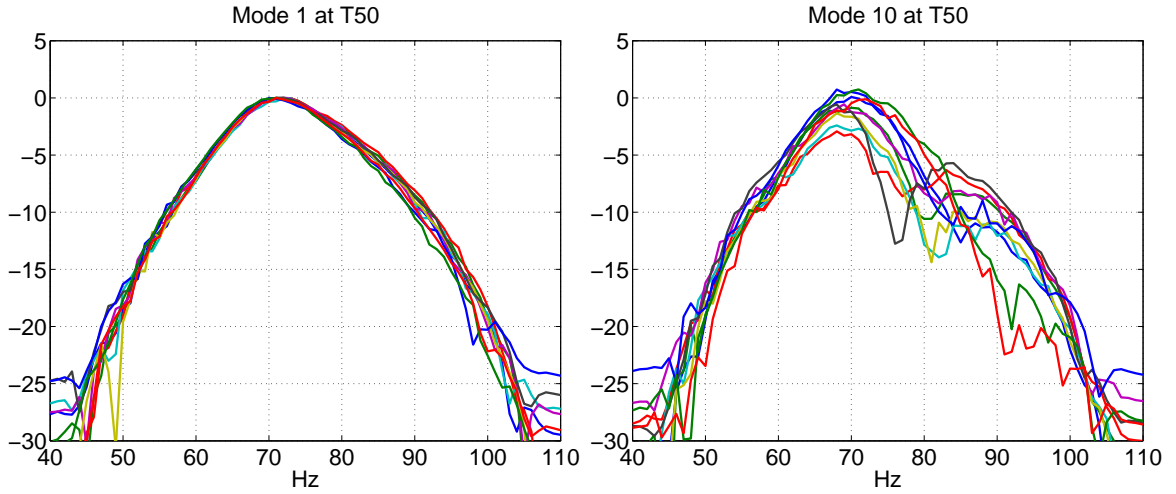


Figure 4.21: Modes 1 and 10 spectra at T50. Mode 10 shows more variability than mode 1. For some of the receptions, mode 10 contains nulls around 80 Hz.

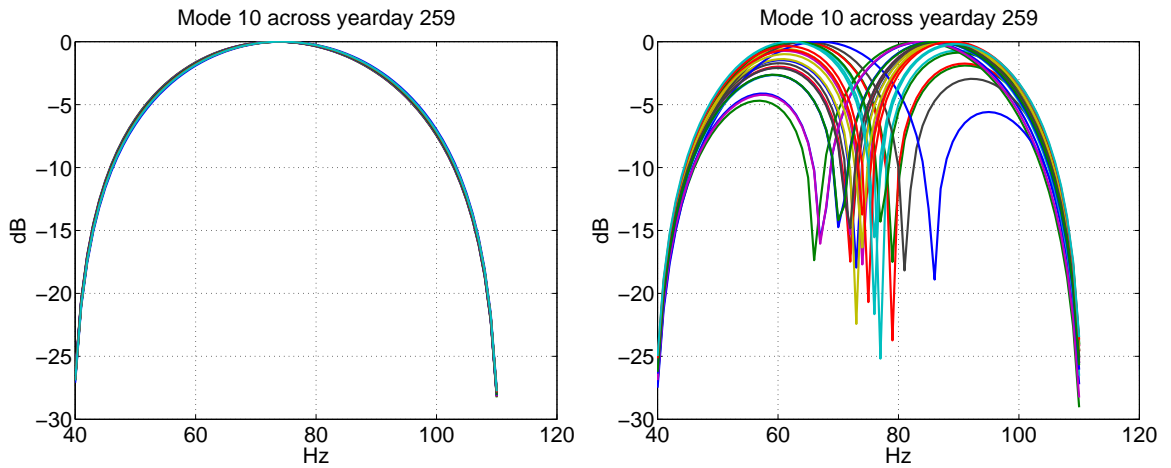


Figure 4.22: Spectrum for modes 1 and 10 during yearday 259.

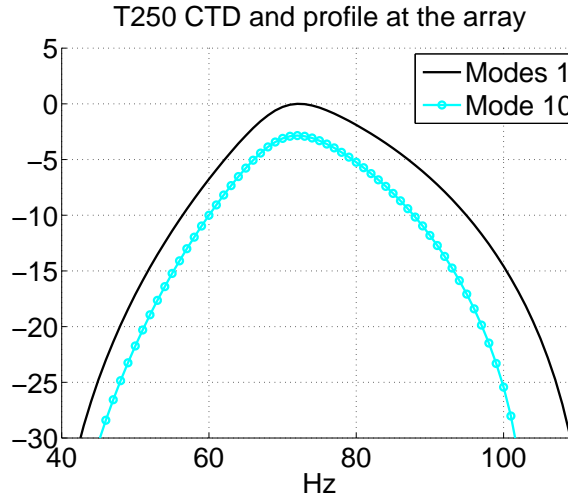


Figure 4.23: Mode 1 and 10 spectrum at T250. Mode 10 is excited at much lower level than mode 1.

from other modes. Internal waves generally increase as function of frequency and thus the higher frequencies of mode 1 show more scattering. Mode 10 at T250 unlike at T50, shows some amount of amplitude variability for low frequencies also. The T250 LOAPEX modes show more scattering and less correlation with the source excitation spectrum, which agrees with the model in Chapter 3.

*T500 spectrum:* Figure 4.25 shows the mode 1 and 10 spectra at T500. Chapter 3 predicted that for ranges on the order of 400 km or greater, modes 1 to 10 undergo frequency selective fading. The T500 LOAPEX modes 1 and 10 show significant amount of amplitude variability due to fading, which agrees with the model in Chapter 3.

#### 4.4.3 Time coherence for modes 1 and 10

The time coherence for the LOAPEX modes was calculated as follows. The 11 x 3 M sequence periods of each of the LOAPEX transmissions were frequency transformed and the mode amplitudes calculated in the 75 Hz bin. Because each transmission consisted of three parts with start times of 0 s, 400 s and 800 s, it yielded 11 measurements of the narrowband mode amplitudes spaced at times of 0 s, 400 s and 800 s for each transmission. The narrowband mode amplitudes at 0 s were then correlated with their counterparts

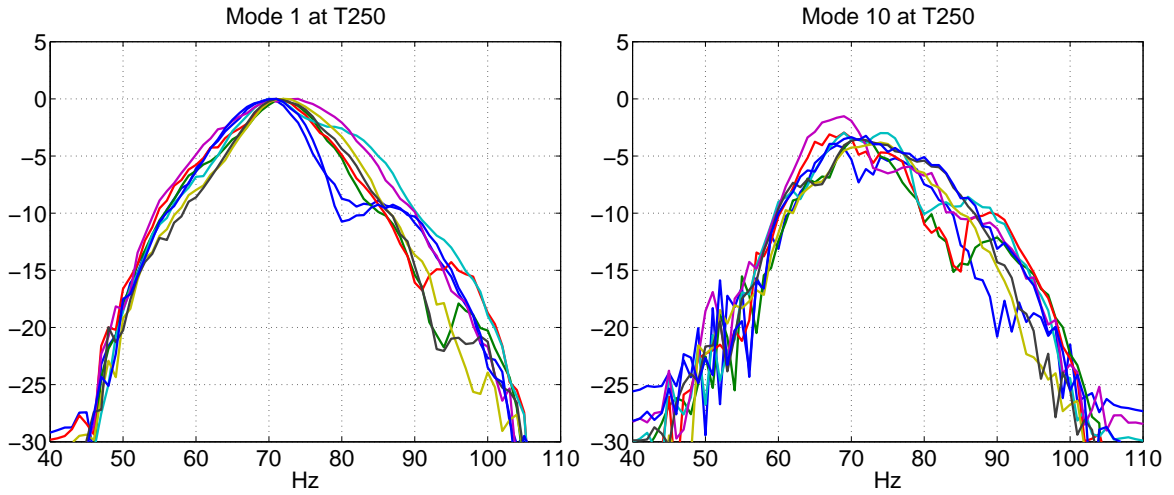


Figure 4.24: Modes 1 and 10 spectra at T250. Mode 1 shows more amplitude variability than at T50. Mode 10 still shows more variability for the higher frequencies, however the lower frequencies of mode 1 have started showing more variability than at T50.

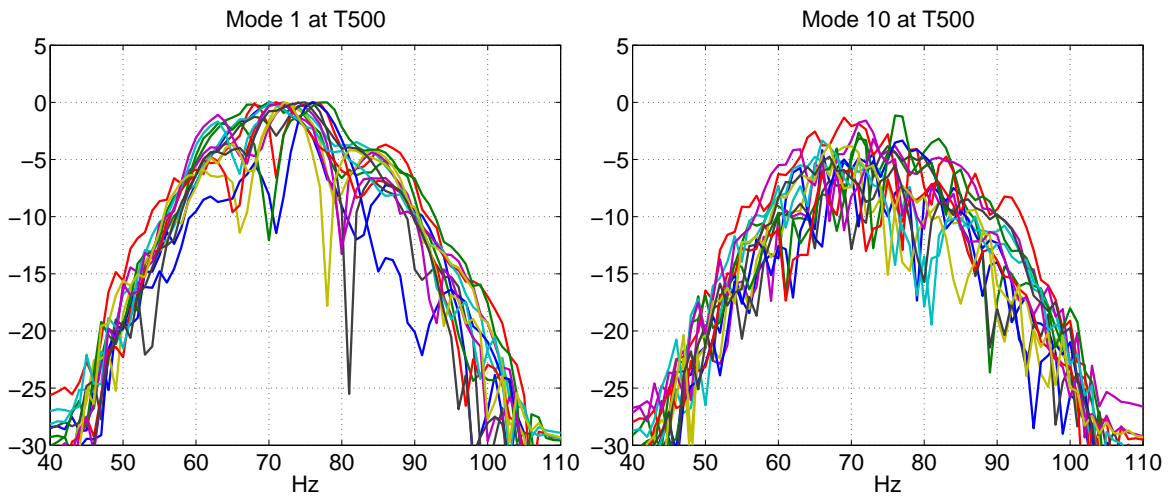


Figure 4.25: Modes 1 and 10 spectra at T500. Both the modes show the same amount of variability. The amount of amplitude variability is almost the same across frequency.

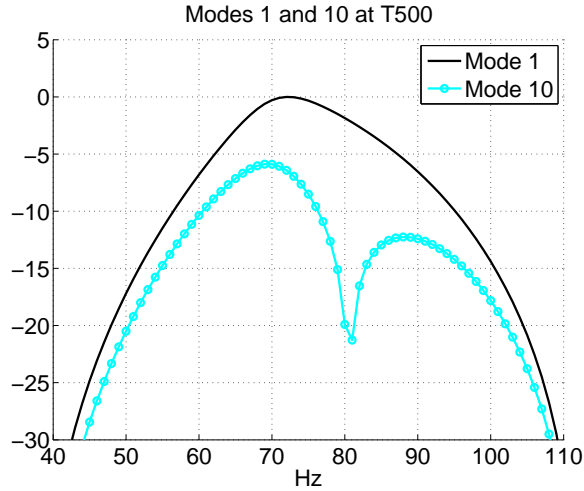


Figure 4.26: Mode 1 and 10 spectrum at T500. Mode 10 is excited at much lower level than mode 1.

that occurred 400 s and 800 s later. The results of the cross-correlation was averaged across the multiple M sequence periods and normalized to estimate the time coherence. Figures 4.27, 4.28 and 4.29 show the time coherence of modes 1 and 10 at T50, T250 and T500 respectively. The time coherence of modes 1 and 10 decrease with respect to range due to increase in scattering. However, the time coherences of the LOAPEX modes are shorter than the predictions in Chapter 3. The shorter time coherences are due to the noise in LOAPEX receptions.

## 4.5 Conclusions

This chapter discussed the challenges in LOAPEX mode processing and how they were met. The current literature does not contain any information about the range-dependent mode statistics estimated from experiments. The LOAPEX mode statistics estimated from the transmissions at different ranges along the same propagation path are hence a valuable addition to the literature. The LOAPEX mode time series at the different ranges agree with the model predictions in Chapter 3. The mode spectrum at the different ranges validate the predictions in the previous chapter that at T50, the source excitation spectrum has a

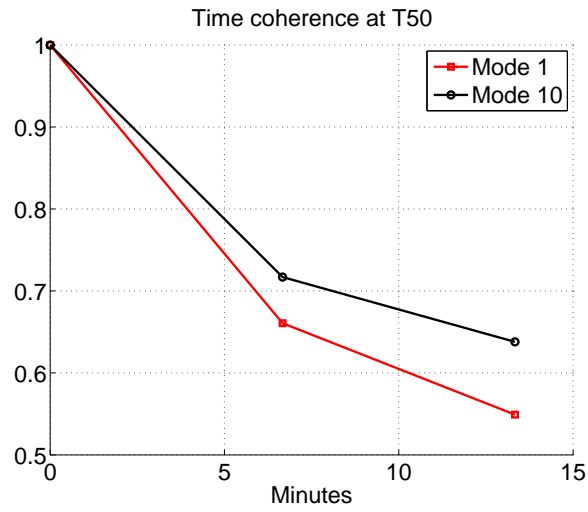


Figure 4.27: Time coherence at T50

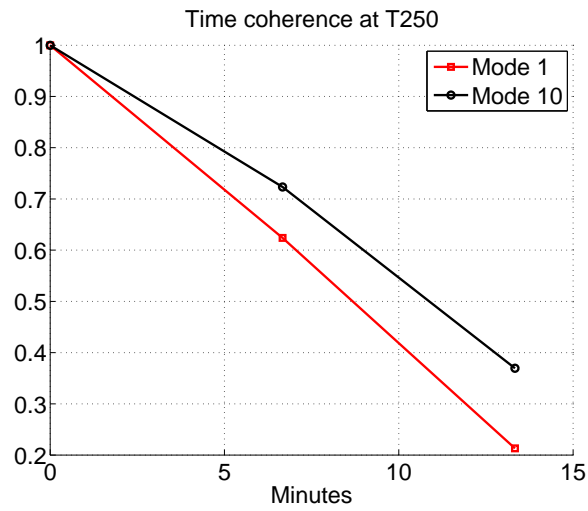


Figure 4.28: Time coherence at T250

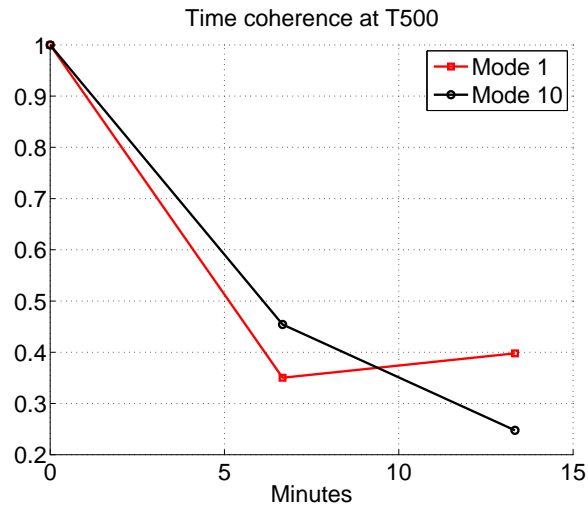


Figure 4.29: Time coherence at T500

significant influence on the mode spectrum. The amplitude variability of modes 1 and 10 at the different ranges are an useful method to analyze the amount of mode scattering at different ranges.

## Chapter 5: Detection methods for mode signals

This chapter uses the concept of Matched Subspace Detectors developed by Scharf to estimate the travel times of the modes at short ranges [42] [43]. In order to build the case for using MSDs this chapter is organized into three parts. First, section 5.1 discusses the application of matched filters to make travel time estimates for modes propagating an environment with no internal waves. Following that, Section 5.2 shows that the perturbations in the background spectrum due to internal waves cause mismatch in the matched filter. MSDs are presented as alternative to the elementary matched filter to accommodate the perturbations to the excitation spectrum. Section 5.3 discusses the statistics of the travel times estimated using the MSDs. Section 5.4 concludes the chapter.

### 5.1 Optimum detection methods in the absence of internal waves : quiescent matched filter

This section first describes the travel time estimation methods for a purely dispersive channel and then explores how they perform in the presence of internal waves. In discussing the performance of the MSDs for the modes, the presentation is similar to the previous chapters in that the discussion focuses on modes 1 and 10.

Consider a source with the spectrum  $H(f)$  plotted in Figure 5.1. The source response has a maximum at 75 Hz and is symmetric around the peak. In a dispersive channel that does not have any multipath due to internal wave scattering, the time series  $h(t)$  at range  $r$  is given by,

$$h(t) = \int_f H(f) e^{j2\pi ft} e^{-jk_m r} df \quad (5.1)$$

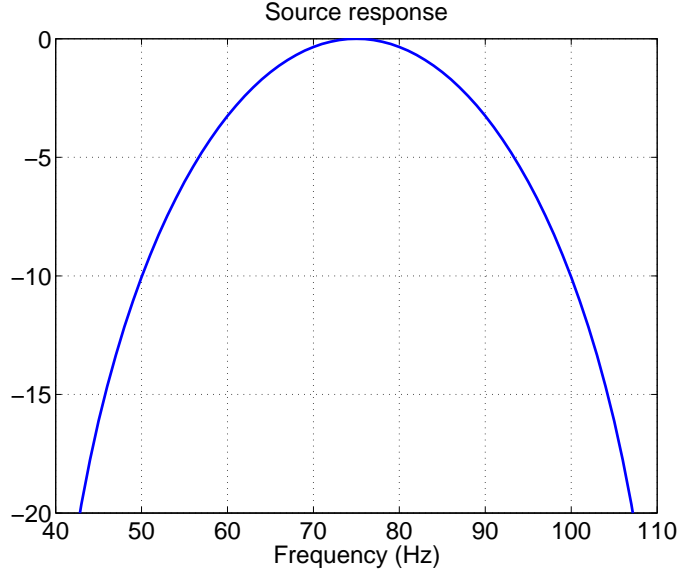


Figure 5.1: Finite bandwidth source response  $H(f)$ . The frequency response spans frequencies of 40 Hz to 110 Hz and has a peak at 75 Hz.

Note that the above equation does not take into account the  $\frac{1}{\sqrt{r}}$  dependence due to cylindrical spreading across range. In the above equation, the wavenumbers  $k_m$  vary as a function of the frequency. The above equation is similar to the frequency transform for the source signal but also accounts for the dispersive spread via the  $k_m$  terms. In a dispersive channel, the different frequencies have different group velocities, hence arrive at different times. The amplitudes of the different arrivals are in proportion to the amplitudes of the source response. Thus the dispersed time series has a peak at the travel time corresponding to the 75 Hz component. The method for calculating the travel time of the 75 Hz component consists of measuring the time of arrival of the peak of the time series.

The modes have a more complicated spectrum than Figure 5.1. Consider the SSP in Figure 5.2 that was measured during LOAPEX. The figure indicates the location of an axial source placed at depth  $z_s = 800$  m. Chapter 2 gave the expression for the broadband mode ( $m$ ) signal at range  $r$  as

$$a_m(t) = \int_f H(f) \Psi_m(z_s, f) e^{j2\pi ft} e^{-jk_m r} df. \quad (5.2)$$

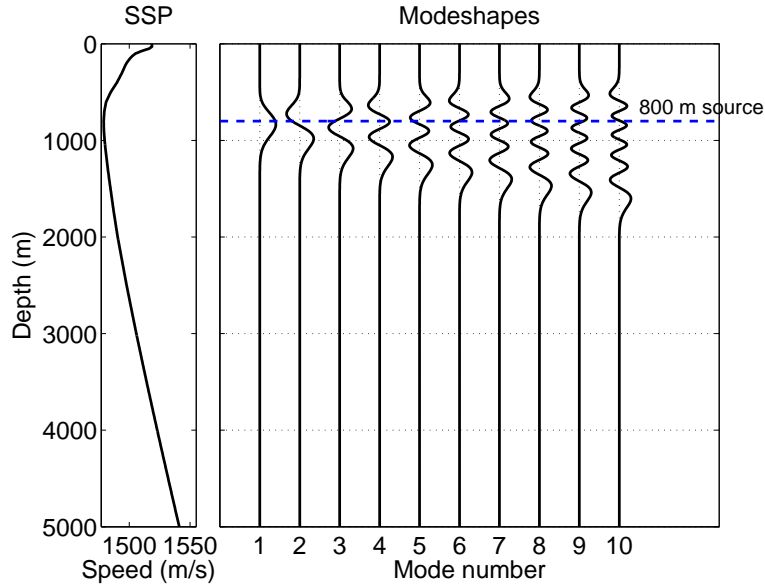


Figure 5.2: Sound speed profile and the modeshapes for the LOAPEX path. The left subplot shows the average sound speed profile for the LOAPEX path derived from the World Ocean Atlas [2,3] database. The right subplot shows the modeshapes at 75 Hz of modes 1 to 10 calculated from the sound speed profile.

According to Equation 5.2, the source response in Figure 5.1 is weighted by the narrowband mode amplitudes at the source depth for each frequency. For convenience sake, we refer to the product of the background mode amplitudes  $\Psi_m(z_s, f)$  and the source spectrum  $H(f)$  as the quiescent spectrum. The name ‘quiescent’ denotes the unperturbed ocean (without internal waves). The mode amplitudes were calculated for frequencies 40 Hz to 110 Hz by solving for the modes associated with the SSP in Figure 5.2. Figure 5.3 shows the source excitation spectrum for modes 1 and 10. Mode 1 has a flat mode spectrum, hence the source excitation spectrum for mode 1 mostly resembles the source spectrum  $H(f)$  in Figure 5.1. Mode 10, unlike mode 1, has nulls in its spectrum thus the source excitation spectrum has nulls and is also asymmetric. Figure 5.4 shows the mode time series for modes 1 and 10 calculated using Equation 5.2 at 50 km. The mode time series for each mode reflects the respective mode source excitation spectrum in Figure 5.3. Mode 10, unlike mode 1, has a null in its spectrum and hence gives rise to an asymmetric time series with a null. Because mode 1 has a peak at 75 Hz, the peak of the mode time series occurs at the time of arrival

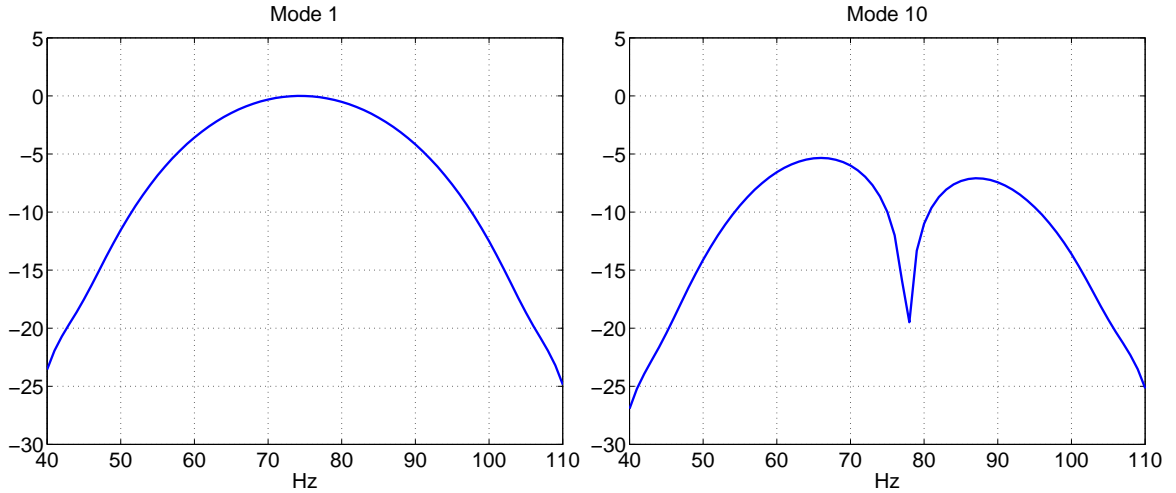


Figure 5.3: quiescent frequency response. The mode amplitudes for frequencies 40 Hz to 110 Hz weighed with the source response in Figure 5.1. Modes 6, 9 and 10 contain nulls close to 75 Hz.

for the 75 Hz component. Mode 10, however, has a double peaked arrival structure and has a null at the time of arrival corresponding to the time of arrival of the 75 Hz component. Thus, peak picking does not work well to estimate the arrival time of mode 10.

The discussion until now has shown that peak picking works best for a symmetric time series. The travel time estimation method for a different mode spectrum such as mode 10 should take into account the background spectrum. This thesis uses matched filtering techniques to estimate the travel time of the mode signals. The matched filter, originally called the North Filter [44], is used to detect the presence of a known signal in an Additive White Gaussian Noise (AWGN) channel. Another application of the matched filter is pulse compression. Pulse compression is routinely used in RADAR [45], ocean acoustic tomography [1] and digital communications [46] to make minimum mean square estimates of the travel time of a signal. This thesis uses the pulse compression application of the matched filter. Pulse compression can be explained as follows. Consider the broadband mode time series  $b_m(t)$  such that,

$$b_m(t) = a_m(t - t_0) + q_m(t) \quad (5.3)$$

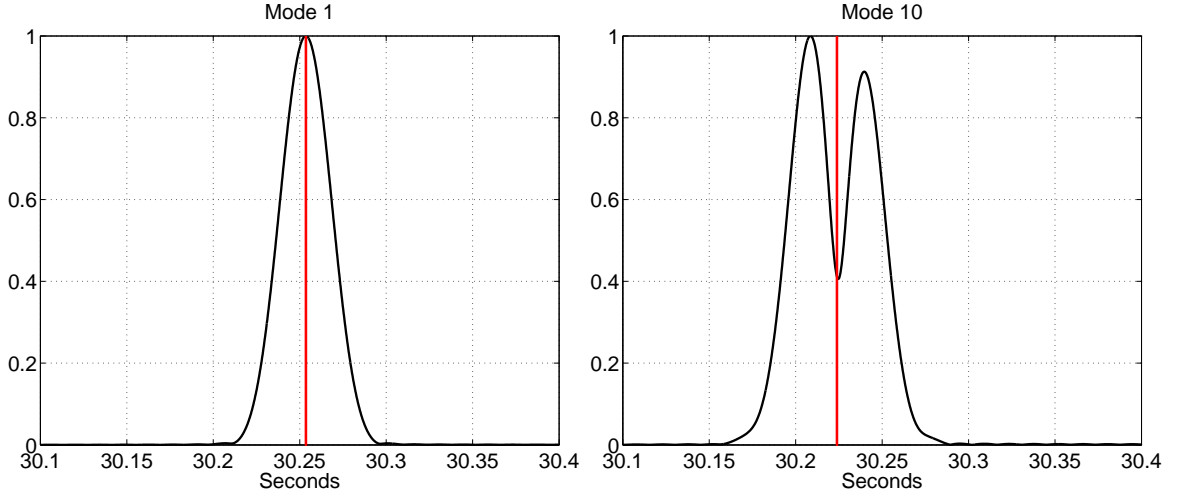


Figure 5.4: Quiescent time series for modes 1 and 10 (black) and the time of arrival of the 75 Hz component for each mode (red). The time of arrival of the peak of mode 10 differs from the 75 Hz component.

where  $a_m(t)$  is the mode time series and  $q_m(t)$  is the background noise. The travel time  $t_0$  of the mode signal is unknown. Pulse compression consists of convolving the signal  $b_m(t)$  with a template of the time reversed version of the transmitted signal  $a_m(t)$ . Matched filtering is equivalent to cross-correlation. By principle, cross-correlation is guaranteed to produce a symmetric output with a peak corresponding to the time of arrival of the signal. The pulse compression operation of the matched filter is thus used to make travel time measurements for the mode signal. The equations above expressed in continuous time domain can be discretized in time as,

$$\mathbf{b}_m = \mathbf{a}_m + \mathbf{q}_m \quad (5.4)$$

where the column vectors  $\mathbf{b}_m$ ,  $\mathbf{a}_m$  and  $\mathbf{q}_m$  contain the samples of the signals  $b_m(t)$ ,  $a_m(t)$ ,  $q_m(t)$  respectively. For example the observation vector  $\mathbf{b}_m$  is given by,

$$\mathbf{b}_m = \begin{bmatrix} b_m(1) \\ b_m(2) \\ \vdots \\ b_m(k) \end{bmatrix} \quad (5.5)$$

Equation 5.4 describes a one dimensional (1D) signal ( $a_m$ ) embedded in background noise ( $q_m$ ). Pulse compression for signal  $a_m$  consists of convolving the signal  $b_m$  with time reversed version of the conjugate of  $a_m$ , or in other words cross-correlating the signal  $b_m$  with the template  $a_m^*$ <sup>1</sup>. Cross-correlation is a basic signal processing technique and can be interpreted in a number of ways. In discussing how cross-correlation can be implemented for modes, this thesis uses the approach by Scharf in [43] and Scharf and Friedlander in [42] that uses projection operators. The matched filtering operation for the signal model in Equation 5.4 is given by,

$$l = \mathbf{a}_m^H \mathbf{P}_a \mathbf{a}_m \quad (5.6)$$

The projection matrix  $\mathbf{P}_a$  for  $\mathbf{a}_m$  is given by,

$$\mathbf{P}_a = \frac{\mathbf{a}_m \mathbf{a}_m^H}{\mathbf{a}_m^T \mathbf{a}_m} \quad (5.7)$$

The quiescent matched filter, given by equation 5.7, implements cross correlation by projecting the signal  $\mathbf{b}_m$  on to the 1D space defined by  $\mathbf{a}_m$ . The projection operation in Equation 5.6 is equivalent to an energy detector for signals in the 1D space defined by Equation 5.7. The output of Equation 5.6 has a maximum corresponding to the time of arrival of the signal.

Figure 5.5 shows the output of the quiescent matched filter for modes 1 and 10. The quiescent detector for modes that contain no nulls compensates for the dispersive spread for

---

<sup>1</sup>\* denotes complex conjugate

each mode. For mode 10 that has a null, the quiescent detector compensates for the nulls and gives a peak at the time of arrival of the desired signal. Thus the quiescent matched filter accommodates the different mode spectra and makes accurate travel time estimates for modes 1 and 10.

In order to analyze the error statistics of the quiescent filter and the peak picking method an estimation error was defined. The travel time estimation error for the quiescent filter is the difference in times of arrival of the peak of the matched filter and the predicted time of arrival for the 75 Hz component. The travel time estimation error for peak picking was also defined in a similar manner. It should be noted that the background noise is small compared to the coupling contributions. The simulations thus did not include the effect of noise. Figure 5.6 shows the travel time estimation error for modes 1 to 10 at 50 km. Peak picking has a minimal amount of error for modes 1, 2, 4 and 8 that have no nulls in their spectrum. However for mode 10 that has a null in its spectrum the travel time estimation error is much higher on the order of 16 ms. The increased error is due to the fact that the peak picking method incorrectly chooses the peak of the mode arrival that does not occur at the time of the arrival of the 75 Hz component (Figure 5.4). The performance of the peak picking method similar to mode 10 is also bad for modes 3, 6, 7, and 9 which also have nulls in their spectrum. For the quiescent matched filter, the travel time estimation error is almost zero for modes 1 to 10. The quiescent detector compensates for the nulls and gives the exact estimate of the background travel times.

## **5.2 Detection methods for internal wave perturbed modes: Matched Subspace Detectors**

The quiescent filter is based on the mode spectrum calculated for the background sound speed profile. As mentioned in the previous chapters, internal waves induce perturbations in the excitation spectrum of the modes. Consider Figure 5.8, which shows the excitation spectra for modes 1 and 10 for two different internal wave realizations. The spectra for these

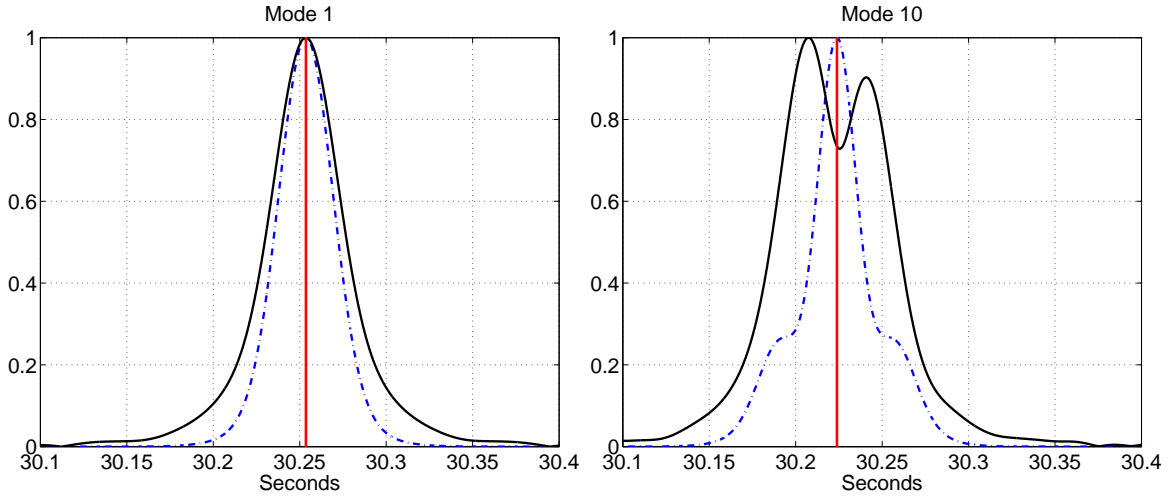


Figure 5.5: The quiescent time series (black), the output of the quiescent detector (blue -) and the the travel time of the 75 Hz component of the background profile for modes 1 and 10. The peak of the quiescent detector matches the time of arrival of the 75 Hz component.

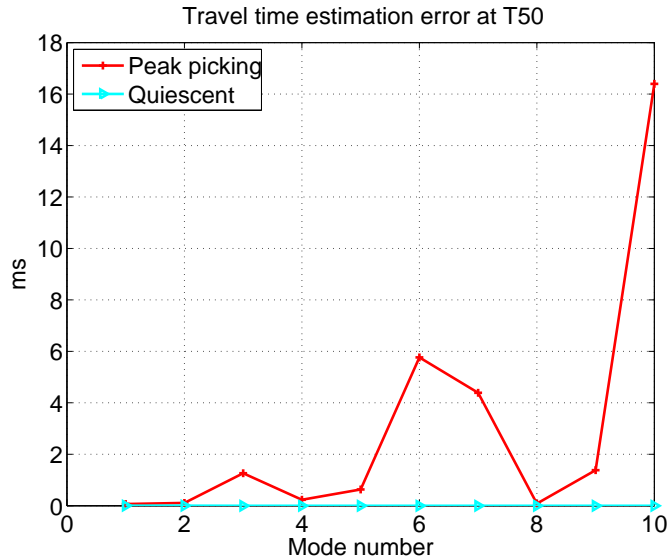


Figure 5.6: Performance of the quiescent matched subspace detector at T50, no internal waves. The travel time estimation error is defined as the difference between the travel time estimate and the predicted travel times at 75 Hz. The quiescent matched filter recovers the background travel times.

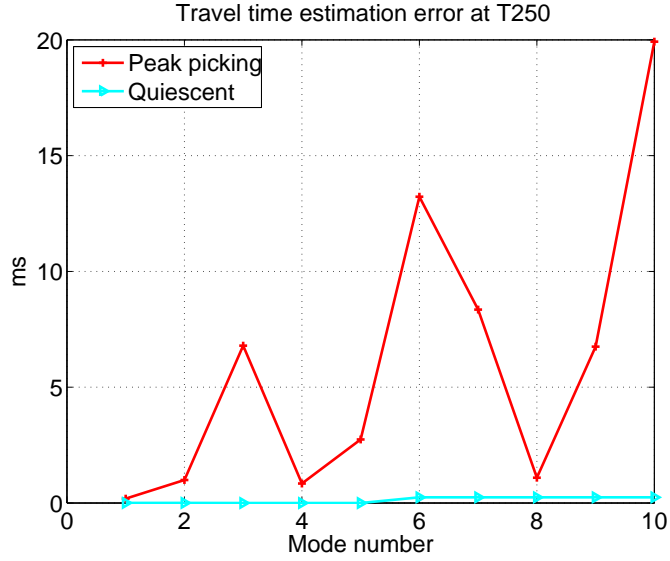


Figure 5.7: Performance of the quiescent matched subspace detector at T250, no internal waves. The travel time estimation error is defined as the difference between the travel time estimate and the predicted travel times at 75 Hz. The quiescent matched filter recovers the background travel times.

realizations differ from each other and the quiescent spectrum. The spectrum for mode 1 does not vary much, but the spectrum for mode 10 shows significant variations from one realization to the other. Specifically, the location of the nulls in the mode 10 spectrum varies substantially with each realization. The quiescent filter based on the background spectrum is poorly matched to the mode spectrum perturbed due to internal waves. In order to make travel time estimates of modes perturbed by internal waves, the quiescent filter must be modified to take into account the perturbations to the source amplitude. The modified quiescent filter must be flexible enough to accommodate the change in excitation spectrum with respect to mode number and the statistics of the internal wave perturbations.

This section addresses travel time estimation for the modes in two parts. The first part describes a linear subspace model for internal wave perturbations at the source depth. The second subsection uses the model to construct MSDs for travel time estimation of modes.

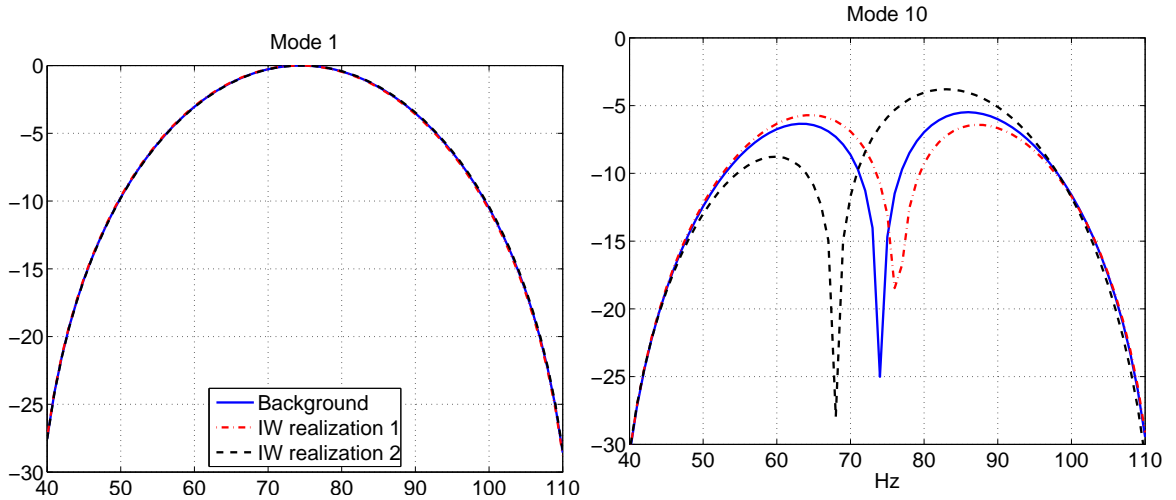


Figure 5.8: The source excitation spectrum for 2 different internal wave realizations (black ‘-’ and red ‘.’) and the quiescent spectrum (blue ‘-’). Internal waves cause variations in the source excitations spectrum. Mode 10 shows significant variation in mode spectrum for internal wave variations.

### 5.2.1 Linear subspace model for mode signals perturbed by internal waves

Simulations were performed to calculate a basis set that describes the perturbations to the spectral amplitudes. Sound speed perturbations due to internal waves of half GM strength were simulated using the Colosi and Brown method [12] and added to the measured LOAPEX background SSP in Figure 5.2. The narrowband mode amplitudes for the perturbed SSPs and the source spectrum  $H(f)$  in Figure 5.1 were substituted in Equation 5.2 to calculate the source pulse  $a_m(t)$  for the different internal wave realizations at a range of  $r = 50, 250$  km. The correlation matrix for the internal wave perturbed source excitation time series  $a_m(t)$  was estimated and an SVD [47] analysis performed to estimate the temporal EOFs ( $g_1, g_2, \dots, g_k$ ) of the time series. Figure 5.9 shows the cumulative energy in the first 5 EOFs. The plot for the cumulative energy shows two things. First, The EOFs 1 and 2 are sufficient to describe most of the perturbations. Second, EOF 1 contributes a significantly lower percentage of energy for modes 3, 6, 7, 9 and 10 implying that the source excitation spectra for those modes needs more than 1 EOF. The first 2 EOFs thus constitute a temporal subspace for the modes. Based on the observation that up to 2 EOFs are needed to model the modes,

$$\mathbf{a}_m = \sum_{k=1,2} \mathbf{g}_{k,m} \theta_{k,m} \quad (5.8)$$

The weights  $\theta$  that denote the contribution of each EOF to the mode time series vary from internal wave realization to the other. The internal wave perturbed mode signals thus lie in a 2-D subspace. On comparing the modes perturbed by internal waves to the quiescent modes, the internal waves have introduced an extra degree of complexity to the mode signals. Where the quiescent filter needed only one basis vector (defined by only the background mode excitations), the internal wave perturbed mode signals require up to 2 basis vectors. Figure 5.10 shows the the first 2 EOFs for modes 1 to 10. The frequency domain plot of the EOFs gives a better idea of the difference between the first two EOFs. Figure 5.11 shows the Fourier transform of the first two EOFs for each mode. The spectrum of the first EOF is similar to the quiescent spectrum. The first EOF thus models the background spectrum and the second EOF models the variations to the background spectrum. The EOF-based model thus accommodates the quiescent mode time series and the perturbations to the mode time series. Writing Equation 5.8 in matrix form,

$$\mathbf{a}_m = \mathbf{G}_m \boldsymbol{\theta} \quad (5.9)$$

### 5.2.2 Matched subspace detectors based on the linear subspace model

Substituting Equation 5.9 in Equation 5.4,

$$\mathbf{b}_m = \mathbf{G}_m \boldsymbol{\theta} + \mathbf{q}_m \quad (5.10)$$

The equation above describes an internal wave perturbed signal described by a 2 D model that lies in background noise. Scharf defined Matched Subspace Detectors (MSDs) to deal with signals that lie in a subspace such as the one in the above equation [42, 43]. The optimum detection statistic for the signal in Equation 5.10 is given by,

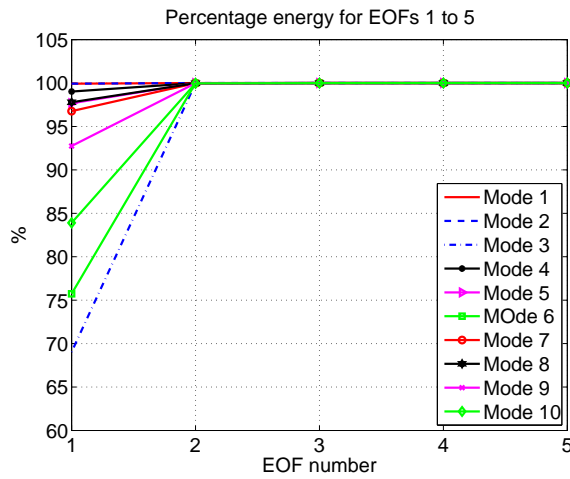


Figure 5.9: The percentage of energy of the first 5 EOFs of modes 1 to 10. All the modes are described by not more than 2 EOFs. In modes 6 and 10, the first EOF accounts for less than 90 percent of the total energy implying that modes 6 and 10 are more complicated.

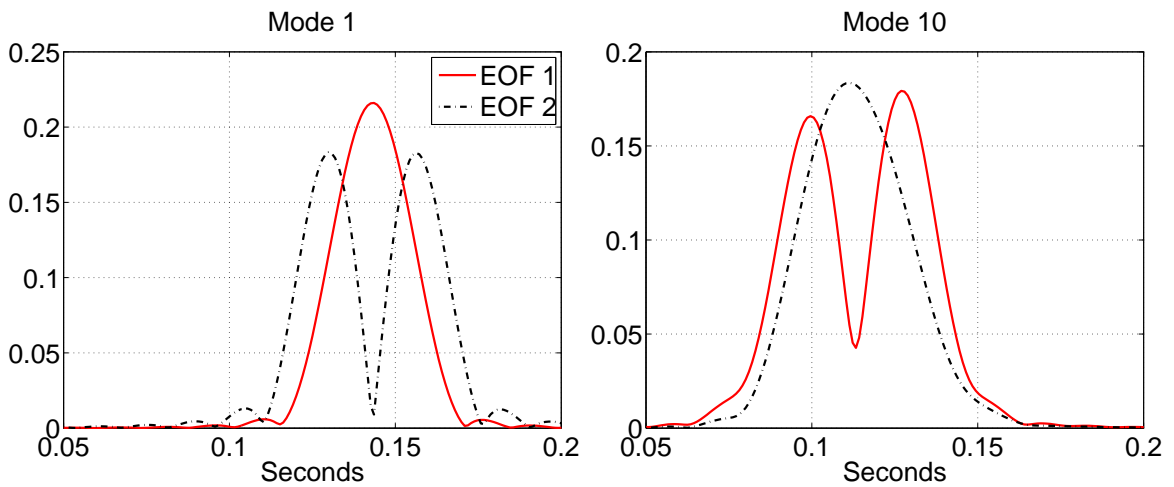


Figure 5.10: EOFs 1 and 2 for modes 1 and 10 at T50.

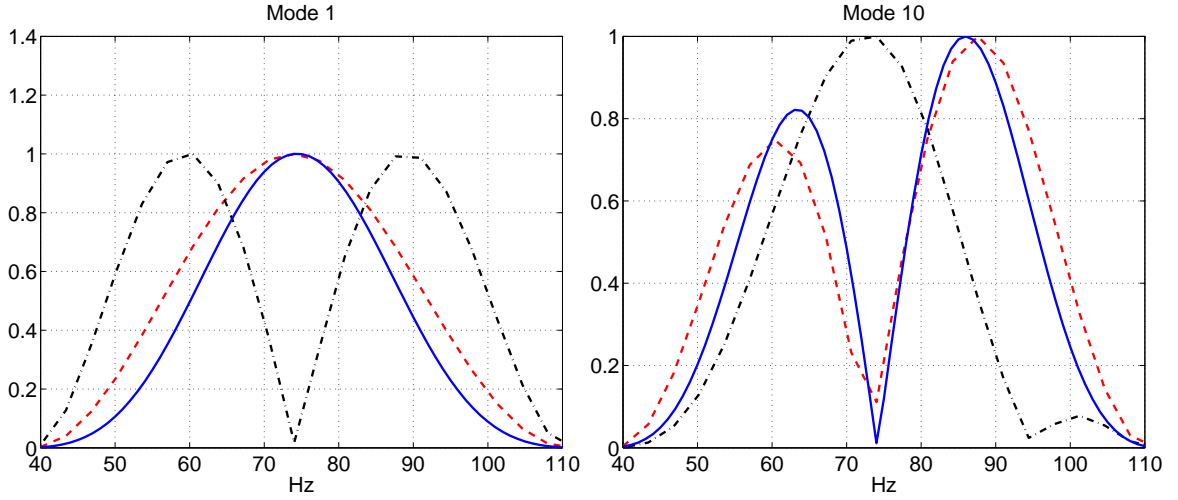


Figure 5.11: Comparison of the spectrum of the background profile (blue -), the spectrum of EOF 1 (red -) and the spectrum of EOF 2 (black -). The spectrum of EOF 1 is similar to the spectrum of the first EOF.

$$l = \mathbf{b}^H \mathbf{P}_G \mathbf{b} \quad (5.11)$$

The projection operator  $\mathbf{P}_G$  is given by,

$$\mathbf{P}_G = \mathbf{G}(\mathbf{G}^H \mathbf{G})^{-1} \mathbf{H}^G \quad (5.12)$$

The statistic 'l' in Equation 5.11 is similar to the statistics in Equation 5.6 and is a measure of the energy of the signal contained in subspace defined by  $\mathbf{P}_G$ . The MSD is thus an energy detector similar to the matched filter described in the previous section. Further note that for a 1D subspace, the MSD in Equation 5.12 becomes the matched filter in Equation 5.7. The matched filter is a special case of the MSD.

Based on the 2D model for each mode, two types of MSDS were considered. The first type is the 1D MSD based on the first EOF for each mode. The second type is the 2D MSD built using the first and second EOFs. To appreciate the benefits of the two 2D MSD versus the 1D MSD, it is helpful to observe the MSD outputs for mode signals affected due to internal waves. PE simulations modeling internal wave effects at ranges of 50 km, 250 km and

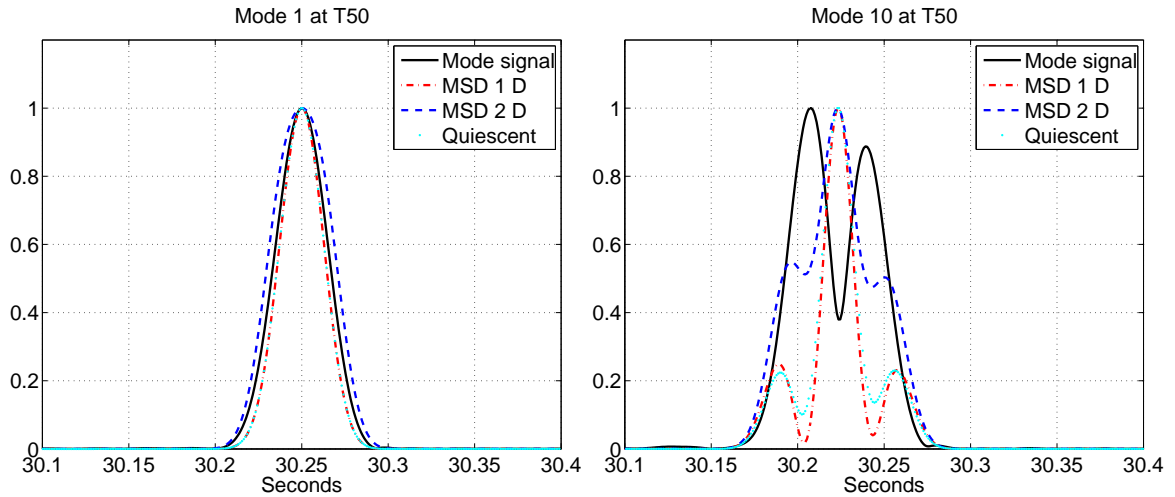


Figure 5.12: MSD sample output at 50 km for modes 1 and 10. MSD sample output at 50 km for modes 1 and 10. For modes 1 and 10, the 1 D MSD and the quiescent detector are matched to the signal arrival. The MSDs and the quiescent detectors compress the mode signal into a single arrival.

400 km were performed using the method described in the previous chapters. Figures 5.12 and 5.13 show modes 1 and 10 and the output of the MSDs for two different internal wave realizations. First consider the mode signals in Figure 5.12. Mode 1 has a single peaked arrival that resembles its first EOF in Figure 5.10 (left subplot). Similarly mode 10 has a two peaked arrival that resembles its EOF 1 in Figure 5.10 (right subplot). The 1 D MSD or the quiescent detector for modes 1 and 10 peak at the time corresponding to the travel time of the 75 Hz component of the background profile. Moving on to another internal wave realization, Figure 5.13, shows that mode 10 has a different arrival structure that is similar to its EOF 2 in Figure 5.10. The quiescent detector or the 1 D MSD have a peak output that is inconsistent with the background time of arrival. The 2 D MSD on the other hand is able to detect the perturbed mode. Based on the sample plots shown, the MSDs are capable of two things. First, the MSDs can accommodate different types of mode spectra. Second, the 2 D MSDs are also able to compensate the perturbations to the mode spectra.

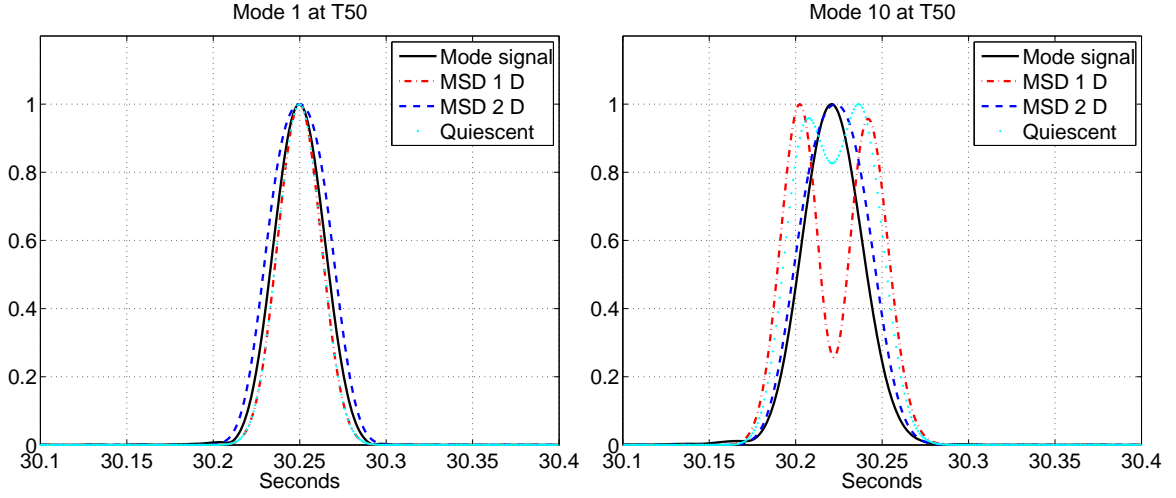


Figure 5.13: MSD sample output at 50 km for modes 1 and 10 for an internal wave realization. Mode 1 is similar to the arrival in Figure 5.12. Mode 10 on the other hand completely differs from the corresponding arrival in Figure 5.12. The 2 D MSD for mode 10 gives a more stable arrival with respect to the mode arrival in Figure 5.12.

### 5.3 Error statistics of the MSD travel time estimates

The main points of this chapter until now are as follows. The EOFs for the source excitation amplitudes provide a compact basis set to describe the perturbations to the source amplitudes. The MSDs based on the EOF model are a flexible framework to make travel time estimates for the modes perturbed by internal waves. This section compares the travel time estimation error of the 1D and 2D MSDs with peak picking and the quiescent detector presented in Section 5.1.

The peak output of the MSDs such as in the sample plots in Figures 5.12 and 5.13 were averaged across 50 realizations. The travel time estimation error is defined as the difference between the estimated travel time and the background travel time. Figure 5.14 shows the mean (left plot) and variance (right plot) of the travel time calculations for the 1 D MSD, 2 D MSD, quiescent detector and the mode signal for modes 1 to 10 at T50. The 2 D MSD has the lowest mean and variance in error. The MSD has significantly less error for modes 3, 6, 7, 9 and 10. Note that Figure 3.14 showed that the standard deviation of the travel times of mode 1 (for the range averaged LOAPEX profile) due to internal waves is between 4 ms to 5 ms. The internal wave induced travel time wander correlates well with

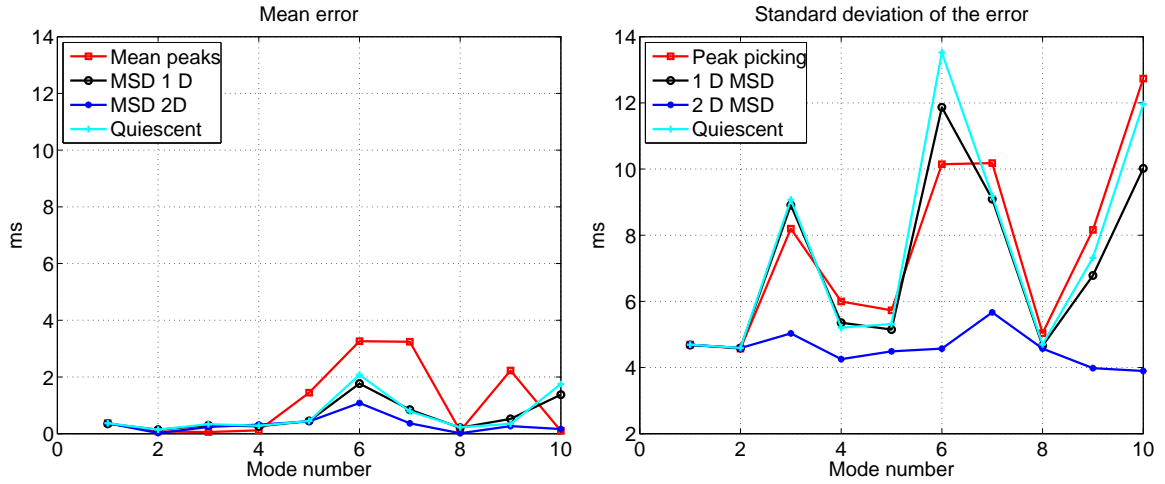


Figure 5.14: Travel time estimation at T50. For modes 3, 6,7,9 and 10 the 2 D MSD has a lower error and a more stable arrival.

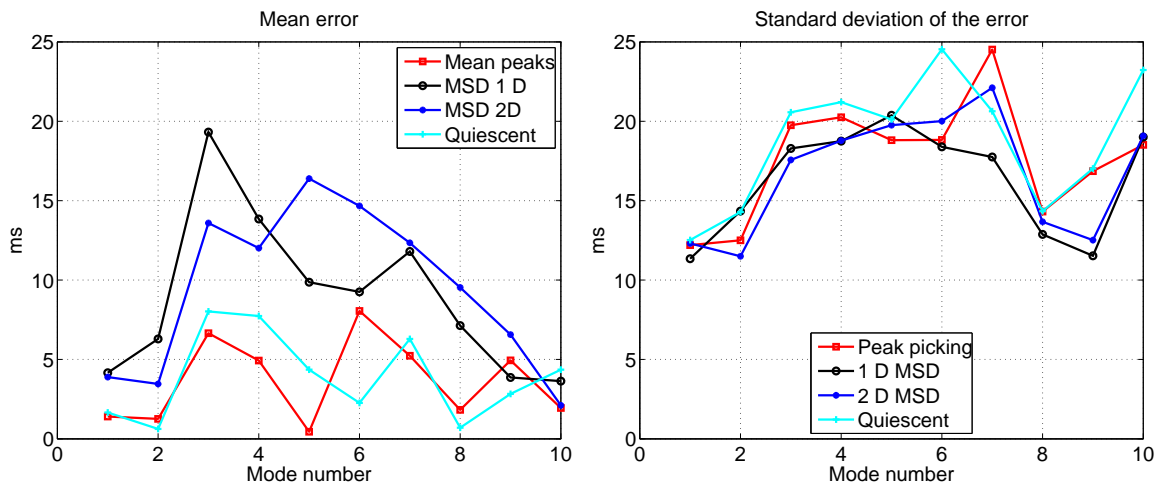


Figure 5.15: Travel time estimation at T250. Peak picking and the quiescent detector have a lower mean error than the MSDs

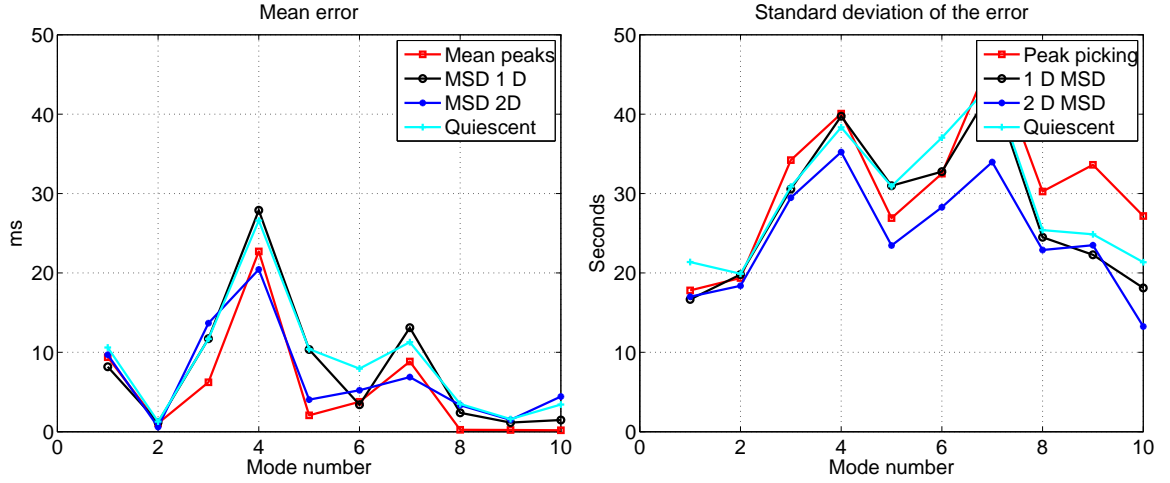


Figure 5.16: Travel time estimation at T400. Modes 1 and 2 have a lower travel time error and are more stable.

the standard deviation of the MSDs error in Figure 5.14. This implies that the wander in the travel time estimates is only due to internal wave variance and not due to estimation error.

The objective in measuring the travel time is to invert for the axial sound speed. To get an idea of the error in sound speed due to travel time estimation error, consider the following approximate expression for the error in axial sound speed,

$$\Delta c = c_0 \frac{\Delta T}{T} \quad (5.13)$$

In the above equation,  $c_0$  denotes the axial sound speed,  $\Delta T$  is the mode travel time estimation error and  $T$  is the actual mode travel time. For an axial sound speed of approximately 1500 m/s,

$$\Delta c = 1500 \frac{\Delta T}{T} \quad (5.14)$$

The mean travel time estimation error ( $\Delta T$ ) in figure 5.14 is around 1 ms. The travel time for the modes ( $T$ ) at T50 is around 30 s, thus hence by Equation 5.14, the sound speed error is on the order of 0.05 m/s.

Figure 5.15 shows the performance of the MSD at 250 km. The previous two chapters showed that at 250 km, coupling effects start contributing to the mode arrival. The EOFs described in the previous section are not perfectly suited to describe the MSD. Peak picking and the quiescent detector have the lowest error. The estimation error for the peak picking and the quiescent detector is between 1 ms to 7 ms. For MSDs, the mean error varies between 5 ms to 20 ms. Modes 1 and 2 have the lowest mean error. Contrary to the mean estimation error plots, the plot for the variance of the estimation error shows that the MSDs have a lower estimation variance than the quiescent detector and peak picking. The error statistics plots show that there is no clear winner between the MSDs and the other methods. At T250 the travel time  $T$  is around 165 s. The estimation error ( $\Delta T$ ) for peak picking is between 1 ms to 7 ms. Hence by Equation 5.14, the sound speed estimation error for peak picking is on the order of 0.009 m/s to 0.05 m/s. By a similar calculation, the sound speed inverse error for MSDs is on the order of 0.045 m/s to 0.18 m/s.

The previous chapters showed that at 400 km, coupling effects dominate the mode arrival and cause significant amounts of multipath. Figure 5.16 shows the performance of the MSDs at 400 km. The magnitude of the travel time error is and the variance is twice that at 250 km. The MSDs, peak picking and the quiescent detector have almost the same amount of mean error and variance. The previous chapters showed that at T400, the mean spectrum for modes 1 and 2 have the minimum amount of fading. Modes 1 and 2 hence have the lowest error and the lowest variance. The mean estimation error varies between 10 ms for modes 1 and 2 to 25 ms for the higher modes. By Equation 5.14 at 400 km for a value of  $T = 270$  s the mean sound speed error varies from .05 m/s to 0.13 m/s.

## 5.4 Discussion and conclusions

This chapter considered various travel time estimation methods and analyzed their error performance. In the absence of internal wave effects or no knowledge of internal wave statistics, the quiescent detector is preferable to peak picking. In the presence of internal waves,

the quiescent detector is sub-optimal in terms of accommodating internal wave perturbations to the mode signal. When the propagating environment contains significant amount of internal waves, MSDs and peak picking are more preferable than the quiescent detector. At 50 km, MSDs are appropriate for travel time estimation. For ranges greater than 50 km, peak picking has a smaller travel time estimation error.

## Chapter 6: Mode Tomography

The last two chapters discussed the statistics of the LOAPEX signals and suggested MSDs to obtain travel time observables for up to 400 km. This chapter uses these ideas to implement mode tomography for LOAPEX signals measured at 50 km, 250 km and 500 km. The chapter is organized into three sections. Section 6.1 gives a background on mode tomography how the mode travel times can be inverted for the SSPs. Section 6.2 discusses how the mode tomography problem was set up for LOAPEX. Section 6.3 uses the MSDs described in Chapter 5 to make travel time estimates for the LOAPEX signals. The estimated travel times are then inverted for the SSPs at T50, T250 and T500. Section 6.4 concludes this chapter.

### 6.1 Mode tomography

Tomography uses both ray based and mode based approaches. Ray tomography has been widely used. Munk and Wunsch used a geometric optics approach to show that the perturbations in the travel times of the different rays can be used to measure perturbations in sound speed [48]. Worcester implemented the first tomography experiment using reciprocal travel time measurements across 25 km path in the Pacific Ocean [49]. The Mid-Ocean Dynamics (MODE) group showed that most of the energy in the ocean was concentrated around mesoscale phenomenon [50] which, as mentioned in the previous chapters is spread across hundreds of kilometers. Motivated by the study performed by the MODE group, and Munk and Wunsch's study in [48], Cornuelle [51] performed ray tomographic inversions around 300 km x 300 km area. In 1981, the Ocean tomography group deployed acoustic receivers at ranges of 1000 km to 2000 km in Gulf Stream. The travel time changes were useful to track the seasonal changes and the meandering of the Gulf Stream [52]. Other

than these experiments, ray based tomography has been widely applied. See the book by Munk et al. for a complete list of tomography experiments [1].

For modes, Munk and Wunsch propose a perturbation based inverse where the perturbation in narrowband mode travel time is inverted for perturbation in sound speed [15]. The following equation assumes the sound speed perturbation  $\Delta c(i)$  is constant in each layer (i) and uses a perturbation theory approach to express the narrowband mode travel time perturbation as a weighted sum of the sound speed perturbations across layers (i.e),

$$\Delta\tau_m = \sum_i \chi_m(i) \Delta c(i) \quad (6.1)$$

where the weights  $\chi_m$  for each mode are given by a perturbation expansion of the modal group velocity with respect to sound speed perturbation. The weights  $\chi_m$  for mode  $m$  are given by,

$$\chi_m(i) = \frac{1}{k_m^0} \underbrace{\left[ (2\omega_0 - \frac{c_m^0}{v_{g,m}^0} \omega_0) |\psi_m^0(i)|^2 + \omega_0^2 \frac{\partial}{\partial \omega} |\psi_m^0(i)|^2 \right]}_{\omega_0} \frac{\Delta z_i}{c_0^3(i)} \quad (6.2)$$

where,

$c_0(z)$  = Reference sound speed

$k_m^0$  = Modal phase velocity

$v_{g,m}^0$  = Modal group velocity

The subscript '0' denotes that all the quantities are measured with respect to the reference sound speed profile. Note that because of the narrowband nature of Equation 6.1, the modeshapes, group velocities and phase velocities are defined with respect to the frequency  $\omega_0$ . The travel time perturbations of the different modes can be arranged as a column vector, thus Equation 6.1 can be written in matrix form

$$\Delta\tau = \chi\Delta\mathbf{c} \quad (6.3)$$

where the columns of the matrix  $\chi$  contain the sensitivity functions of the different modes arranged as column vectors and the vector  $\Delta\mathbf{c}$  is a column vector that contains the sound speed perturbations across multiple layers. The least squares inverse for the sound speed is given by

$$\widehat{\Delta\mathbf{c}} = (\chi^H\chi)^{-1}\chi^H\Delta\tau \quad (6.4)$$

Mode travel times can thus be inverted for the sound speed perturbations across the propagation path. Building on Munk and Wunsch's work [15], Romm discussed the framework for mode tomography by discussing how perturbations in mode group velocity can be used to invert for the sound speed perturbations [53]. Romm's simulation examples [53] (modeled on the Greenland Sea experiment [21]) showed that mode tomography could be used to measure sound speed perturbations in the top 500 m of the water column. Using simulations Shang showed that for a the perturbation in mode travel times can be used to measure the range and depth scale of an eddy [16]. Regarding experimental results, the mode tomography for the Greenland Sea experiment [21] is the only case. During the Greenland Sea experiment 6 hydrophones spanning depths of 100 m to 200 m recorded 250 Hz broadband acoustic signals across a 106 km path. The group velocities of the first 6 modes along with the ray travel times were used to invert for the SSP across the propagation path. Incorporating the modal group velocities significantly improved the sound speed resolution in the near surface of the Greenland Sea.

In their development, Munk and Wunsch assume that the modes are the adiabatic invariants, implying that for slow range dependence, the modes do not undergo mode coupling [15]. Experiments such as ATOC and NPAL that were conducted later showed that modes undergo significant scattering at megameter ranges. Shang's simulations in [16] do not take into account internal waves. The Greenland Sea experiment was only over a range

of 106 km. At short ranges and high latitudes internal wave effects are not significant. The environment during the ATOC 1996, NPAL 1998 and the recent LOAPEX experiment is different in containing significant amount of internal waves. The LOAPEX signals in Chapter 4 and the simulations in Chapter 3 showed that internal waves induce travel time wander and perturbations to the mode amplitudes. This causes a challenge to mode tomography. Chapter 5 discussed MSD based travel time estimation methods to estimate the mode travel times and showed that the MSDs account for the internal wave induced source excitation perturbations and yield travel time estimates that are more accurate and have a less variance for up to range of 250 km. The MSDs thus provide a way to invert for the sound speed profile in spite of internal wave effects. The next two sections describe the following. Section 6.2 frames the mode tomography problem for LOAPEX. Following that, Section 6.3 uses MSDs and peak picking methods to estimate the SSP during LOAPEX.

## 6.2 Sound speed inverse in the LOAPEX environment

The LS inverse in the form expressed in Equation 6.4 is restrictive in several ways. First, the sound speed perturbation is assumed constant across each layer, which gives the resulting perturbation inverse a blocky appearance. Second, for a well conditioned inverse problem the number of layers must be less than the number of modes. This limits the number of layers that can be used in the inversion. References [51], [54], [21], [53] avoid these problems by expressing the sound speed perturbations as a weighted sum of depth dependent basis functions such that,

$$\Delta c(z) = \sum_m U_m(z) b_m \quad (6.5)$$

Writing Equation 6.5 in matrix form,

$$\mathbf{\Delta}c(z) = \mathbf{U}b \quad (6.6)$$

By equations 6.6, 6.5 and 6.4, the estimated coefficients are,

$$\hat{\mathbf{b}} = (\chi\mathbf{U})^{\mathbf{H}}(\chi\mathbf{U})^{-1}(\chi\mathbf{U})^{\mathbf{H}}\Delta\tau_{\mathbf{m}} \quad (6.7)$$

The sound speed inverse interpolated via the basis functions is given by,

$$\widehat{\Delta c(z)} = \mathbf{U}\hat{\mathbf{b}} \quad (6.8)$$

The sound speed inverse via Equation 6.8 has the following advantages over implementing it using Equation 6.4. The SSP inverse using Equation 6.4 assumes that the sound speed is constant across each layer, which causes the inverse sound speed to look blocky. Using basis functions on the other hand, offers a smooth basis set to avoid the blockiness via Equation 6.4. Second, the basis functions lead to a reduction in dimension and hence instead of inverting for the perturbations across many layers only a few coefficients need to be estimated. This leads to a better conditioned inverse. Finally, a basis that incorporates a-priori knowledge of the statistics of the sound speed perturbations across the multiple layers restricts the inverse to be more in line with the oceanographic data and thus more accurate. There have been different types of basis functions used so far. Cornuelle suggests geostrophic modes [51] to interpolate the sound speed perturbations across depth. Howe uses a basis function set that consists of the geostrophic functions augmented with additional basis functions that account for various uncertainties [54]. Sutton [21] and Romm [53] use archival CTD profiles to estimate an EOF basis function set for the sound speed perturbations.

The LOAPEX array can adequately resolve only acoustic modes 1 to 10. This chapter uses travel times of LOAPEX modes 1 to 10 and the EOF method defined by Equations 6.7 and 6.8 to estimate the SSP perturbations. Mode tomography via Equations 6.7 and 6.8 first requires a reference profile that does not differ much from the perturbed profiles. For LOAPEX, the reference SSP and the SSP perturbations were estimated from in situ measurements made at the VLA. Sensors clamped to the VLA made continuous environmental

measurements (temperature and salinity) and these in situ measurements provide a reference profile and a basis function set that describes the sound speed perturbations. The sensors were made by a company called Seabird, thus they are referred to as “Seabird measurements” [55,56]. Temperature and salinity measurements were made every 5-7 minutes for the duration of the LOAPEX experiment. The SSPs estimated at the LOAPEX VLA for yeardays 160 to 400 were averaged to obtain a mean SSP for the LOAPEX environment. The mean SSP will be the reference profile  $c_0(z)$ . The modeshapes were calculated for the reference SSP and the sensitivity matrix estimated via Equation 6.2. Figure 6.1 shows the modeshapes and the sensitivity matrix for the reference profile. Mode 10 has an upper and lower turning depths of 350 m and 1600 m, respectively. The columns of the sensitivity matrix span the depth spread of the modeshapes. The sensitivity of the higher modes increases in depth and detail with mode number.

The next requirement is to obtain a suitable basis set that describes the sound speed perturbations about the reference SSP. The sound speed perturbations about the reference SSP measured at the VLA provide a data set to estimate the perturbation statistics and estimate a basis set. Because modes 1 to 10 span depths of only 350 m to 1600 m, the sound speed perturbations will be estimated only between those depths. The sound speed perturbations must be pre-processed before estimating the statistics. Figure 6.2 shows the perturbations of the SSPs about the mean SSP. The sound speed perturbations in Figure 6.2 vary between + 3 m/s to -3 m/s. The sound speed perturbations are presumably due to internal waves and mesoscale effects. The two phenomena differ from each other in their time and range scales. While the mesoscale variations span larger distances and have time scales of 30-40 days [1,4] the internal wave variations are correlated across tens of kilometers and have high frequency variations on the order of greater than a day [13,14]. The objective here is to suppress the sound speed perturbations induced by internal waves and invert for possible mesoscale events. While calculating the basis function, the sound speed perturbations due to internal waves must be mitigated. To isolate the different types of sound speed perturbations, the data displayed in Figure 6.2 was processed using a high

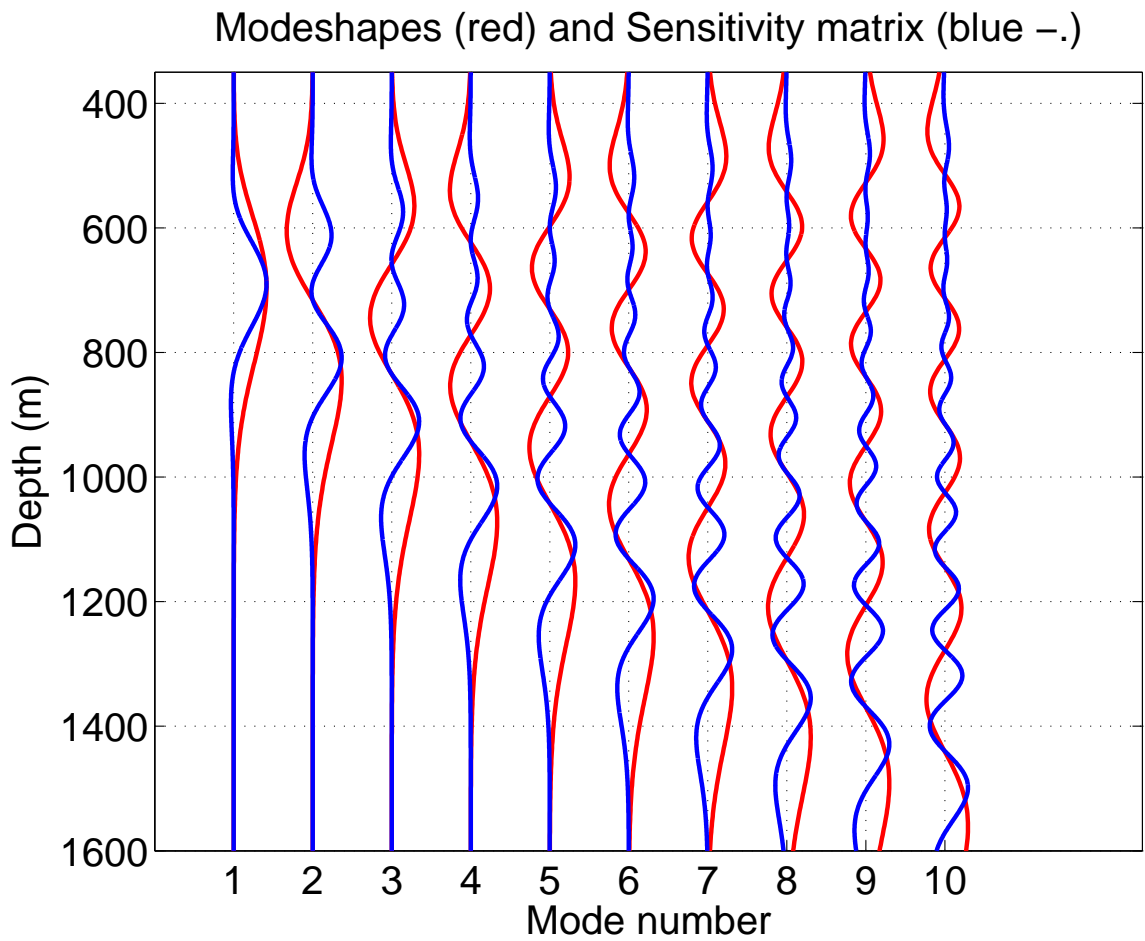


Figure 6.1: The modeshapes (red) and the sensitivity matrix (blue -.) for the mean Seabird profile. The depth resolution of the different columns is roughly proportional to the span of each mode. The higher modes span greater depths and offer more resolution across depth.

pass filter and a low pass filter. First, a high pass filter with cutoff frequencies above one cycle per day filtered the perturbations to isolate the internal wave induced perturbations. Figure 6.3 gives an idea of the magnitude of the high pass variations. The data has a zero mean and a maximum standard deviation of 0.1 m/s. The maximum and minimum variations around the axis lie between  $\pm 0.25$  m/s and increase to  $\pm 0.5$  m/s at shallower depths. In order to obtain the slow variations of the SSP, the seabird measurements were used to perform one day averages. Figure 6.4 shows the one day averages. The low pass filtered sound speed perturbations show some patterns that are consistent for days. For instance, between yeardays 210 to 240, there is an obvious sound speed perturbation between 600 m and 800 m. On the other hand, between 160 to 200, the sound speed perturbations are high between 350 m to 600 m. In order to obtain a suitable independent realizations of the sound speed variations were obtained by averaging the low pass sound speed perturbations every 10 days. An SVD analysis of the sound speed perturbations of the ten day averages yielded an EOF basis set that described the larger time scale variations at the array. The analysis showed that the first 3 EOFs constituted more than 99 % of the variance in the sound speed perturbations. The 3 EOFs are shown in Figure 6.5.

### 6.3 Mode tomography for LOAPEX

Apart from the SSPs measured at the array, LOAPEX had CTD measurements that were made at T50, T250 and T500 just before the transmissions at the respective stations. The SSP measurements at the array and the transmitting stations are a cross check to verify if the tomographic inverse is within the range of sound speed variations in the LOAPEX environment.

Before comparing the tomographic inverse with the point measurements at different stations, also note the fundamental differences between the two sound speed profiles. The received signals at each station propagate across tens to hundreds of kilometers through different sound speed profiles. The mean travel times of the modes are better described by the range averaged sound speed profile. The tomographic inverse should yield a sound

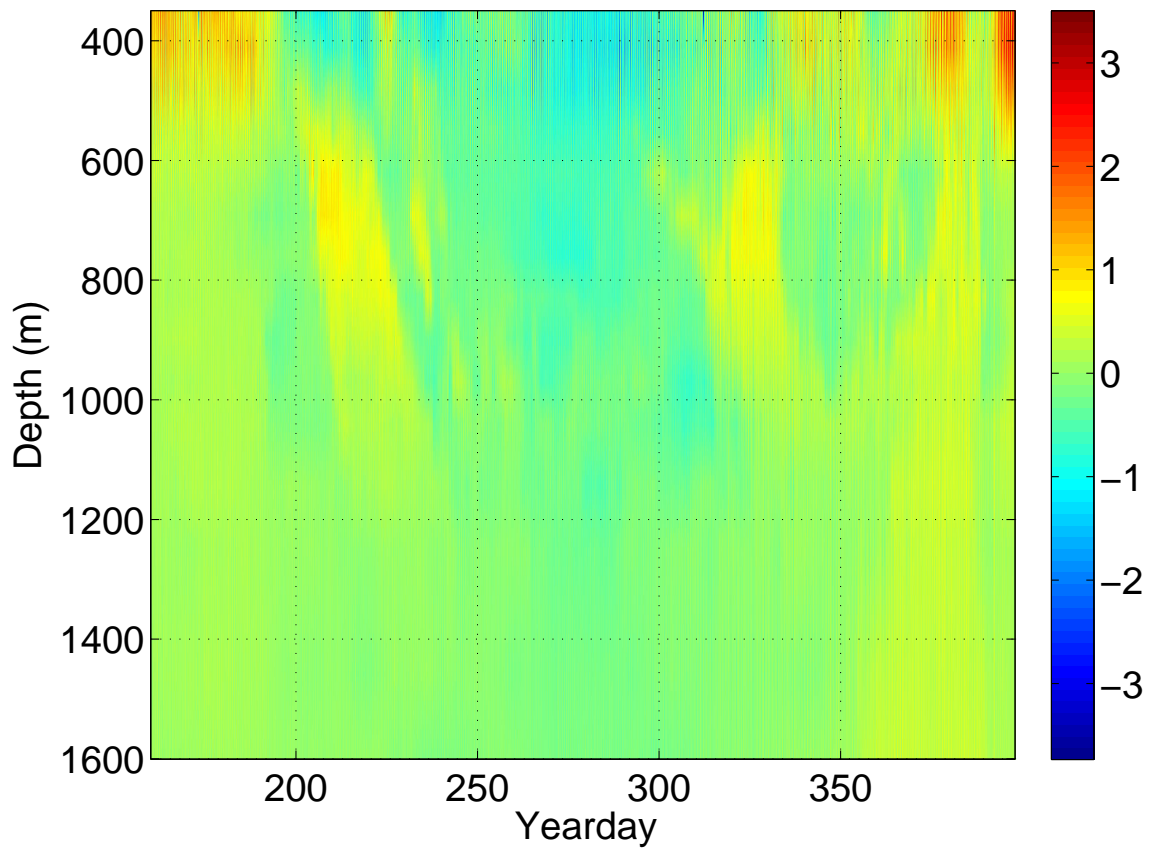


Figure 6.2: Sound speed perturbations (m/s) (with respect to the time averaged mean SSP) at the VLA. The perturbations vary between  $\pm 3$  m/s.

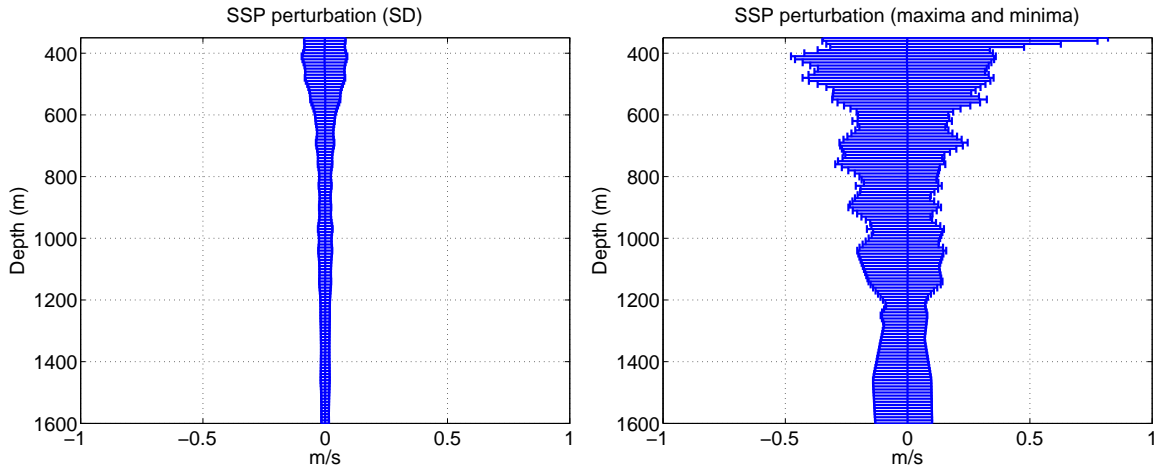


Figure 6.3: Statistics of the high pass filtered sound speed perturbations (with respect to the time averaged mean SSP). The standard deviation (left subplot) is around .1 m/s. The maximum and minimum of the sound speed perturbations (right subplot) vary with depth. Around the axis between 600 m to 1000 m, the maximum perturbations are on the order of  $\pm .25$  m/s, whereas at shallower depths around 350 m, the sound speed perturbations can go up to .5 m/s.

speed profile that is closer to the range averaged profile. Also note that the depth extent and detail of the sound speed inverse are governed by the sensitivity matrix in Figure 6.1. Modes 1 to 10 are affected only the sound speed perturbations between 350 m to 1600 m and hence can yield a sound speed inverse spanning those depths. The sensitivity matrix and the reference sound speed profile substituted in Equation 6.7, 6.8 to estimate the SSPs across the different LOAPEX paths. The rest of this section discusses the results of the tomographic inverses at T50, T250 and T500.

Figure 6.6 shows the travel time estimates produced via peak picking, 1 D MSD and 2 D MSD and compares them with the travel times predicted by the SSP measured at the array and the CTD measurement at T50. For modes such as 6, 7, 9 and 10, the 1 D MSD and peak picking have a greater time variance than the 2 D MSD. This is due to the 1 D MSD and peak picking not accounting for the nulls in the mode spectrum. The LOAPEX source is skewed towards frequencies lower than 75 Hz. The mean peak of the LOAPEX modes hence occurs at an earlier time than the time of arrival of the 75 Hz frequency. The most important thing to note from Figure 6.6 is that the travel time estimates of all three

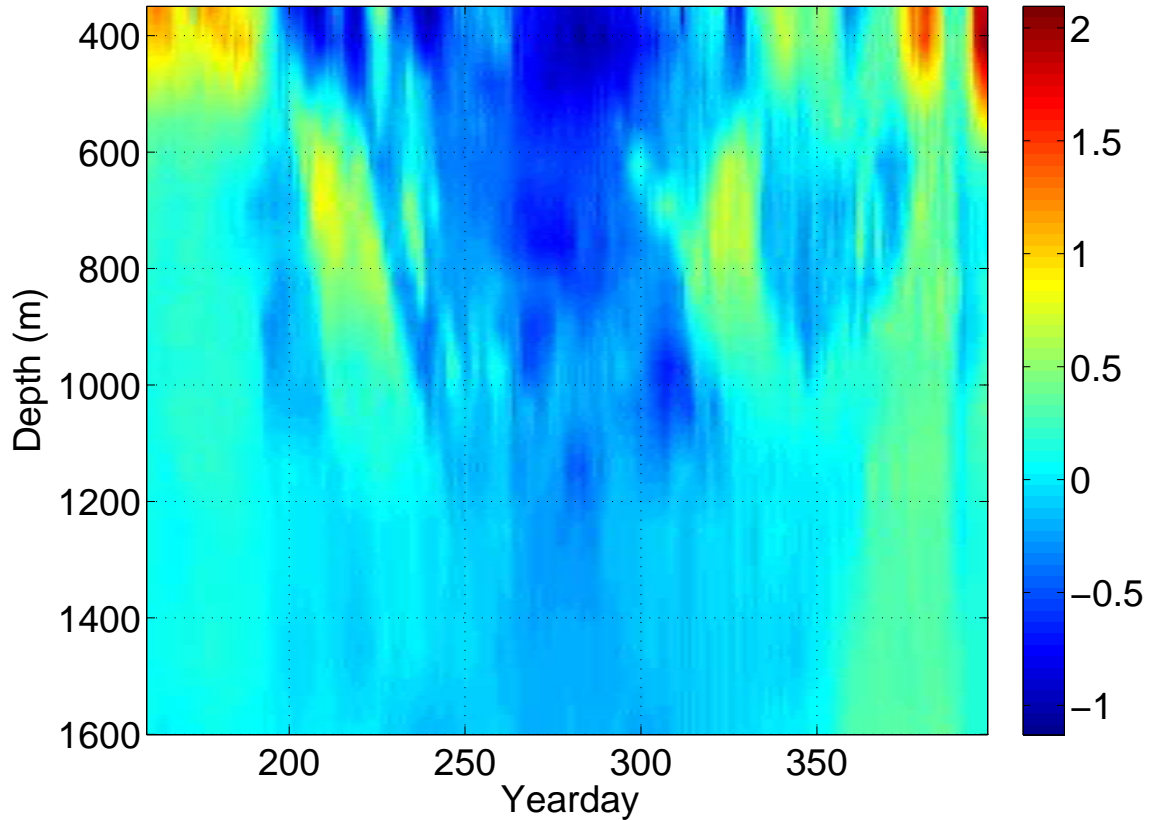


Figure 6.4: One day averages of the sound speed perturbations in m/s (with respect to the time averaged mean SSP) at the VLA. The one day averages of the sound speed perturbations are larger than the magnitudes of the high pass filtered sound speed perturbations in Figure 6.3. The one day averages of the sound speed perturbations vary between -1 m/s and +2 m/s.

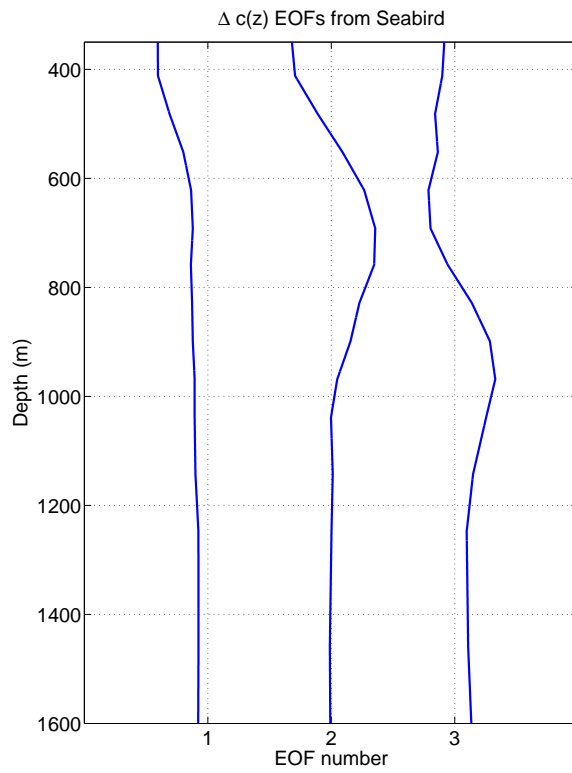


Figure 6.5: EOFs 1 to 3 estimated from the sound speed perturbations at the VLA. The plotted EOFs make up for more than 99 % of the energy in the sound speed perturbations.

methods are closer to the Seabird predictions than the CTD.

The sensitivity matrix in Figure 6.1, the travel time estimates in Figure 6.6 were substituted in Equation 6.7 and 6.8 to obtain the sound speed inverse. Figure 6.7 shows the Seabird SSP at the array, the CTD SSP at the source and the inverted SSPs. For a range separation of only 50 km, the SSPs at the array and the source are remarkably different. The perturbations at the source are similar in magnitude and depth scale to the mesoscale perturbations shown in Figure 6.4 recorded by the VLA between yeardays 210 to 240. The sound speed inverse shows greater variations for the 1 D MSD and peak picking show greater variance than the 2 D MSD. This can be related to the travel time estimates in Figure 6.6 which showed that the 1 D MSD and the peak picking had a greater variance.

The sound speed perturbations measured at the array and the transmitting station at T50 significantly differ from each other and seem to suggest that there was a significant mesoscale perturbation in the environment. The sound speed inverse is closer to the Seabird profile which suggests that the LOAPEX signals for the most part propagated in an environment where the environment resembled the environment at the array. This suggests that going East from the source towards the VLA, there are significant changes in the environment. The previous paragraph observed that the sound speed perturbation at the source is similar to a mesoscale perturbation. Mesoscale effects are spread over tens to hundreds of kilometers. The mesoscale perturbation at the source should hence be constant across a large distance. Given the conjecture from the sound speed profiles, that the environment to the east of the source is much different from the environment at the source, it is plausible that the T50 source is on the periphery of a mesoscale feature.

Moving on to station T250, Figure 6.8 shows that there is not much of a difference between the travel time estimation curves for the three different methods. The travel times of the LOAPEX modes differ much from the predictions made using the SSP measured at the array because the modes propagate for most of the distance between T50 and T250. The travel time estimates produced by the three methods for modes 1 to 5 lie between the predictions made using the T50 and T250 profile which suggests that there is a significant

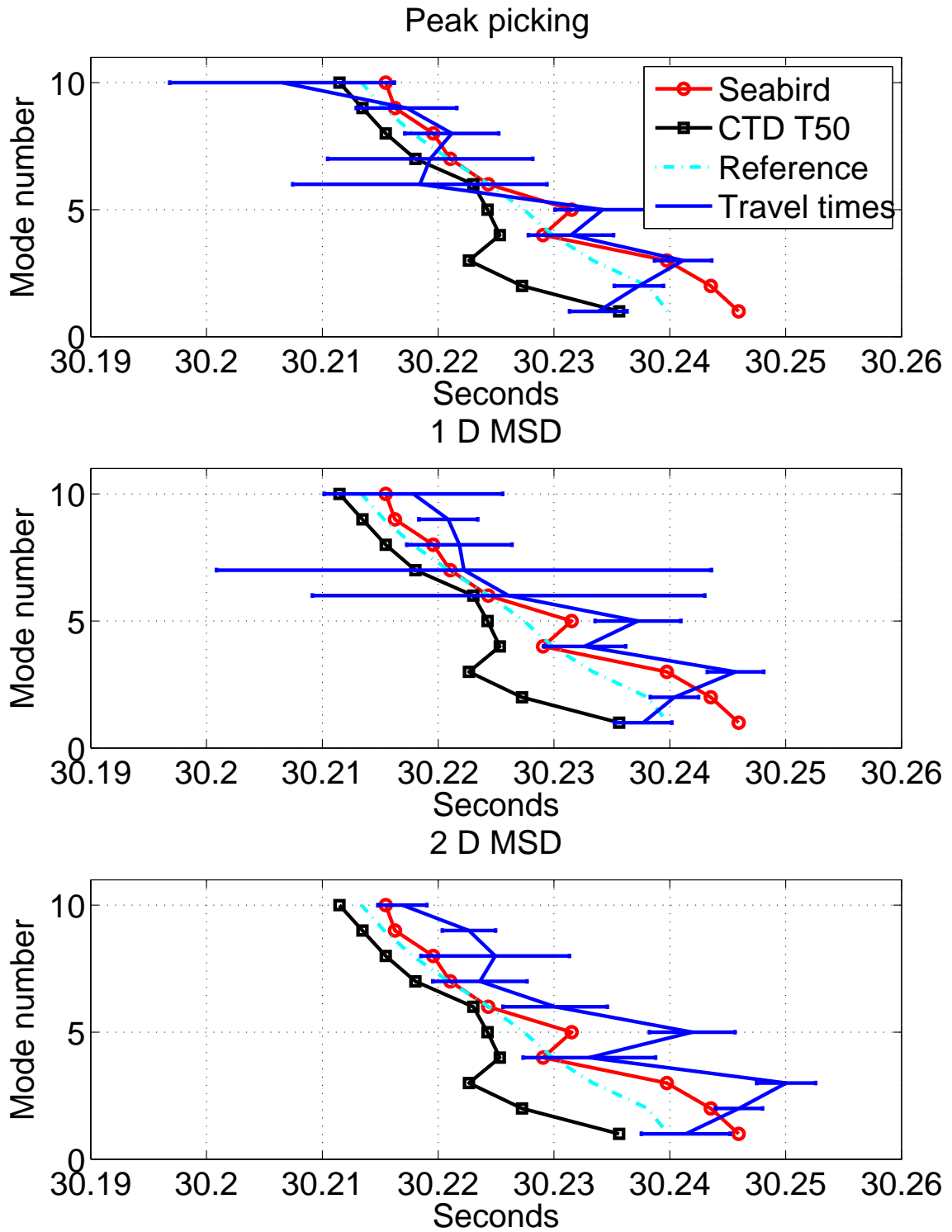


Figure 6.6: Travel time estimates at T50. The errorbars indicate the standard deviation of the estimates. The travel time estimates are closer to the Seabird SSP measured at the array than the CTD profile measured at the source. The 2 D MSD yields a less travel time variance.

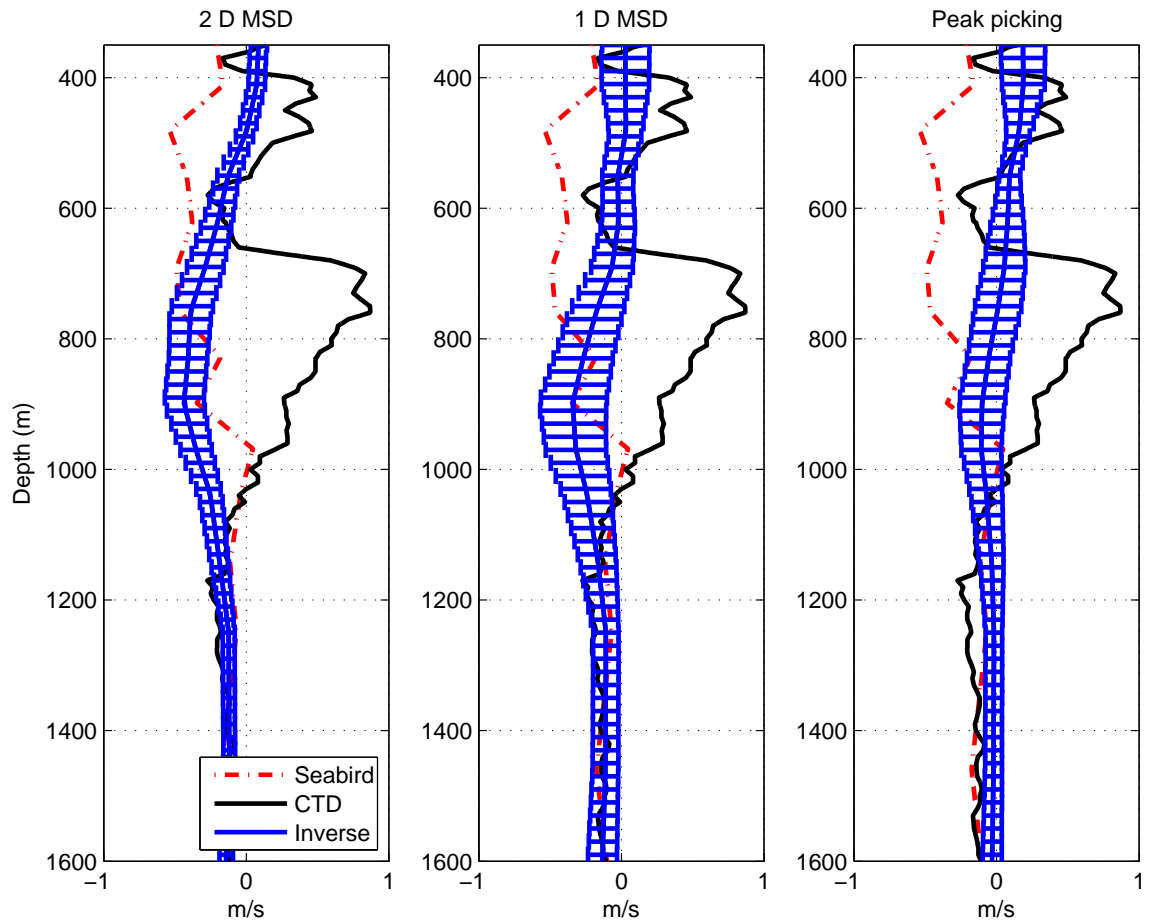


Figure 6.7: Sound speed perturbations inverse at T50. The inverted SSP is closer to the Seabird SSP. The errorbars of the sound speed inverses show that the inverse obtained by using the 2 D MSD has a lower variance.

difference in the axial sound speeds measured between T50 and T250. For modes greater than 5 the errorbars for travel times lie close to the T250 CTD.

Figure 6.9 shows the sound speed inverse at T250. The sound speed inverse produced by the three methods varies significantly from the SSP measured at the array. The estimated inverse is close to the average of the T50 and T250 profile. There are two observations to make here. First, the significant difference between the SSP inverse at T50 and T250 lend more credence to the earlier conjecture that T50 is on the edge of a significant mesoscale perturbation. Second, the 2 D MSD again yields a lower variance in the sound speed inverse.

Figure 6.10 compares the peak picking statistics to travel times predicted by CTD profiles measured at the array, T50, T250, T500 and the reference profile. The LOAPEX travel times are closer to the travel times predicted by the reference SSP than any other SSPs. Modes 1 to 3 show less travel time variance than the other modes. At T500 there is much cross-modal coupling that the MSDs constructed using the statistics of the source excitation spectrum are not an effective method. Peak picking was hence used to estimate the travel times of the modes. Two types of tomographic inversions were considered. The first inverse consisted of only modes 1 to 3 and the second inverse consisted of using modes 1 to 10. Figure 6.11 shows the results for both the types of inversions. In general, the SSP inverse has a much higher variance than at T50 and T250. Using only modes 1 to 3, decreases the variance of the sound speed inverse, but causes poor inversion results for depth above 500 m. The much higher sound speed variance is due to the multipath scattering. For the sake of clarity, Figure 6.12 shows only the mean of the sound speed inverse. The mean of the sound speed inverse is close to the mean sound speed profile obtained by averaging the CTD measurements up to T500 and the Seabird measurements at the array. This agrees with the intuition that the modes propagating across the T500 path effectively travel through the range averaged SSP. At T500, in spite of multipath scattering, the mean of the mode travel times can still be exploited for tomographic inversions.

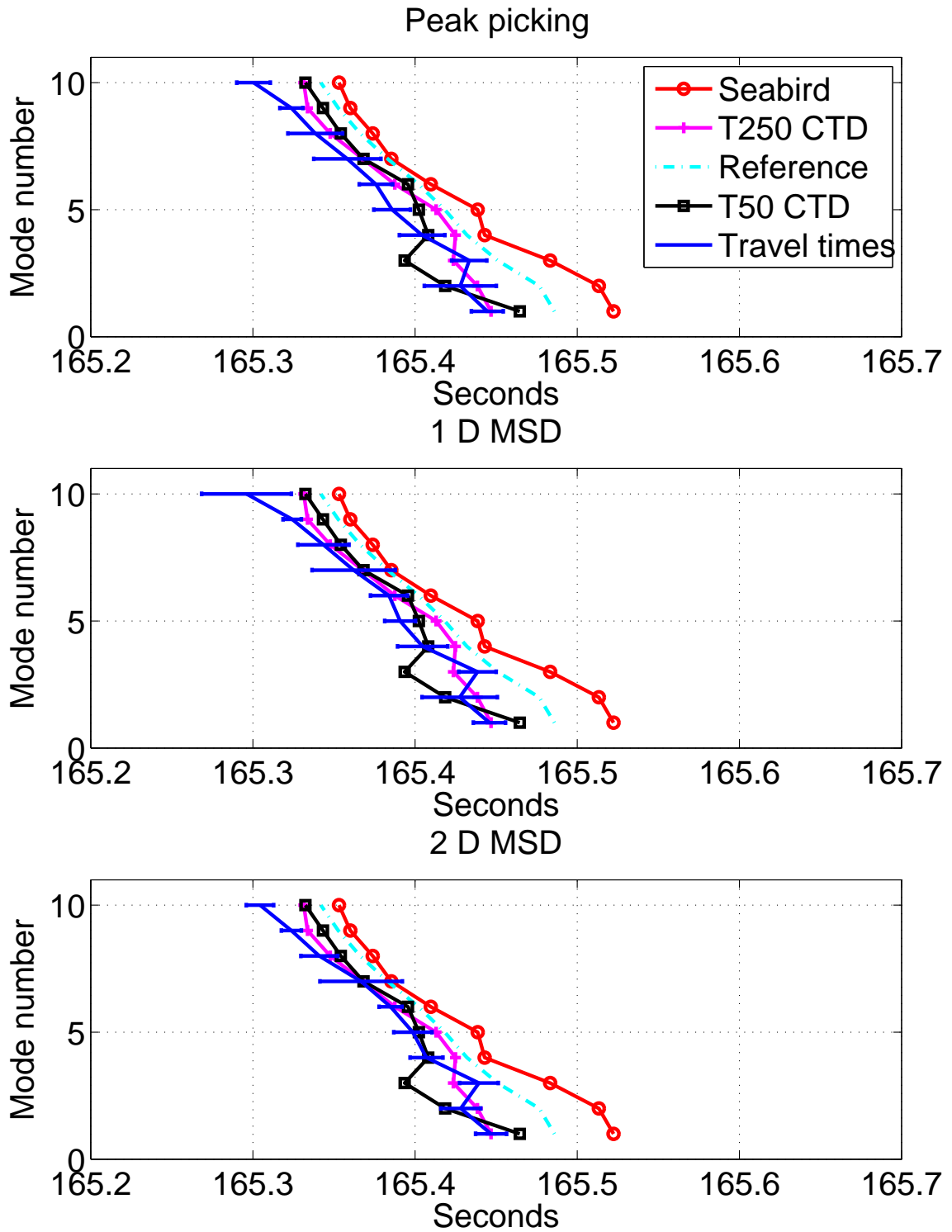


Figure 6.8: Travel time estimates at T250. The errorbars indicate the standard deviation of the estimates. The travel time estimates for the three different methods all lie close to the travel times predicted by the profiles at T50 and T250. Similar to T50, the MSD travel times have a less variance.

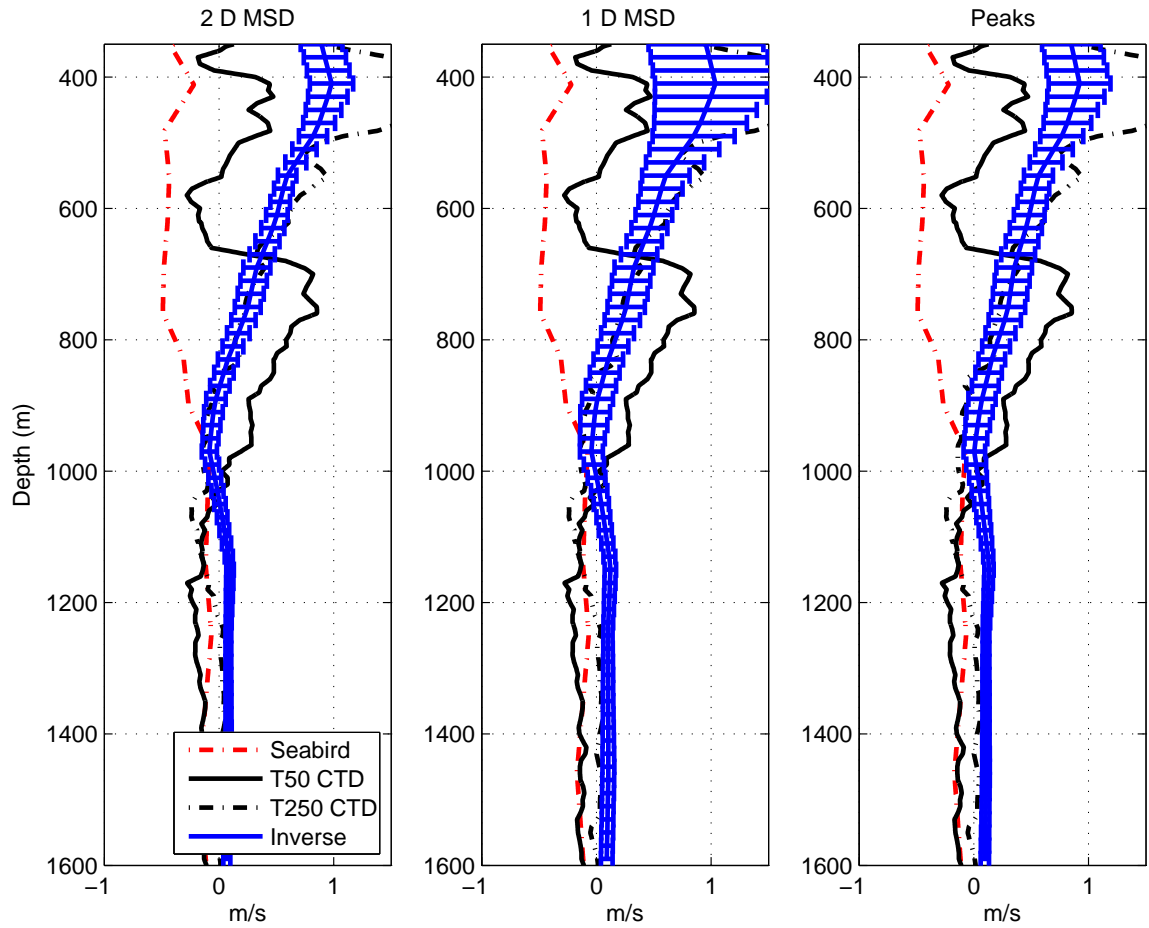


Figure 6.9: Tomographic inverse at T250. The inverse sound speed profile is close to the CTD profile at T250. The errorbars of the sound speed inverses show that the inverse obtained by using the 2 D MSD has a lower variance.

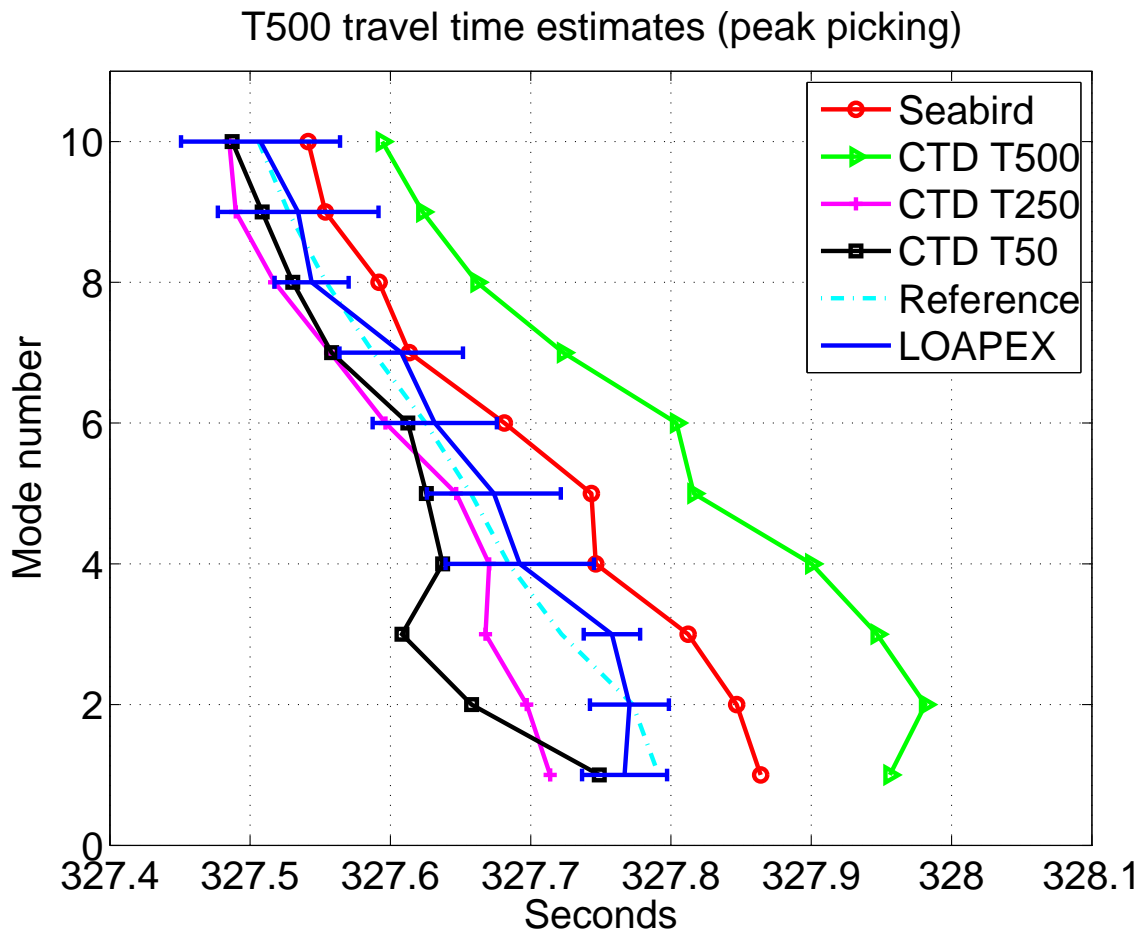


Figure 6.10: Travel time estimates at T500 (via peak picking). The errorbars indicate the standard deviation of the estimates. The LOAPEX mode travel times are closer to the travel times predicted by the mean SSP than any of the other spot measurements.

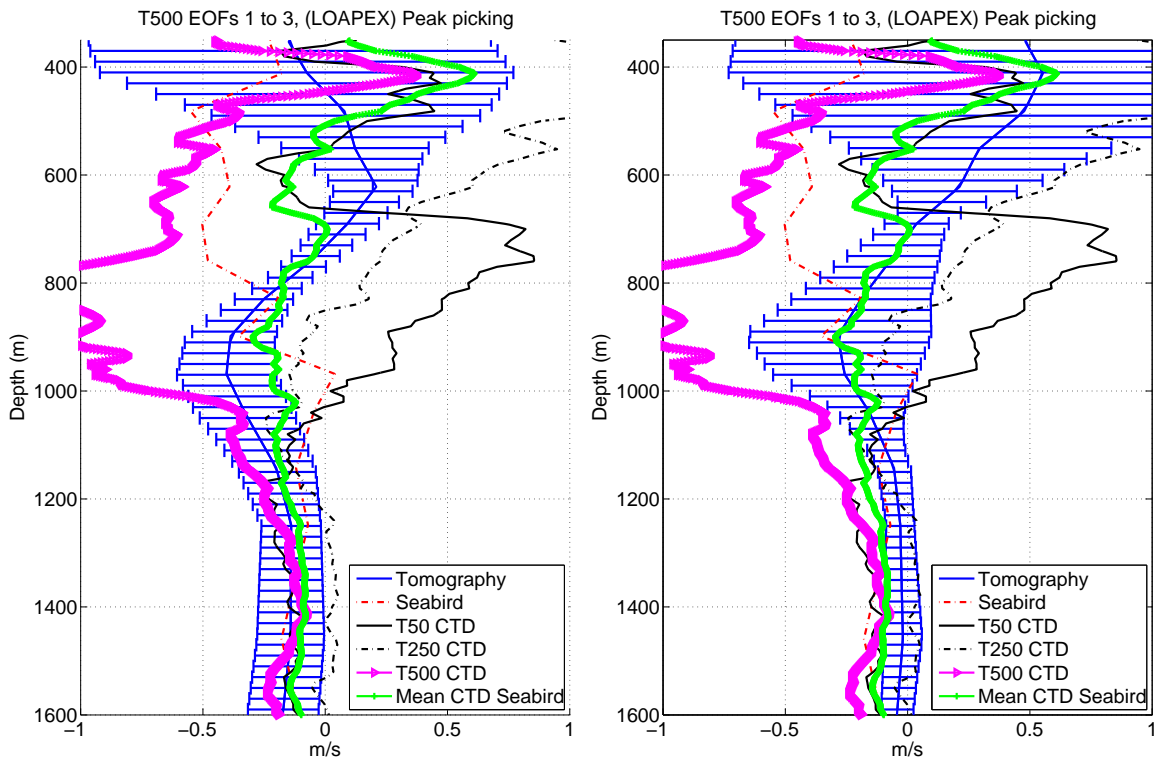


Figure 6.11: Sound speed inversion results at T500 using modes 1 to 3 (left plot) and using modes 1 to 10 (right plot). The SSP inversion results have a much higher variance than at T50 and T250. Using only modes 1 to 3, decreases the variance of the sound speed inverse, however causing poor inversion results for depth above 500 m.

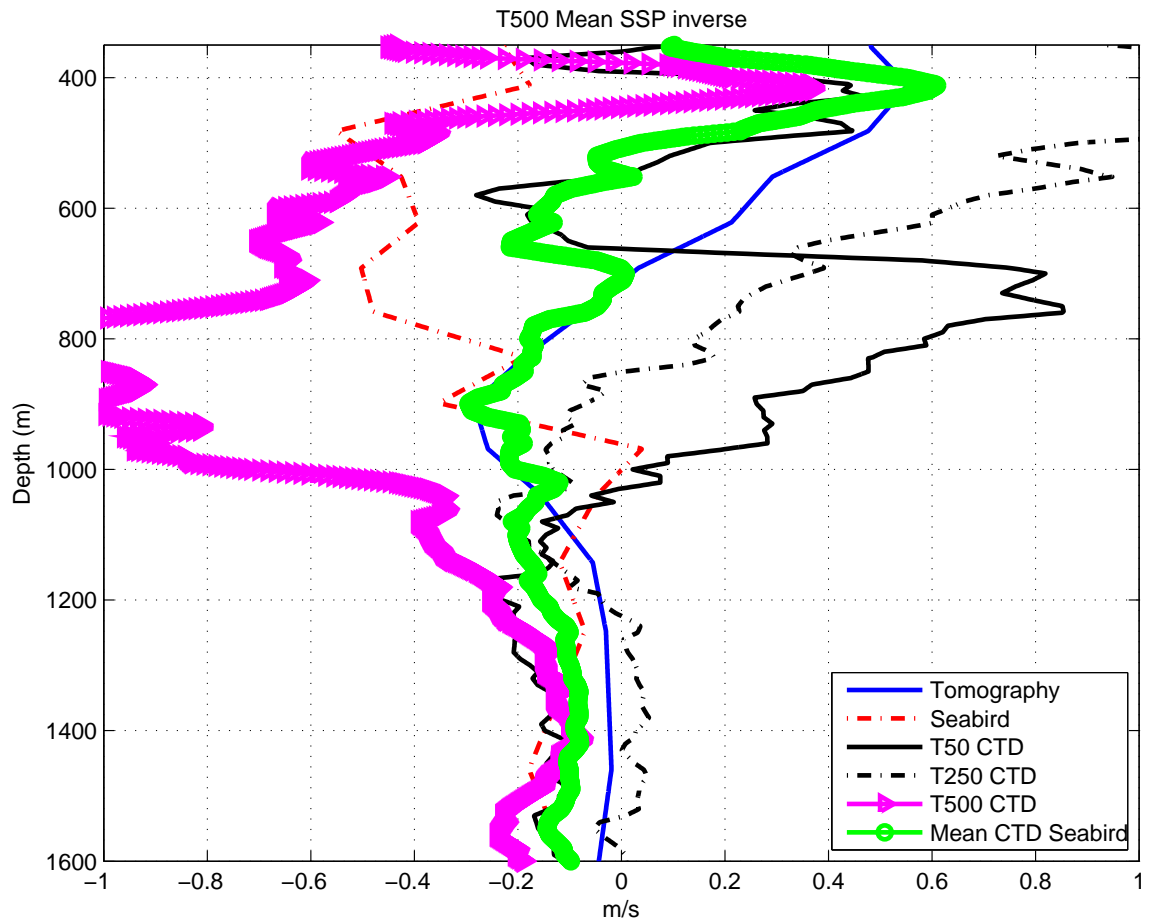


Figure 6.12: Mean sound speed inverse at T500 using modes 1 to 10. The mean of the sound speed inverse is close to the mean SSP obtained by averaging the SSPs measured across the T500 path.

## 6.4 Conclusions

The most significant contribution of this chapter is performing mode tomography in the presence of significant internal wave effects. The MSDs were useful to provide sound speed inverses that had less variance than peak picking. The SSP inverse via the MSDs were also consistent with sound speed perturbations measured across the LOAPEX area. The mode tomography results presented in this chapter for ranges of up to 500 km have shown that mode tomography can measure mesoscale effects across hundreds of kilometers.

Although the MSDs were useful in making travel time measurements and reducing the sound speed perturbations, there is still a significant travel time wander due to internal waves. Averaging travel times over a day suppresses internal wave induced time wander [57]. None of the LOAPEX transmissions from T50 to T500 lasted for a day. Having a greater number of transmissions lasting for more than a day should have yielded more accurate tomographic inverse and more insights into the background SSP. Future experiments should make provisions for having more number of transmissions.

## Chapter 7: Conclusions and Future Directions

This chapter concludes the thesis by summarizing the important points and suggesting future directions for research. Section 7.1 highlights the conclusions of each chapter and discusses their impact on current and future work in ocean acoustics. Section 7.2 describes the significant future directions that could build on the work presented in this thesis.

### 7.1 Conclusions

The first contribution of this thesis is the body of simulation work modeling broadband and narrowband mode statistics at short ranges. As mentioned in Chapter 3, there is significant literature on the mode coupling at megameter ranges [5, 6, 24, 58], but very little at short ranges. By focusing on mode statistics at distances on the order of hundreds of kilometers, Chapter 3 is a valuable addition to the coupled mode literature. Based on the simulations, the important conclusion was that mode scattering across range occurs in three different stages. During the first stage, there is no mode coupling, but the internal waves induce significant perturbations to the amplitude and phase of the mode time series. In the second stage, coupling effects start causing multipath. During the third phase, coupling effects dominate and the mode arrivals contain significant multipath. Apart from providing a better understanding of mode propagation, the mode statistics have applications in planning tomography experiments. The time coherence plots determine how long it would take for mode signals to decorrelate. This should help plan the time spacing of transmissions. In tomography it is crucial to make accurate travel time measurements. While estimating the mode travel times, the internal-wave-induced time wander is equivalent to a background noise. The statistics for the travel time variance in Chapter 3 quantify the travel time noise due to internal waves.

The second major contribution of this thesis is the analysis of the LOAPEX mode signals. Chapter 4 noted the challenges in processing the LOAPEX receptions and described how they were overcome. The LOAPEX mode statistics agreed with the simulations, indicating that the proposed model for mode scattering in Chapter 3 is correct. Although LOAPEX was a unique experiment in its conduct and scope, very little has been published on the analysis of the LOAPEX signals. One reason for this is the difficulty of implementing the mooring and source delay corrections for the LOAPEX data set. The solution to these problems presented in Chapter 4 will facilitate future analysis of the LOAPEX receptions. Udovydchenkov used theoretical analysis and simulations to predict modal time spreads [25]. The LOAPEX mode statistics in Chapter 4 should serve as a cross-check for the results in [25]. LOAPEX also contained transmissions made from a shallow source placed at 350 m. The receptions from the shallow source could provide new insights on sound scattering into the axis. The mode amplitudes from the shallow source are at a low SNR and require averaging across multiple receptions. The lack of mooring data for the whole array has prevented any coherent averaging on the shallow receptions. The mooring estimates from Chapter 4 provide mooring data for the whole array and can be used to compensate for the array motion. The motion compensated signals can then be averaged to increase the SNR of the shallow source receptions.

The third contribution of this thesis is with regard to signal processing. The simulations and the LOAPEX analysis highlighted the need for signal processing techniques to make accurate travel time estimates for modes perturbed by internal waves. Chapter 5 constructed MSDs based on the source amplitude statistics to make optimal travel time estimates for modes at short ranges. For simulated mode signals, the MSDs demonstrated travel time estimates that had less variance for up to the second scattering regime.

Another important contribution of this thesis is the implementation of mode tomography on LOAPEX signals. The tomographic scheme in Chapter 6 used the travel time estimates obtained via MSDs to obtain sound speed inverse across the LOAPEX path for T50 and T250. Although there were significant internal wave effects, the tomographic inverse yielded

SSPs that were consistent with measurements around the LOAPEX area. Chapter 1 noted that mode tomography has the potential to track mesoscale phenomena. The tomography methods in Chapter 6 should motivate future tomographic experiments aimed at measuring mesoscale phenomena.

## 7.2 Future directions

There are two significant research directions that can be based on this thesis. Regarding the first direction, there is the question of what are the tomographic observables beyond 400-500 km. The PE simulations in Chapter 3 and the travel time estimation methods in Chapter 5 showed that beyond 400 km, the coupling of the axial energy would be so great as to make the available travel time estimation methods useless. To invert for sound speed perturbations near the axis, an alternative is to use parts of the axial field that are more robust with respect to scattering. It is beyond the scope of this thesis to suggest the appropriate tomographic observables beyond 400-500 km. To decide on the appropriate tomographic observables two things are required. The first step is to undertake a simulation study similar to Chapter 3 for ranges beyond 400 km. The second step is to estimate the statistics of the axial arrivals and use that information to decide on the appropriate observables.

The second research direction is on implementing tomography using the material in this thesis. The travel time estimates provide by the MSDs could be used to implement internal wave tomography. At ranges on the order of 50 km, if there are no intervening mesoscale sound speed perturbations, the travel times of the modes would be affected only by internal waves. The MSDs can then be used to estimate the travel times and the statistics of the travel times inverted for parameters of the Garrett-Munk spectrum. The second type of tomographic inverse is to invert for the background SSP using the mode amplitudes. The conclusion that the mode amplitudes at short ranges, are mainly a function of the mode amplitudes at the source raises the possibility that the received mode amplitudes can be inverted for the mode amplitudes at the source. The source amplitudes can then be

substituted in Equation 2.2 to estimate the source SSP. A simpler type of inverse with mode amplitudes is to implement a perturbation based inverse. Tindle et al. gives equations for the perturbations in mode amplitudes for a perturbation in sound speed [59]. The perturbation in mode amplitudes with respect to a background mode amplitudes can hence be used to measure the perturbation in the sound speed.

## Bibliography

## Bibliography

- [1] W. Munk, P. Worcester, and C. Wunsch, *Ocean Acoustic Tomography*. Cambridge University Press, 1995.
- [2] S. Levitus, R. Burgett, and T. Boyer, *World Ocean Atlas 1994 Volume 3: Salinity*, 1994, NOAA Atlas NESDIS 3.
- [3] S. Levitus and T. Boyer, *World Ocean Atlas 1994 Volume 4: Temperature*, 1994, NOAA Atlas NESDIS 4.
- [4] G. L. Pickard and W. J. Emery, *Descriptive Physical Oceanography*, 5th ed. Pergamon Press, 1990.
- [5] L. Dozier and F. Tappert, “Statistics of normal mode amplitudes in a random ocean. 1. Theory,” *J. Acoust. Soc. Am.*, vol. 63, no. 2, pp. 353–365, February 1978.
- [6] —, “Statistics of normal mode amplitudes in a random ocean. 2. Computations,” *J. Acoust. Soc. Am.*, vol. 64, no. 2, pp. 533–547, August 1978.
- [7] L. Brekhovskikh and Y. P. Lysanov, *Fundamentals of Ocean Acoustics*. Springer-Verlag, 1991.
- [8] G. Frisk, *Ocean and Seabed Acoustics*. Englewood Cliffs, NJ: Prentice Hall, 1994.
- [9] F. B. Jensen, W. A. Kuperman, M. B. Porter, and H. Schmidt, *Computational Ocean Acoustics*. American Institute of Physics, 1994.
- [10] M. Collins, *User’s guide for RAM*, Naval Research Lab, Washington D.C.
- [11] M. B. Porter, *The Kraken Normal Mode Program*, SACLANT Undersea Research Centre, La Spezia, Italy.
- [12] J. A. Colosi and M. G. Brown, “Efficient numerical simulation of stochastic internal-wave-induced sound-speed perturbation fields,” *J. Acoust. Soc. Am.*, vol. 103, no. 4, pp. 2232–2235, April 1998.
- [13] C. Garrett and W. Munk, “Space-time scales of internal waves,” *J. Geophys. Res.*, vol. 3, pp. 225–264, 1972.
- [14] —, “Space-time scales of internal waves: a progress report,” *J. Geophys. Res.*, vol. 80, pp. 291–297, 1975.

- [15] W. Munk and C. Wunsch, "Ocean acoustic tomography : Rays and modes," *Reviews of Geophysics and Space Physics*, vol. 21, pp. 777–793, 1983.
- [16] E. Shang, "Ocean acoustic tomography based on adiabatic mode theory," *J. Acoust. Soc. Am.*, vol. 85, no. 4, pp. 1531–1537, April 1989.
- [17] G. V. Frisk, J. F. Lynch, and S. D. Rajan, "Determination of compressional wave speed profiles using modal inverse techniques in a range-dependent environment in nantucket sound," *J. Acoust. Soc. Am.*, vol. 86, pp. 1928–1939, 1989.
- [18] S. D. Rajan, J. F. Lynch, and G. V. Frisk, "Perturbative inversion methods for obtaining bottom geoacoustic parameters in shallow water," *J. Acoust. Soc. Am.*, vol. 82, pp. 998–1017, 1987.
- [19] J. F. Lynch, S. D. Rajan, and G. V. Frisk, "A comparison of broadband and narrow-band modal inversions for bottom geoacoustic properties at a site near corpus christi, texas," *J. Acoust. Soc. Am.*, vol. 86, pp. 1928–1939, 1991.
- [20] V. V. Goncharov and A. G. Voronovich, "An experiment on matched-field acoustic tomography with continuous wave signals in the Norway Sea," *J. Acoust. Soc. Am.*, vol. 93, no. 4, pp. 1873–1881, April 1993.
- [21] P. Sutton, W. Morawitz, B. Cornuelle, G. Masters, and P. Worcester, "Incorporation of acoustic normal mode data into tomographic inversions in the Greenland Sea," *Journal of Physical Oceanography*, vol. 99, pp. 12 487–12 502, June 1994.
- [22] P. F. Worcester and R. C. Spindel, "North Pacific Acoustic Laboratory," *J. Acoust. Soc. Am.*, vol. 117, no. 3, pp. 1499–1510, March 2005.
- [23] A. G. Voronovich, V. E. Ostashev, and the NPAL group, "Horizontal refraction of acoustic signals retrieved from the North Pacific Acoustic Laboratory billboard array data," *J. Acoust. Soc. Am.*, vol. 117, no. 3, pp. 1527–1537, March 2005.
- [24] J. A. Colosi and S. M. Flatte, "Mode coupling by internal waves for multimegahertz acoustic propagation in the ocean," *J. Acoust. Soc. Am.*, vol. 100, no. 6, pp. 3607 – 3620, December 1996.
- [25] I. A. Udovydchenkov and M. G. Brown, "Modal group time spreads in weakly range-dependent deep ocean environment," *J. Acoust. Soc. Am.*, vol. 123, no. 1, pp. 41–50, January 2008.
- [26] K. E. Wage, A. B. Baggeroer, and J. C. Preisig, "Modal analysis of broadband acoustic receptions at 3515-km range in the North Pacific using short-time Fourier techniques," *J. Acoust. Soc. Am.*, vol. 113, no. 2, pp. 801–817, February 2003.
- [27] K. E. Wage, "Broadband Modal Coherence and Beamforming at Megahertz Ranges," Ph.D. dissertation, MIT/WHOI, 2000.
- [28] K. E. Wage, M. A. Dzieciuch, P. F. Worcester, B. M. Howe, and J. A. Mercer, "Mode coherence at megahertz ranges in the North Pacific Ocean," *J. Acoust. Soc. Am.*, vol. 117, no. 3, pp. 1565–1581, March 2005.

- [29] A. B. Baggeroer and E. K. Scheer, "Modal leakage in range-dependent oceans," *The Journal of the Acoustical Society of America*, vol. 103, no. 5, pp. 2751–2751, 1998.
- [30] William H. Press and Brian P. Flannery and Saul A. Teukolsky and William T. Vetterling, *Numerical Recipes in C: The Art of Scientific Computing*, 1st ed. Cambridge University Press, 1992.
- [31] R. K. Andrew, private communication.
- [32] K. Aki and P. G. Richards, *Quantitative Seismology*. University Science Books, 2002.
- [33] R. H. Ferris, "Comparison of Measured and Calculated Normal-Mode Amplitude Functions for Acoustic Waves in Shallow Water ," *J. Acoust. Soc. Am.*, vol. 52, no. 3, pp. 981–988, February 1972.
- [34] F. Ingenito, "Measurements of mode attenuation coefficients in shallow water ," *J. Acoust. Soc. Am.*, vol. 53, no. 3, pp. 858–863, 1973.
- [35] R. P. P. Robert C. Spindel and J. A. Schwoerer, "Acoustic phase tracking of ocean moorings," *IEEE Journal of Oceanic Engineering*, vol. 3, no. 1, pp. 27–30, January 1978.
- [36] W. M. M. Robert C. Spindel, Robert P. Porter and J. L. Durham, "A high-resolution pulse-doppler underwater acoustic navigation system," *IEEE Journal of Oceanic Engineering*, vol. 1, no. 1, pp. 6–13, September 1976.
- [37] P. Oliveira, "Interpolation of Signals with Missing Data Using PCA," *2006 IEEE International Conference on Acoustics, Speech and Signal Processing, 2006. ICASSP 2006 Proceedings.*, vol. 3, pp. 828–831, 14-19 May 2006.
- [38] T. K. Chandrayadula and K. E. Wage, "Interpolation methods for vertical linear array element localization," in *Proceedings of the MTS/IEEE Oceans 2008 conference*, Quebec, Canada, September 2008.
- [39] T. Kailath, A. H. Sayed, and B. Hassibi, *Linear Estimation*. Prentice Hall, 2000.
- [40] M. R. Zarnetske, "Long-range ocean acoustic propagation experiment (loapex): Preliminary analysis of transmitter motion and tidal signals," Master's thesis, University of Washington, Seattle, October 2005.
- [41] Rex K. Andrew, Michael R. Zarnetske, Bruce M. Howe and James A. Mercer, "Ship-suspended acoustic transmitter position estimation and motion compensation," *IEEE Journal of Oceanic Engineering*, submitted.
- [42] L. L. Scharf and B. Friedlander, "Matched subspace detectors," *IEEE transactions on signal processing*, pp. 2146–2157, August 1994.
- [43] L. L. Scharf, *Statistical Signal Processing*. Addison-Wesley Publishing Company, 1991, vol. 1.
- [44] D. North, "An analysis of the factors which determine signal/noise discrimination in pulsed-carrier systems," *Proceedings of the IEEE*, vol. 51, no. 7, pp. 1016–1027, July 1963.

- [45] H. L. V. Trees, *Detection, Estimation and Modulation Theory*. John Wiley and Sons, 2001, vol. 3.
- [46] J. G. Proakis, *Digital Communications*. McGraw-Hill, 2000, ch. 13, pp. 639–640.
- [47] G. H. Golub and C. F. V. Loan, *Matrix Computations*. The Johns Hopkins University Press, 1996.
- [48] W. Munk and C. Wunsch, “Ocean acoustic tomography: a scheme for large scale monitoring,” *Deep-Sea Research*, vol. 26A, pp. 123–161, February 1979.
- [49] P. F. Worcester, “Reciprocal acoustic transmission in a mid-ocean environment,” *J. Acoust. Soc. Am.*, vol. 62, pp. 895–905, 1977.
- [50] T. M. Group, “The mid-ocean dynamics experiment,” *Deep-Sea Research*, vol. 25, pp. 859–910, 1978.
- [51] B. D. Cornuelle, “Inverse methods and results from the 1981 ocean acoustic tomography experiment,” Ph.D. dissertation, MIT, 1983.
- [52] J. Spiesberger, T. Birdsall, K. Metzger, R. Know, C. Spofford, and R. Spindel, “Measurements of gulf stream meandering and evidence of seasonal thermocline development using long-range acoustic transmissions,” *Journal of Physical Oceanography*, vol. 13, pp. 1836–1846, 1983.
- [53] J. J. Romm, “Applications of normal mode analysis to ocean acoustic tomography,” Ph.D. dissertation, MIT, 1987.
- [54] B. M. Howe, P. F. Worcester, and R. C. Spindel, “Ocean acoustic tomography: Mesoscale velocity,” *Journal of Geophysical Research*, vol. 92, no. C4, pp. 3785–3805, April 1987.
- [55] *SBE 37-SI Microcat*, Sea-Bird Electronics, Inc, 1808 136th Place NE, Bellevue, Washington 98005 USA.
- [56] *SBE 39 Temperature (pressure optional) Recorder*, Sea-Bird Electronics, 1808 136th Place NE, Bellevue, Washington 98005 USA.
- [57] S. M. Flatte, R. Dashen, W. H. Munk, K. M. Watson, and F. Zachariasen, *Sound Transmission Through a Fluctuating Ocean*. Cambridge University Press, 1979.
- [58] J. A. Colosi, A. B. Baggeroer, B. D. Cornuelle, M. A. Dzieciuch, W. H. Munk, P. F. Worcester, B. D. Dushaw, B. M. Howe, J. A. Mercer, R. C. Spindel, T. G. Birdsall, K. Metzger, and A. M. G. Forbes, “Analysis of multipath acoustic field variability and coherence in the finale of broadband basin-scale transmissions in the north pacific ocean,” *J. Acoust. Soc. Am.*, vol. 117, no. 3, March 2005.
- [59] C.T. Tindle and L.M.O’Driscoll and C.J. Higham , “Coupled mode perturbation theory of range dependence,” *J. Acoust. Soc. Am.*, vol. 1, no. 108, July 2000.

## Curriculum Vitae

Tarun Chandrayadula was born in Chennai (Madras), India in 1980. He received his Bachelor of Engineering from the University of Madras in 2001. He has been a graduate student at George Mason University (GMU), Virginia, USA since 2001 where he obtained his Master of Science in Electrical Engineering in 2003. He has since been working towards his Ph.D in the same area. He is a graduate research assistant in the ocean acoustics and signal processing lab at GMU. His interests include signal processing, physical layer communications and underwater acoustics. He is a member of the IEEE and the Acoustical Society of America (ASA).